Russian Original Vol. 58, No. 1, January, 1985

July, 1985

[redacted]

1 7 0 8

PEEL HERE

1

SATEAZ 58(1) 1-84 (1985)

SOVIET ATOMIC ENERGY

АТОМНАЯ ЭНЕРГИЯ
(ATOMNAYA ÉNERGIYA)

TRANSLATED FROM RUSSIAN

c/b CONSULTANTS BUREAU, NEW YORK

SOVIET ATOMIC ENERGY

Soviet Atomic Energy is abstracted or indexed in *Chemical Abstracts, Chemical Titles, Pollution Abstracts, Science Research Abstracts, Parts A and B, Safety Science Abstracts Journal, Current Contents, Energy Research Abstracts,* and *Engineering Index.*

Mailed in the USA by Publications Expediting, Inc., 200 Meacham Avenue, Elmont, NY 11003.

POSTMASTER: Send address changes to *Soviet Atomic Energy,* Plenum Publishing Corporation, 233 Spring Street, New York, NY 10013.

Soviet Atomic Energy is a translation of *Atomnaya Energiya,* a publication of the Academy of Sciences of the USSR.

An agreement with the Copyright Agency of the USSR (VAAP) makes available both advance copies of the Russian journal and original glossy photographs and artwork. This serves to decrease the necessary time lag between publication of the original and publication of the translation and helps to improve the quality of the latter. The translation began with the first issue of the Russian journal.

Consultants Bureau journals appear about six months after the publication of the original Russian issue. For bibliographic accuracy, the English issue published by Consultants Bureau carries the same number and date as the original Russian from which it was translated. For example, a Russian issue published in December will appear in a Consultants Bureau English translation about the following June, but the translation issue will carry the December date. When ordering any volume or particular issue of a Consultants Bureau journal, please specify the date and, where applicable, the volume and issue numbers of the original Russian. The material you will receive will be a translation of that Russian volume or issue.

Subscription (2 volumes per year)
Vols. 56 & 57: $560 (domestic), $621 (foreign)
Vols. 58 & 59: $645 (domestic), $715 (foreign)
Single Issue: $100
Single Article: $9.50

CONSULTANTS BUREAU, NEW YORK AND LONDON

c/b
233 Spring Street
New York, New York 10013

Published monthly. Second-class postage paid at Jamaica, New York 11431.

SOVIET ATOMIC ENERGY

A translation of *Atomnaya Énergiya*

July, 1985

Volume 58, Number 1 January, 1985

CONTENTS

	Engl.	Russ.
ARTICLES		
Region of Controlability of an Unstable Nuclear Reactor — N. S. Postnikov	1	3
Features of the Operation of Local Automatic Regulator Systems with Lateral Ionization Chambers for Weighted Summation of Signals from the Lateral Ionization Chambers — I. Ya. Emel'yanov, A. N. Aleksakov, E. V. Nikolaev, V. M. Panin, and L. N. Podlazov	7	11
Cesium Migration in Fuel Elements with Vibrocompacted Oxide Fuel with Getter Additives — V. A. Tsykanov, Yu. M. Golovchenko, I. G. Lebedev, A. V. Sukhikh, and A. A. Maershin	13	12
Allowing for the Effects of Residual Stresses on Creep in Channel Tubes — Yu. N. Knizhnikov, P. A. Platonov, and A. I. Ul'yanov	15	13
Effect of Diffusion on the Selective Sputtering of Composite Materials on a Carbon Base with Hydrogen Ions — M. I. Guseva, A. M. Izmailov, V. V. Kuchinskii, Yu. V. Nikol'skii, and V. A. Stepanchikov	20	18
An Apparatus for Measuring Bending-Stress Relaxation in Reactors — G. F. Lepin, N. P. Losev, A. Ya. Rogozyanov, and B. V. Samsonov	24	21
Structure of Molybdenum Bombarded with Low-Energy Hydrogen and Helium Ions during Creep Tests — V. N. Chernikov, I. B. Savvatimova, A. A. Babad-Zakhryapin, and A. P. Zakharov	28	24
Study of the Diffusion of Hydrogen in Materials by the Method of Elastic Scattering of Fast Neutrons — A. N. Valiev, V. N. Kadushkin, Z. P. Kiseleva, V. N. Serebryakov, B. G. Skorodumov, A. P. Sokolov, V. A. Shpiner, P. K. Khabibullaev, and I. O. Yatsevich	32	27
Possibilities of Reducing Radiation Erosion by the Use of Protective Coatings — B. A. Kalin, I. I. Chernov, D. M. Skorov, P. I. Kartsev, and E. P. Fomina	38	32
Optimizing Extractant Molecular Structure for Reprocessing Spent Nuclear Power Station Fuel — A. M. Rozen, A. S. Nikiforov, V. S. Shmidt, Z. I. Nikolotova, N. A. Kartasheva, and B. S. Zakharkin	45	38
Determination of the Efficiency of a Detector in Gamma Spectrometry of Large-Volume Samples — É. G. Tertyshnik and A. T. Korsakov	52	44
Isomeric Ratios of the Yields of Photonuclear Reactions for Gamma-Activation Analysis — M. G. Davydov, V. G. Magera, A. V. Trukhov, and É. M. Shomurodov	56	47

CONTENTS

(continued)

	Engl.	Russ.
Possibility of Decreasing the Energy Dependence of Detectors Based on the Thermal Luminophor LiF in the X-Ray Region — L. Z. Kalmykov, T. G. Kandel', S. M. Grinberg, and I. L. Kruglikov	60	50
LETTERS TO THE EDITOR		
Effect of Intragrain Pores on the Swelling of UO_2 — A. S. Gontar', R. Ya. Kucherov, and M. V. Nelidov	64	54
Study of the Conditions of Activation with a Radionuclide Neutron Source Based on ^{252}Cf — V. N. Kustov and V. V. Ivanenko	66	55
Determination of the Quantity of Tritium Formed in the Coolant of Water-Cooled–Water-Moderated Reactors — S. V. Popov, A. G. Babenko, B. N. Mekhedov, V. M. Ilyasov, I. G. Golubchikova, and L. E. Podporinova	69	57
New Formula for the Spectrum of Prompt Neutrons from Fission — A. F. Grashin and M. V. Lepeshkin	72	59
Spectrometry of the Multiplicity of Gamma Quanta on a Stationary Research Reactor — Yu. V. Adamchuk, A. L. Kovtun, G. V. Muradyan, Yu. G. Shchepkin, G. Georgiev, N. Kalinkova, E. Moravska, N. Stancheva, N. Chikov, and N. Yaneva	75	61
Neutron Sources Based on a Booster — N. I. Alekseev	79	64
Use of Metallic Lithium for Detecting Solar Neutrinos — E. P. Veretenkin, V. N. Gavrin, and E. A. Yanovich	82	65

The Russian press date (podpisano k pechati) of this issue was 12/28/1984. Publication therefore did not occur prior to this date, but must be assumed to have taken place reasonably soon thereafter.

REGION OF CONTROLABILITY OF AN UNSTABLE NUCLEAR REACTOR

N. S. Postnikov

UDC 621.039.515

Many modern reactors suffer from an unstable energy distribution throughout the core. We are only able to operate such reactors by using special systems of regulation, which must be capable of stabilizing the neutron flux [1, 2]. Many articles have discussed the stabilization of neutron flux ([1-5], for example). A feature of the regulation of unstable reactors is that the natural limitations on the effectiveness of the reactor control rods make it impossible to cope in the steady state with all disturbances of the steady-state conditions [6]. Consequently, the problem of finding the set of permissible initial disturbances of steady state conditions is urgent.

The present article proposes a way of plotting the region of controlability and studies in qualitative terms the set of deviations in the parameters of the reactor from their steady-state values which can be compensated by such a system of regulation.

Mathematical Model. A Statement of the Problem

We use equations for a single-group diffusion approximation to describe the changes in neutron flux, linearized in the region of the steady-state condition [7]:

$$\left.\begin{aligned} l\frac{\partial\varphi}{\partial t} &= M^2\nabla^2\varphi + (k_\infty^* - 1)\,\varphi + \\ &+ \frac{\Phi^*}{\bar{\Phi}}(\bar{\Phi}\mathbf{b}^{\mathrm{T}}\mathbf{u} + F) + \sum_{i=1}^{6}\lambda_i c_i - \beta\varphi \\ \frac{\partial c_i}{\partial t} &= \beta_i\varphi - \lambda_i c_i;\ i = 1\ \ldots.\ 6; \\ \varphi &+ d\,(\nabla\varphi,\ \mathbf{n}) = 0,\ \mathbf{r}\in\Gamma \end{aligned}\right\}, \tag{1}$$

where $\varphi = (\Phi - \Phi^*)/\bar{\Phi}$ is the relative deviation of neutron flux from its steady-state value Φ^*; $\bar{\Phi} = \left(\int_\Omega \Phi^* d\omega\right)\Big/\int_\Omega d\omega$ is the mean value of neutron flux in the core Ω, bounded by surface Γ; $\mathbf{r}$ is the radius vector; $\mathbf{r}\in\Omega+\Gamma$; c_i is the deviation from steady state of the concentration of nuclei radiators of delayed neutrons for the i-th group; l is the life of the instantaneous neutrons; λ_i is the decay constant of the source of delayed neutrons in the i-th group; β_i is the contribution of the i-th group to the neutron multiplication coefficient; $\beta = \sum_{i=1}^{6}\beta_i$; M^2 is the square of the migration distance of the neutrons; $\mathbf{n}$ is the normal to surface Γ; k_∞^* is the steady-state neutron multiplication coefficient for an infinite medium; α is a constant; t is time; F is the variation in the multiplication coefficient k_∞^* caused by the controls; the components of vector $\mathbf{b}(\mathbf{r})$ determine the reactivity coefficients; $\mathbf{b}^{\mathrm{T}}\mathbf{u}$ is the variation in reactivity due to internal feedback, which can be described by linear equations of the form

$$\frac{\partial\mathbf{u}}{\partial t} = P\mathbf{u} + \mathbf{a}\varphi, \tag{2}$$

where $P(\mathbf{r})$ is an $n\times n$ matrix; $\mathbf{a}(\mathbf{r})$ and $\mathbf{u}(\mathbf{r}, t)$ are vector functions.

Let us assume that the reactor is stabilized by an interconnected system of regulation whose contribution to the multiplication coefficient can be found from the expression

$$F = \sum_{i=1}^{k}\psi_i(\mathbf{r})\,\sigma_i. \tag{3}$$

Here $\bar{\psi}_i(\mathbf{r})$ is a weighting function; σ_i is the relative setting of the controls, which are

Translated from Atomnaya Énergiya, Vol. 58, No. 1, pp. 3-7, January, 1985. Original article submitted March 11, 1984.

0038-531X/85/5801-0001$09.50

gene material for neutron capture (liquids, gases). The following limitation is imposed on movements of the control rods:

$$|\sigma_i(t)| \leqslant \delta_i; \quad i = 1, \ldots k, \quad \delta_i > 0, \tag{4}$$

where points $\pm\delta_i$ represent the extreme positions of the controls.

If we postulate that

$$\left.\begin{aligned} W &= \begin{pmatrix} |M^2\nabla^2 + (k_\infty^* - 1) - \beta|/l; & \lambda_i/l; & \Phi^* \mathbf{b}^T/l \\ \beta_i; & -\lambda_i; & 0 \\ \mathbf{a}; & 0; & P \end{pmatrix}; \\ \mathbf{v} &= (\varphi,\ c_i,\ \mathbf{u}) \in E \\ \mathbf{h}_i &= \left(\frac{\Phi^*}{l\bar{\Phi}}\psi_i,\ 0,\ 0\right) \\ i &= 1, \ldots k \end{aligned}\right\}, \tag{5}$$

we can rewrite system (1)-(3) in the form

$$\dot{\mathbf{v}} = W\mathbf{v} + \sum_{i=1}^{k} \mathbf{h}_i \sigma_i; \quad |\sigma_i(t)| \leqslant \delta_i. \tag{6}$$

Let us assume that the reactor is unstable without a system of regulation, i.e., that part of the intrinsic value of operator W (the last term) lies to the right of the imaginary axis of the complex plane. The problem consists in determining the region of controllability Q of system (6), i.e., the set of initial conditions $\mathbf{v}(0)$ for which a permissible (4) exists that translates system (6) from $\mathbf{v}(0)$ to the point $\mathbf{v} = 0$. Let us assume that the translation of system (6) from $\mathbf{v}(0)$ to point 0 is permitted both at the end and also up to infinity in time, i.e., we shall endeavor to find a region of ε controllability [8].

Method of Investigation

Space E of system (6) can be represented in the form of the sum of two half-spaces $E = R^n + E_0$, where R^n and E_0 are the unstable and stable invariant forms of operator W. We can assume that the unstable half-space is finite. System (6) is usually divided into two subsystems [9]:

$$\dot{\mathbf{y}} = W^+\mathbf{y} + \sum_{i=1}^{k} \mathbf{h}_i^+ \sigma_i; \quad \mathbf{y} \in R^n; \quad |\sigma_i(t)| \leqslant \delta_i; \tag{7}$$

$$\dot{\mathbf{z}} = W^-\mathbf{z} + \sum_{i=1}^{k} \mathbf{h}_i^- \sigma_i; \quad \mathbf{z} \in E_0; \quad |\sigma_i(t)| \leqslant \delta_i. \tag{8}$$

Subsystems (7), (8) describe the behavior of the initial system (6) and its unstable and stable forms R^n and E_0. In this case, W^+ and W^- are the constrictions of operator W in half-spaces R^n and E_0; $\mathbf{h}_i^+$ and $\mathbf{h}_i^-$ are the projections of vector $\mathbf{h}_i$ on R^n and E_0. The region of ε controllability Q of system (6) takes the form [8, 10]:

$$Q = Q^+ + E_0 = \{\mathbf{v} = \mathbf{y} + \mathbf{z} : \mathbf{y} \in Q^+; \quad \mathbf{z} \in E_0\},$$

i.e., the set of those values of $\mathbf{v}$ whose projection on the stable manifold is artibrary, whereas their projection onto unstable half-spaces R^n belongs to a limited convex set Q^+, fully determined by its hyperplane of reference [10]:

$$Q^+ = \{\mathbf{y} : |\boldsymbol{\eta}^T\mathbf{y}| < d(\boldsymbol{\eta}) \quad \text{for all} \quad \boldsymbol{\eta} \in R^n\}. \tag{9}$$

For each factor $\boldsymbol{\eta}_0 \in R^n$, a set Q^+ lies in the band $-d(\eta_0) < \boldsymbol{\eta}_0^T\mathbf{y} < d(\eta_0)$ and holds true for hyperspaces of reference $\boldsymbol{\eta}_0^T\mathbf{y} = \pm d(\eta_0)$. No points of set Q^+ lie in the half-space $\boldsymbol{\eta}_0^T\mathbf{y} > d(\eta_0)$ and $\boldsymbol{\eta}_0^T\mathbf{y} < -d(\eta_0)$. The formula for finding $d(\eta)$ takes the form [10]

$$d(\boldsymbol{\eta}) = \sum_{i=1}^{k} \delta_i \int_0^\infty |\boldsymbol{\eta}^T \exp(-W^+\tau)\,\mathbf{h}_i^+|\,d\tau. \tag{10}$$

Consequently, the problem of finding the region of controllability reduces to that of deriving finite subsystem (7) and constructing set Q^+. System (7) can easily be described in explicit form, provided we know the characteristic values of s_i of operator W lying in right-hand half-space (Re $s_i > 0$) and the characteristic functions $\mathbf{v}_i$ of operator W* conjugate to W. System (7) is obtained after introducing functionals y_i:

$$y_i(t) = \langle \mathbf{v}_i, \mathbf{v}(t) \rangle = \int_\Omega \varphi_i(\mathbf{r})\,\varphi(\mathbf{r}, t)\,d\omega + \sum_{i=1} \int_\Omega c_i(\mathbf{r})\,c_i(\mathbf{r}, t)\,d\omega + \int_\Omega \mathbf{u}^{\mathrm{T}}(\mathbf{r})\,\mathbf{u}(\mathbf{r}, t)\,d\omega$$

followed by differentiation of y_i with respect to t, in accordance with expression (6).

Set Q^+ can be built up with the aid of formulas (9) and (10). However, there is another way of finding region Q^+ which does not involve calculating $d(\eta)$ by means of formula (10), based on the fact that the boundary of Q^+ comprises the trajectory of subsystem (7) when $\sigma_i = \pm\delta_i$. This method is particularly suitble for situations in which the dimensionality of the unstable manifolds R^n is low (n = 1, 2, 3). Formulas for the trajectory bounding Q^+ in the simplest cases can be found in [10, 11].

We should, however, bear in mind that calculations do not in practice always need an accurate construction of the controllability region, an estimate being all that is needed in such cases. To assess the upper limit, we only have to calculate $d(\eta)$ for the one vector η_0. The region of controllability will not apply to the initial state of system (6), $\mathbf{v}(0)$, whose projection onto the unstable manifold R^n lies in the space $\eta_0^{\mathrm{T}}\mathbf{y} > d(\eta_0)$. If these initial conditions include a disturbance of the steady-state conditions which always tends to arise during operation of the reactor, then by calculating only the one value of $d(\eta_0)$, we can find out that the system of regulation is useless for that particular role, without resorting to the law governing the displacement of the control rods.

One assessment of the upper end of the range is obtained by finding $-W^{-1}\left(\sum_{i=1}^{k} \mathbf{h}_i\sigma_i\right)$ for σ_i = const, $|\sigma_i| \leqslant \delta_i$. The region of controllability relates to all the steady-state conditions of system (6) corresponding to a particular position of the control rod.

Examples

Let us consider a one-dimensional model of a reactor with delayed positive feedback

$$\left.\begin{aligned} &\frac{M^2}{H^2}\,\frac{\partial^2\varphi}{\partial\xi^2} - a\varphi + bu + F = 0 \\ &T\,\frac{\partial u}{\partial t} = -u + \varphi;\ \varphi(0) = \varphi(1) = 0 \end{aligned}\right\}, \tag{11}$$

where H is a linear dimension of the reactor (its height or the core diameter); ξ is the coordinate of the reactor; T is the time constant of the feedback; b, a are constants > 0 and represent the coefficients of reactivity.

Operator (5) of system (11) has intrinsic values and intrinsic function of the form

$$\left.\begin{aligned} &s_i = \left(\frac{b}{(\pi i)^2\,\frac{M^2}{H^2} + a} - 1\right)/T; \\ &u_i(\xi) = \sin \pi i\xi; \\ &\varphi_i(\xi) = u_i(Ts_i + 1); \end{aligned}\right\} \quad i = 1, 2 \ldots \tag{12}$$

The reactor is unstable over n harmonics when b > a + $[(\pi nM)^2/H^2]$. If

$$M^2/H^2 = 0.325 \cdot 10^{-3};\quad a = \beta = 0.0075, \tag{13}$$

then the instabilities for the fundamental, second, and third harmonics occur when b = 1.43β, b = 2.71β, and b = 4.85β, respectively.

By stipulating that $y_i = \int_0^1 u(\xi, t)\sin \pi i\xi\,d\xi$ and differentiating y_i with respect to t, expression (11) gives us subsystem (7) in the form

$$\dot{y}_i = s_i y_i + \frac{(Ts_i + 1)}{bT} \int_0^1 F \sin \pi i\xi\,d\xi;\quad i = 1, \ldots n. \tag{14}$$

The region of controllability of system (11) has the form

$$Q = \{u(\xi) : (y_1 \ldots y_n\} \in Q^+ \in R^n\}. \tag{15}$$

Let

$$u(\xi,\ t) = \sum_{i=1}^{\infty} x_i(t) \sin \pi i \xi. \tag{16}$$

Then $y_i = \frac{1}{2}x_i$, and the controllability region of system (11) takes the form of a set of functions $u(\xi)$, in the expansion of which according to intrinsic function (12) the coefficients for the stable harmonics are arbitrary, while the peak-to-peak values of the unstable harmonics correspond to set Q^+, which we are able to find.

Let us assume that F in Eq. (11) has the form

$$F = F_1 = \sum_{i=1}^{k} \delta(\xi - \xi_i^*)\sigma_i; \quad |\sigma_i(t)| \leqslant \delta_i, \tag{17}$$

i.e., there are k control rods introducing reactivity at points ξ_i^*. By selecting in R^n the vector $\eta_i = (0, \ldots 1, \ldots 0)$ and calculating $d(\eta_i)$ by means of formula (10) for system (14), we find that the controllability region of system (11) does not fall into the set of those functions $u(\xi)$ for which

$$|y_i| = \left| \int_0^1 u(\xi) \sin \pi i \xi \, d\xi \right| > \Delta_i = \frac{\sum_{j=1}^{k} \delta_j |\sin \pi i \xi_j^*|}{s_i T \left[(\pi i)^2 \frac{M^2}{H^2} + a \right]}. \tag{18}$$

The value of Δ characterizes the contribution made by the control system to the i-th unstable harmonic. We can see from (18) that the size of the controllability region greatly depends upon the parameters of the reactor and the system of regulation. If the effectiveness of the rods (δ_i) is increased, the region of controllability will itself increase. By choosing an adequate degree of effectiveness, we are able to include any predetermined set of deviations of the reactor parameters in the region of controllability. However, the effectiveness of the rods is not infinite, so we have to look to other resources for increasing the permissible disturbances of the steady-state conditions. We can see from expression (18) that $\Delta_i = 0$ and the reactor is not able to stabilize in the i-th harmonic if all the rods are in the positions belonging to this harmonic ($\sin \pi i \xi_j^* = 0$). We can increase the region of controllability without changing the effectiveness of the rods by planting the rods at points corresponding to the maximum for the harmonic ($\sin \pi i \xi_j^* = 1$). We can see from expression (18) that Δ_i is inversely proportional to the positive intrinsic value of s_i. Therefore, the size of the region of controllability falls to zero (or increases) with an increase (or decrease) in the degree of reactor instability.

If it is only the fundamental harmonic that is unstable, then Δ_1 (18) entirely determines the region of instability, which is subject only to the $u(\xi)$ for which $|2x_1| = |y_1| < \Delta_1$. If all the harmonics are unstable, then set Q^+ in the plane y_1, y_2 is determined by taking into account the interactions between the fundamental and second harmonic. The set Q^+ in Fig. 1 is drawn for parameters (13) and $b = 3.5\beta$. Curve 1 bounds Q^+ when only one control rod is in use at the point $\xi_1^* = 1/4$, with an effectiveness $\delta_1 = \beta/2$. We can see that a reactor that is unstable in two harmonics can be stabilized by means of a singly linked system of regulation. Curve 2 bounds Q^+ in the presence of two control rods at points $\xi_1^* = 1/4$ and $\xi_2^* = 3/4$, with an effectiveness of $\delta_1 = \beta/4$, $\delta_2 = \beta/4$. We can see from Fig. 1 that the controllability region for one rod is little different from that for two rods with the same summated effectiveness.

Let us assume that the reactor has a closed system of control in addition to its open system of regulations (17), which at any given moment in time maintains the given value constant. The contribution of these systems to the multiplication coefficient of the neutrons can be found from the expression $F = F_1 + F_2$, where F_1 has the form (17) and F_2 is found from the following expression:

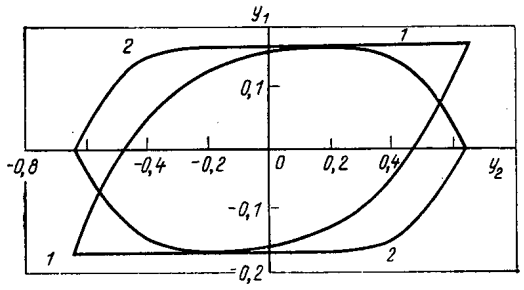

Fig. 1. Regions of controllability of systems (11), (17).

$$r = r_1 + r_2;\ r_2 = \sum_{i=1} g_i(\xi)\,\gamma_i; \qquad (19)$$

$$\gamma_i : \int_0^1 f_i(\xi)\,\varphi(\xi,\ t)\,d\xi = 0.$$

In this expression, γ_i signifies the relative position of the control rod in the reactor, as did σ_i; $g_i(\xi)$, $f_i(\xi)$ are weighting functions. Equation (19) defines the law governing the displacement of the rods. The operator, or an automatic system, moves the rods to a position γ_i such that Eq. (19) is satisfied at any instant in time. The system of regulation (19), by maintaining m given values constant, is able to stabilize the reactor. However, as with the initial system, unstabilized high harmonics can remain in the reactor. We also introduce an open system of regulation (17) to stabilize these.

To build up the region of controllability of system (17) in the presence of system (19), we need to know the positive intrinsic values of s_i and the intrinsic functions u_i, $\bar{u}_i$ of operators W and W*, which are determined taking closed system (19) into consideration. Functions u_i, $\bar{u}_i$ are solutions of the boundary problems

$$\left.\begin{aligned} &\frac{M^2}{H^2}\,\frac{d^2\varphi_i}{d\xi^2} + \left(\frac{b}{Ts_i+1} - a\right)\varphi_i + \\ &+ \sum_{j=1}^{m} g_j(\xi)\,\gamma_j^i = 0;\ u_i = \frac{\varphi_i}{Ts_i+1} \\ &\gamma_j^i : \int_0^1 f_j(\xi)\,\varphi_i(\xi)\,d\xi = 0; \\ &\varphi_i(0) = \varphi_i(1) = 0; \quad \begin{matrix} i = 1,\ \ldots\ n \\ j = 1,\ \ldots\ m \end{matrix} \end{aligned}\right\}; \qquad (20)$$

$$\left.\begin{aligned} &\frac{M^2}{H^2}\,\frac{d^2\bar{\varphi}_i}{d\xi^2} + \left(\frac{b}{Ts_i+1} - a\right)\bar{\varphi}_i + \\ &+ \sum_{j=1}^{m} f_j(\xi)\,\bar{\gamma}_j^i = 0;\ \bar{u}_i = \frac{\bar{\varphi}_i}{Ts_i+1} \\ &\bar{\gamma}_j^i : \int_0^1 g_i(\xi)\,\bar{\varphi}_i(\xi)\,d\xi = 0; \\ &\bar{\varphi}_i(0) = \bar{\varphi}_i(1) = 0; \quad \begin{matrix} i = 1,\ \ldots\ n \\ j = 1,\ \ldots\ m \end{matrix} \end{aligned}\right\}. \qquad (21)$$

By postulating that $y_i = \int_0^1 \bar{u}_i(\xi)\,u(\xi,\ t)\,d\xi$ and differentiating y_i, we obtain subsystem (7) in accordance with expressions (11), (17), and (19) in the form

$$\dot{y}_i = s_i y_i + \frac{Ts_i+1}{bT} \sum_{j=1}^{k} \bar{u}_i(\xi_j^*)\,\sigma_j, \quad i = 1,\ \ldots\ n.$$

The region of controllability now has a new form: (15).

Let us assume that system (19) consists of one rod (m = 1), located at point 3/4 [$g_1 = \delta(\xi - 3/4)$] and maintaining the power [$f_1(\xi) = \sin \pi\xi$] constant. The solution to systems (20), (21) takes the form

$$s_i = \left(\frac{b}{(\pi i)^2\,\frac{M^2}{H^2} + a} - 1\right)/T;$$

$$\bar{u}_i = \left(\sin \pi i\xi - \frac{\sin \frac{3}{4}\pi i}{\sin \frac{3}{4}\pi} \sin \pi\xi\right), \quad i = 2,\ 3\ \ldots.$$

$$u_i = \sin \pi i\xi;$$

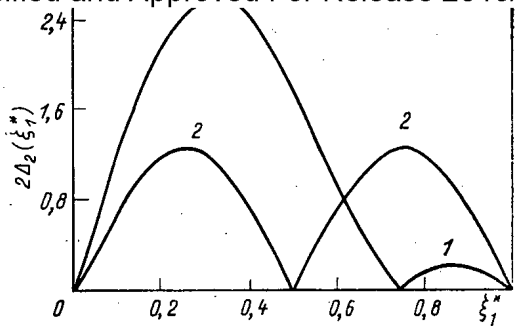

Fig. 2. Relationship of size of region of controllability to arrangement of control rods.

$$\bar{\gamma}_1^i = \frac{\sin\frac{3}{4}\pi i}{\sin\frac{3}{4}\pi}\left[b - \left(\frac{\pi^2 M^2}{H^2} + a\right)(Ts_i + 1)\right];\ \gamma_1^i = 0.$$

Let us also assume that b = 3.5β, while the remaining parameters correspond to expression (13). As a consequence, a reactor equipped with a mean-power regulator will only remain unstable in the second harmonic $u_2 = \sin 2\pi\xi$. A second regulator (17) (k = 1, $\delta_1 = \beta/2$) is introduced, bringing in reactivity at point ξ_1^*, which has to be included among the parameters.

A region of controllability is assinged in half-space $\int_0^1 u(\xi)\sin\pi\xi d\xi = 0$ and comprises only those values of u(ξ) for which

$$\left|\int_0^1 \bar{u}_2(\xi)\,u(\xi)\,d\xi\right| < \Delta_2(\xi_1^*) = 0.63\left|\sin 2\pi\xi_1^* + 1.41\sin\pi\xi_1^*\right|.$$

By employing an expression of u(ξ) in functions of sin πiξ, we obtain a region of controllability in the form

$$Q = \{u(\xi) : x_1 = 0;\quad |x_2| < 2\Delta_2(\xi_1^*);$$
$$|x_i| < \infty,\quad i = 3,4\ldots\}.$$

If we consider a deviation of u(ξ) in the form of a second harmonic $u(\xi) = x_2\sin 2\pi\xi$, then the rod at point ξ_1^* can compensate for a deviation of amplitude $|x_2| < 2\Delta_2(\xi_1^*)$. The relationship between the size of the region of controllability at the second harmonic and the position of the second control rod is shown in Fig. 2 (curve 1). This same relationship $2\Delta_2(\xi_1^*)$ of form (18) is determined in curve 2 for the case where there is no mean-power regulator. By comparing these curves, we can see that the interaction of the regulators has a powerful influence on the size of the region of controllability. In fact, Fig. 2 shows that if the rod belonging to the open system of regulation is located in the interval $\xi_1^* \in [0;\ 0.62]$, then its interaction with the mean-power regulator facilitates third-harmonic stabilization, to increase the region of controllability. When the rod is at point 3/4, the region of controllability does not reach zero, even if the second rod is located at the harmonic "node": point $\xi_1^* = 1/2$. If regulator (17) lies in the interval $\xi_1^* \in [0.62;\ 1]$, however, the interaction of the regulators obstructs third-harmonic stabilization, reducing the size of the region of controllability to zero when both regulators are at the same point $\xi_1^* = 3/4$.

LITERATURE CITED

1. I. Ya. Emel'yanov, E. V. Filipchuk, P. T. Potapenko, and V. T. Neboyan, "Engineering problems concerned with the regulation of an unstable distribution of power in a nuclear reactor," At. Energ., 37, No. 2, 118-122 (1974).
2. I. Ya. Emel'yanov, P. A. Gavrilov, and B. N. Seliverstov, The Control and Safety of Nuclear Power Reactors [in Russian], Atomizdat, Moscow (1975).
3. I. Ya. Emel'yanov et al., "The development and testing of systems of local regulation of reactor type RBMK-1000," Vopr. At. Nauki Tekh., Ser. Fiz. Tekh. Yad. Reaktorov, No. 1(5), 3-16 (1979).
4. E. V. Filipchuk, P. T. Potapenko, and V. V. Postnikov, Controlling the Neutron Field of a Nuclear Reactor [in Russian], Energoizdat, Moscow (1981).
5. V. N. Konev and B. Z. Torlin, "The validity of the problem of neutron distribution in a reactor," At. Energ., 54, No. 6, 390-395 (1983).
6. N. S. Postnikov and E. F. Sabaev, "The stability of reactors with regulating systems having positive coefficients of reactivity," Vop. At. Nauki Tekh., Ser. Dinamika Yad. Energ. Ustanovok, No. 2(8), 79-89 (1975).

(1965).
8. A. G. Butkovskii, Theory of Optimum Control of Systems with Distributed Parameters [in Russian], Nauka, Moscow (1965).
9. S. G. Krein, Linear Differential Equations in Banach Space [in Russian], Nauka, Moscow (1967).
10. A. M. Formal'skii, Controllability and Stability of Systems with Limited Margins [in Russian], Nauka, Moscow (1974).
11. V. G. Boltyanskii, Mathematical Methods of Optimum Control [in Russian], Nauka, Moscow (1969).

FEATURES OF THE OPERATION OF LOCAL AUTOMATIC REGULATOR SYSTEMS WITH LATERAL IONIZATION CHAMBERS FOR WEIGHTED SUMMATION OF SIGNALS FROM THE LATERAL IONIZATION CHAMBERS

I. Ya. Emel'yanov, A. N. Aleksakov, E. V. Nikolaev, V. M. Panin, and L. N. Podlazov

UDC 621.039.56

At the present time, high-powered water-cooled channel(RBMK) reactors with traditional neutron-power automatic regulators, using lateral ionization chambers (LIC), for the most part employ local automatic regulators (LAR–LIC), which were themselves developed from LIC. Since LAR–LIC have a number of important advantages over a straight automatic regulator (AR) [1], a trend towards replacing these by LAR–LIC has arisen. The AR rods in the RBMK reactor are already set at distances that are close to the optimum spacing for LAR–LIC [1, 2]. Consequently, the conversion from AR to LAR–LIC can be considered as equivalent to replacing the synchronous control of all control rods according to the average unbalance over all the measured channels by control of each rod separately according to the unbalance between the signal of the LIC and the setting for each measurement channel.

This can be written formally as

$$q_i(t) = \sum_{j=1}^{n} a_{ij} \Delta J_j(t), \tag{1}$$

where qi(t) is the unbalance of the i-th control channel, a_{ij} is the weighting coefficient at which the j-th LIC is taken into account in the i-th channel; $\Delta J_j(t)$ is the deviation of the signal of the j-th LIC from setting; n is the number of control channels.

For an AR system, all values of $a_{ij} = 1$; for the LAR–LIC system, $a_{ij} = \delta_{ij}$, where

$$\delta_{ij} = \begin{cases} 0, & i \neq j \\ 1, & i = j. \end{cases}$$

We can see from Eq. (1) that AR and LAR–LIC are the extreme limiting cases of averaging unbalances for forming the rod-control signal. Intermediate cases would seem to be possible in which the i-th rod of the LAR–LIC system takes account of other (j-th) chambers, subject to some weighting factor a_{ij}, in addition to the signal from the i-th channel.

The introduction of weighted summation opens up wide possibilities for varying the properties of an LAR–LIC system, by choosing one or other method of weighting. Investigations of these new possibilities are of undoubted interest, both scientific and practical. A major role here appears to be played by the weighting coefficient itself. If we assume that the processes in reactors characterizing the interactions of the separate points are of a relaxation type, then the natural choice of weighting factors will be subject to an exponential relationship, i.e., they will take the form

$$a_{ij} = \frac{\exp(-\eta \mid \theta_i - \theta_j \mid)}{\sum_{k=1}^{n} \exp(-\eta \mid \theta_i - \theta_k \mid)}, \tag{2}$$

Translated from Atomnaya Énergiya, Vol. 58, No. 1, pp. 7-11, January, 1985. Original article submitted June 15, 1984.

0038-531X/85/5801-0007$09.50

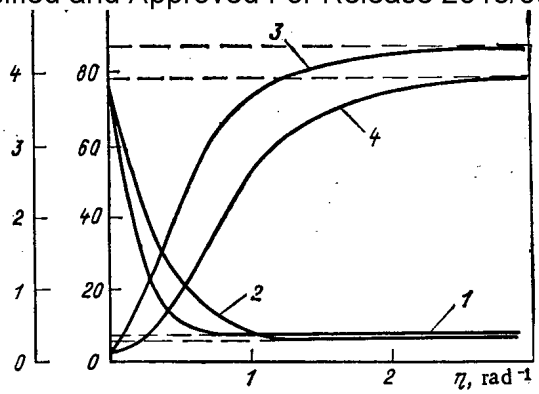

Fig. 1. Relationships of dispersion D (1, 2) and rod displacement R (3, 4), that arise when processing a polyharmonic disturbance, to coefficient η.

where θ_i and θ_j are the azimuth i-th and j-th LICs, respectively.

The LAR–LIC system in use at the present time incorporates eight measurement channels, in which signals representing the deviation of the LIC indications from the settings are formed, together with eight rods that can be moved individually in accordance with each signal. The rods are controlled according to a relay law, i.e., the excursion of the unbalance outside the limits of the set dead zone moves the rods at constant speeds in a direction designed to eliminate the deviation. When weighted summation is introduced into the commands governing movement of the rods, then not only does the unbalance in the measurement channel of the LIC appropriate to the rod concerned contribute to the signal, but also the unbalances in the other measurement channels.

When studying the properties of LAR–LIC systems with weighting coefficients (2), we use a polyharmonic radial–azimuthal dynamic model of the RBMK [3]. This model makes use of the equation for the dynamics of the neutron field, linearized about the rated condition of operation, and includes a description of the action of the LAR–LIC system itself. The solution appears in the form of a finite series of low harmonics (16 terms in the expansion).

The quality of a "fast" reaction of the system is estimated by processing momentary disturbances of the neutron-multiplication coefficient of equal amplitude to each other for the whole set of harmonics participating in the solution. The criterion of quality is the residual deformation of the neutron field after processing the disturbance and the summated displacement of the rods during this processing. The measure of the residual field deformation is the dispersion

$$D(t_k) = \int_S \varphi^2(\mathbf{r}, t_k)\, d\mathbf{r},$$

where $\varphi(\mathbf{r}, t_k)$ is the dimensionless deviation of the neutron flux from its steady-state value at instant t_k at the end of the disturbance-processing operation and the transition of the relay-action LAR–LIC into the sliding state. The displacement of the rods is measured by the sum of the squares of the linear displacements at that particular moment:

$$R(t_k) = \sum_{i=1}^{8} \Delta l_i^2(t_k).$$

In addition to this high-reactivity criterion, an important characteristic of the system is its stabilizing properties when there is a nonuniform distribution of energy. The relationship of dispersion D and the displacement of the rod system R to coefficient η is shown in Fig. 1. When η = 0, the signals of all the chambers are summated for each channel of LAR–LIC regulation and the system turns into an eight-rod AR. When $\eta \to \infty$, the system turns into an LAR–LIC system in which each rod operates in accordance with the signal from its individual chamber.

Up to a point, the dispersion will rise above the asymptote corresponding to $\eta = \infty$ when the slope of the decay of the weighting coefficients falls. However, a marked reduction in the rod displacement R begins even earlier. This shows that when weighted summation is introduced, the quality of the processing achieves a level equal to that of an LAR–LIC system at far smaller rod displacements. The nature of this effect is determined by the width of the dead zone δ of the LAR–LIC relay system. The results set out in Fig. 1 were obtained for δ = 1.0 (2, 4) and 0.5 (1, 3). It is clear that deviations in D and R from the asymptotes corresponding to $\eta \to \infty$ start at lower values of η for δ = 0.5% than is the case for δ = 1.0%.

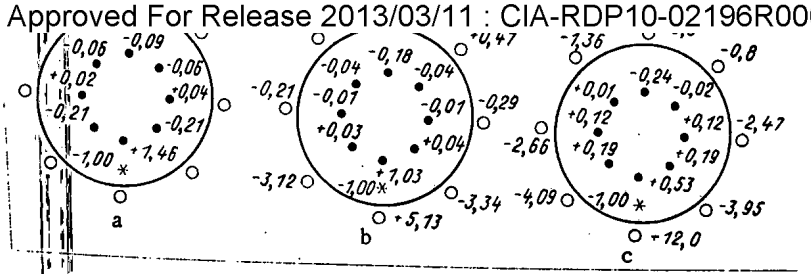

Fig. 2. Reaction of the system to disturbances by the rod closest to the chamber at $\eta \to \infty$ (a), η = 1.0 (b), and η = 0.5 (c): ●) LAR–LIC rod (the displacement in m being marked against the rod concerned); o) LIC (the unbalance in % being marked against the chamber concerned); *) the point of disturbance.

The D and R curves for different values of δ approach different asymptotes at $\eta \to \infty$. A reduction in δ leads to a rise in the asymptote of D at relatively low values of δ ($\delta \leqslant 1.5\%$), since the greater the accuracy in processing the disturbance, the larger will be rod displacement that is entailed. An insignificant increase in the accuracy with which the low harmonics are regulated means that a reduction in δ is swamped by an excess of high-harmonic excitation, leading to an excessive reaction of the rods: the R asymptote lies higher at $\eta \to \infty$ for smaller values of δ. An excessive extension of the dead zone results in loss of accuracy in regulating the lower harmonics, and the D asymptote starts to grow at some value of δ (3-4%).

Figure 2 gives the results of calculations at δ = 1.0%, illustrating the changes in the nature of the system reaction due to disturbances close to the chamber, when weighted summation at various values of η is introduced. In the calculations, the disturbance is created by manually withdrawing the control rod adjacent to the chamber at radius of 5.3 m. The rod is extracted by 1 m.

When $\eta \to \infty$, the motion of the rod operating in the channel in which the disturbance arose is 1.46 m. The rods in the neighboring channels travel in the opposite direction by 0.21 m. The rod movement in the remaining channels is insignificant (0.02-0.06 m). A relatively large movement (0.09 m) is observed in the rod diametrically opposite to the point of disturbance.

When η = 1.0, the motion of the rod in the channel subject to the disturbance is 1.03 m under the same conditions as before. The rods in the neighboring channels move by 0.04 m in the same direction. The remaining LAR–LIC rods move in a direction coinciding with the disturbance by 0.01-0.04 m, while the diametrically opposed rod moves by 0.18 m.

When η = 0.5, the surplus attenuation of the high azimuthal harmonics introduced by weighted summation leads to a "blurring" of the reaction to the disturbance. The processing of the disturbance involves all the rods in the half of the reactor lying adjacent to the "disturbed" LAR–LIC channel. The rod of the disturbed channel is moved by 0.53 m (disturbance = 1 m), while the diametrically opposite rod moves by 0.24 m. Consequently, the case where η = 1.0 for δ = 1.0% roughly corresponds to the state in which the reaction to a disturbance near to a chamber is concentrated mainly in the disturbed channel itself.

We will now turn our attention to the behavior of the unbalance signals in the measurement channels of the LAR–LIC. When $\eta \to \infty$, the signals remain within the dead zone. The introduction of weighted summation means that the unbalances after processing differ significantly from zero. The greatest deviation is seen in the disturbed channel. As η decreases, the distortion in the form of the neutron field caused by the disturbance becomes worse. When η = 1.0, the "residual" deviation in the disturbed channel is $\sim$8.4% relative to the mean deviation in the two neighboring channels. This is increased to 16% when η = 0.5.

The introduction of weighted summation leads to some freedom in variation of the unbalance signal compared with the existing LAR–LIC system. This feature can be put to use when there is a possibility of drift in the sensitivity of the measurement channels. The drift can lead to a mistaken increase in power in the region of the rod of the drifting channel if the sensitivity falls, and it is impossible to detect such a situation from the chamber signals in the existing LAR–LIC system.

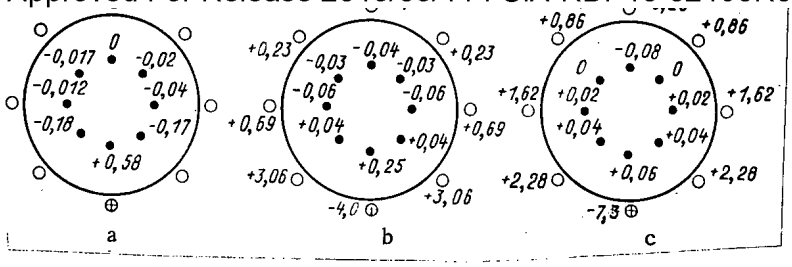

Fig. 3. Reaction of the system to a disturbance in the setting of one of the LAR–LIC channels: ⊕) disturbed regulating channel; the remaining symbols have the same meaning as in Fig. 2.

The reaction of the system to a fall in sensitivity in one of the channels (a sudden 10% fall) is shown in Fig. 3. This can be treated as being due to a change in the individual setting of the LAR–LIC. We can see from the results that in the case of a disturbance of a rod near to the chamber, the introduction of weighted summation with $\eta = 1.0$ and $\delta = 1.0\%$ confines the reaction of the system mainly to the disturbed channel. In this case, the presence of drift can be reliably established from the difference in the signals of the drifting chamber and the two neighboring chambers.

In addition to the required quality of reaction to disturbances, the LAR–LIC system has to ensure stabilization of an unstabilized energy distribution. The criterion of effectiveness of the system in this regard is the time constant of the development of neutron-field distortion due to instabilities in the field when the reactor is operating at a steady-state level, while the system functions in the stabilization mode [1]. The time constant is expressed by the roots of the characteristic equation of the system of equations for dynamics of a reactor equipped with control rods having a most-effective part. Let us consider the effect of weighted summation on this criterion.

Let us write expression (1) in matrix form:

$$Q = A\Phi,$$

where Q is the matrix columns of the "operational" unbalances, A is the weighting factor matrix, and Φ is the matrix columns of the deviation of the LIC from setting. This expression also relates to the case without weighted summation, A in this case being a unit matrix. Since the introduction of weighted summation changes only matrix A, the changes in the stabilizing properties of the system can be analyzed from the variation in the properties of this matrix.

If the dead zone $\delta = 0$, then $A\Phi = 0$ with the system operating in the stabilization mode. Since A is a unit matrix without weighting summation, then $\Phi = 0$. If the determinant of the matrix does not fall to zero when weighted summation is introduced, $A\Phi = 0$ only when $\Phi = 0$. This signifies that when $\delta = 0$ and $\det(A) \neq 0$, the introduction of weighted summation does not affect the stabilizing properties of the system.

Let us consider the properties of matrix A when weighted summation is used. Let us assume that the weighting coefficients summated in the LIC signal when the unbalance is formed vary symmetrically to the same extent for all channels with distance in azimuth from the basic chamber. In this case, matrix A is cyclic and symmetrical. As a result, we find that

$$\det(A) = (a_0 + 2a_1 + 2a_2 + 2a_3 + a_4)\ (a_0 + \sqrt{2}a_1 - \sqrt{2}a_3 - a_4)^2 (a_0 - 2a_2 + a_4)^2 \times$$

$$\times (a_0 - \sqrt{2}a_1 + \sqrt{2}a_3 - a_4)^2 (a_0 - 2a_1 + 2a_2 - 2a_3 + a_4)$$

for an eight-zone LAC–LIC system, where a_0 is the weighting coefficient of the basic chamber; a_1, a_2, a_3, and a_4 are the weighting coefficients of chambers displaced by 45°, 90°, 135°, and 180° respectively, relative to the basic LIC. The weighting coefficients are standardized so that $a_0 + 2a_1 + 2a_2 + 2a_3 + a_4 = 1$. The determinant of matrix A equals zero if one of the following conditions is satisfied:

$$a_0 + \sqrt{2}a_1 - \sqrt{2}a_3 - a_4 = 0; \quad (3)$$

$$a_0 - 2a_2 + a_4 = 0; \quad (4)$$

$$a - \sqrt{2}a_1 + \sqrt{2}a_3 - a_4 = 0; \quad (5)$$

$$a_0 - 2a_1 + 2a_2 - 2a_3 + a_4 = 0. \quad (6)$$

which permute the monitored system of rods for a given set of weighting coefficients. The inability to monitor any azimuthal harmonic shows that the unbalances in all regulation channels are zero, regardless of the amplitude of the harmonic. For example, condition (3) is equivalent to a first azimuthal harmonic that is unmonitorable. To show this, we find the unbalances of the LAR—LIC system due to deformation of the radial—azimuthal neutron field of the first azimuthal harmonic type, aligned in such a way that the zero line passes through the horizontal diameter of the reactor. The deviation in the lower half is positive, while that in the upper half is negative. The transducers are numbered clockwise, starting with the transducer on the lower end of the vertical diameter. The unbalance in the i-th regulation channel, expressed through amplitude $[A_{01}(t)]$ and the spatial form $[\psi_{01}(r)\cos\theta]$ of the first azimuthal harmonic, equals

$$q_i(t)=\sum_{j=1}^{8} a_{ij}A_{01}(t)\,\psi_{01}(r_j)\cos\theta_j=C\sum_{j=1}^{8} a_{ij}\cos\theta_j,$$

where $C = A_{01}(t)\psi_{01}(r_j)$.

Taking condition (3) into consideration, we find that

$$q_1=C\left(a_0+\frac{\sqrt{2}}{2}a_1+0a_2-\frac{\sqrt{2}}{2}a_3-a_4-\frac{\sqrt{2}}{2}a_3+0a_2+\frac{\sqrt{2}}{2}a_1\right)=C\left(a_0+\sqrt{2}a_1-\sqrt{2}a_3-a_4\right)=0;$$

$$q_2=C\left(\frac{\sqrt{2}}{2}a_0+0a_1-\frac{\sqrt{2}}{2}a_2-a_3-\frac{\sqrt{2}}{2}a_4+0a_3+\frac{\sqrt{2}}{2}a_2+a_1\right)=C\frac{\sqrt{2}}{2}\left(a_0-\sqrt{2}a_3-a_4+\sqrt{2}a_1\right)=0.$$

The symmetry condition apparently means that all other unbalances also equal zero. In the same way, we can show that satisfaction of condition (4) signifies that the eight-zone LAR—LIC system does not monitor the second azimuthal harmonic. Satisfaction of condition (5) signifies that the third harmonic is not monitored, while satisfaction of condition (6) signifies that the fourth harmonic is not monitored.

Consequently, the determinant of matrix A is inverted to zero only when specially selected weighting coefficients are chosen to satisfy conditions (3)-(6). Specifically, within the framework of the "harmonic" regulator idea [4], it is proposed to segregate one or two low azimuthal harmonics, and having suppressed them, ignore the higher harmonics. When applied to an LAR—LIC system, this idea is also realized in the form of weighted summation, the so-called "harmonic" method of weighting, apparently leading to coefficients that correspond to conditions (5), (6).

Let us consider the case in which the weighting coefficients vary in accordance with exponential law (2). Figure 4 expresses the relationship of the determinant of matrix A and coefficient η. The determinant obviously varies in the range 0-1, equalling zero only when $\eta = 0$. This signifies that the mathematical problem of determining stability when weighted summation is introduced is equivalent to this same problem for an LAR—LIC system without weighting coefficients, i.e., the conditions for stability with exponential weighting and without weighting are identical.

We should distinguish between the practical and formal-mathematical aspects of those results. For example, when η is very small but not equal to zero, $A\Phi = 0$ only when $\Phi = 0$, even though the weighting coefficients are virtually identical under these conditions. In fact, Q also equals zero with a finite degree of accuracy (when a dead zone exists), and for small values of η the system behaves in exactly the same way as for $\eta = 0$; i.e., when there is a

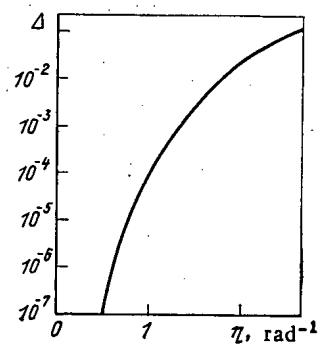

Fig. 4. Relationship of determinant of matrix A to η.

dea an analysis carried out on the supposition of no dead zone at all.

A system possessing the required practical effectiveness, both in its plan for processing disturbances and from the viewpoint of stabilizing unstabilized field motions, can be obtained for specific combinations of η and δ. With regard to the condition of achieving accuracy of regulation while maintaining a permissible frequency of operation of the control-rod drives, a value of δ equal to about 1% is usually chosen. As we have seen already, the quality of processing disturbances at such a value of δ demands a value of $\eta \approx 1.0$, since the dispersion virtually coincides with the asymptote corresponding to no weighted summation for this combination of η and δ. This also signifies that the ability to monitor the high harmonics and, consequently, the effectiveness of the field stabilization are virtually unaffected by the presence of the weighted summation process.

Consequently, our analysis confirms that the introduction of weighted summation effectively enhances the operational properties of an LAR–LIC, provided certain conditions are satisfied. Specifically, it allows us to:

improve the reaction of an LAR–LIC to disturbances close to the chambers and simplifies dialog between the operator and the LAR–LIC system during manual regulation of energy distribution;

monitor any possible drift in the sensitivities of the measurement channels and reduce mistaken increases in reactor power during falls in channel sensitivity;

achieve these advantages and maintain a high level of system effectiveness in a plan for stabilizing unstable energy distributions, by selecting a specific combination of dead-zone width ($\delta \approx 1\%$) and decay constant ($\eta \approx 1$ rad^{-1}) of weighting coefficient.

LITERATURE CITED

1. I. Ya. Emel'yanov, L. N. Podlazov, A. N. Aleksakov, et al., "Synthesizing a system for stabilizing energy distribution and controlling reactor power, based on lateral ionization chambers," At. Energ., 56, No. 1, 11-15 (1984).
2. I. Ya. Emel'yanov, L. N. Podlazov, A. N. Aleksakov, and V. M. Panin, "Synthesizing zonal-asymmetrical systems of automatic energy-distribution regulation for a reactor," At. Energ., 47, No. 6, 370-373 (1979).
3. I. Ya. Emel'yanov, L. N. Podlazov, A. N. Aleksakov, et al., "Synthesizing a system of local automatic regulation for power reactors," At. Energ., 53, No. 5, 301-305 (1982).
4. P. T. Potapenko, "Harmonic regulation of the power of a power reactor," At. Energ., 50, No. 1, 8-13 (1981).

CESIUM MIGRATION IN FUEL ELEMENTS WITH VIBROCOMPACTED OXIDE FUEL WITH GETTER ADDITIVES

V. A. Tsykanov, Yu. M. Golovchenko,
I. G. Lebedev, A. V. Sukhikh, and
A. A. Maershin

UDC 621.039.544.55

It has been established that fission products affect the efficiency of the fuel elements of nuclear reactors. In the first place this applies to chemically active products, among which cesium plays an important role. Numerous domestic and foreign studies point to the participation of this element in corrosion damage of fuel-element cans in reactions between uranium and plutonium oxides.

Model experiments have indicated that at a certain oxygen potential cesium causes corrosion damage to stainless steels, similar to the damage observed in the fuel elements of fast reactors [1, 2]. Studies with the aid of an x-ray microanalyzer confirmed the presence of an increased concentration of this product on the outer surface of the fuel core, in layered zones of the interaction of the fuel with the steel, and at grain boundaries during intercrystalline corrosion of the can of spent fuel elements [3, 4].

The experimental results [5, 6] indicate considerable deformation of the can in the region of spikes of cesium concentration along the length of the fuel element. Extrareactor experiments confirmed the possibility of cesium uranate-plutonates, of a density lower than that of the initial fuel, being formed under certain conditions [7]. The formation of these compounds may lead to the deformation of fuel-element cans. All of this has aroused scientific and technical interest in the study of the physicochemical state and behavior of cesium in oxide fuel. The cesium migration increases upon the introduction of metallic getters into the oxide fuel.

The test fuel elements consisted of OKh16N15M3B austenitic steel tubes filled with powdered uranium oxide with the ratio O/U = 2.00-2.01. Enriched UO_2 was used in the active part and natural UO_2 was used in the reflectors. The getter, in the form of a powder with a particle size of less than 50 μm, was introduced at the rate of ∿5% in relation to the heavy atoms by means of prior mixing with one of the fractions of the UO_2 powder. The fuel elements were irradiated in a BOR-60 reactor at an average thermal load of 40 kW/m to a burn-up of 5%

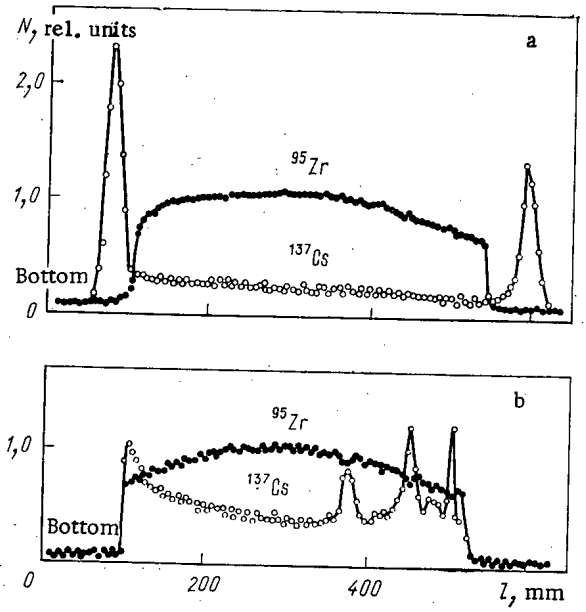

Fig. 1. Distribution of the concentration of fission products over the length of fuel elements with a uranium getter (a) and without a getter (b).

Translated from Atomnaya Énergiya, Vol. 58, No. 1, pp. 12-13, January, 1985.
Original article submitted April 19, 1984.

0038-531X/85/5801-0013$09.50

TABLE 1. Yield of Cesium from the Active Part into the Zone of the Reflectors upon the Introduction of Getters (in %)

Fuel-element No.	Getter material	Cesium yield
1	--	0
2	Cr	5—10
3	Nb	10—15
4	V	10—15
5	Ti	~40
6	Zr	~50
7	U	~50

of the heavy atoms. The concentration of fission products was measured on a semiconductor gamma-spectrometer.

Figure 1 shows how ^{137}Cs and ^{95}Zr are distributed over the height of the fuel column. Data about the influence of the getter material on the yield of ^{137}Cs from the active part of the fuel elements into the zone of the lower and upper reflectors are given in Table 1. The experiments indicate self-purification of the fuel core from cesium when active metals are added to it. It was established that the placement of the getter in the upper and lower reflectors (in the absence of getter in the active part of the fuel column) does not affect the cesium distribution.

When the relative yield of cesium from the fuel core into the reflector (see Table 1) is compared with the values of the oxygen potential of the oxides [8], formed by the metal-getters, a distinct correlation is noted: the lower the oxygen potential of the oxides, the higher the cesium yield. It may be assumed that the introduction of the indicated getters leads to the establishment, in the oxide fuel, of an oxygen potential that corresponds to dynamic equilibrium in the metal—oxide system. This potential determines the chemical state and behavior of the cesium.

Thus, the introduction of metallic getters into the active part of the fuel core is an effective means of acting on the thermodynamic state and behavior of the chemically active fission product cesium.

LITERATURE CITED

1. P. Hoffman and O. Gotzmann, in: Behavior and Chemical State of Irradiated Ceramical Fuels, IAEA, Vienna (1974), p. 237.
2. E. Aitken et al., Trans. Am. Nucl. Soc., 14, No. 1, 176 (1971).
3. K. Perry and C. Craig, Trans. Am. Nucl. Soc., 12, No. 2, 564 (1969).
4. V. A. Tsykanov, E. F. Davydov, E. P. Klochkov, et al., "Study of the physicochemical interaction of oxide fuel with the cans of the fuel elements of a fast reactor," At. Energ., 56, No. 4, 195 (1984).
5. U. Nayak et al., Trans. Am. Nucl. Soc., 19, 113 (1974).
6. V. G. Dvoretskii and A. V. Sukhikh, "Influence of the initial inhomogeneity of the density of vibrocompacted fuel on the state of the cans of test fuel elements irradiated in a fast reactor," Vopr. At. Nauki Tekh. Ser. At. Mater., No. 1(12), 25 (1982).
7. E. Aitken et al., Thermodynamics of Nuclear Materials, Vol. 1, IAEA, Vienna (1975), p. 187.
8. K. Weeks and F. E. Bloch, Thermodynamic Properties of 65 Elements and Their Oxides, Halides, Carbides, and Nitrides [Russian translation], Metallurgiya, Moscow (1965).

ALLOWING FOR THE EFFECTS OF RESIDUAL STRESSES ON CREEP IN CHANNEL TUBES

Yu. N. Knizhnikov, P. A. Platonov, and A. I. Ul'yanov

UDC 621.039.531

Introduction. The walls of channel tubes made of zirconium alloys show residual stresses of the first kind [1] due to the manufacturing technology. It is of interest to consider how these stresses influence the creep, which in some cases determines the working life of the channel tubes or fuel sheaths. Here one expects the stresses to be distributed only over the wall thickness, which is due to the symmetry of the working processes along the length and in azimuth. The residual stress (axial $\sigma_z^0(r)$, circumferential $\sigma_\theta^0(r)$, and radial $\sigma_R^0(r)$) should satisfy the conditions for self-balancing in the bulk as well as the boundary conditions at the walls:

$$\int_{R_1}^{R_2} \sigma_z^0(r')\, r'\, dr' = 0,$$

$$\int_{R_1}^{R_2} \sigma_\theta^0(r')\, dr' = 0, \quad \sigma_R^0(R_1) = \sigma_R^0(R_2) = 0, \tag{1}$$

in which

$$\sigma_R^0(r) = \frac{1}{r}\int_{R_1}^{r} \sigma_\theta^0(r')\, dr',$$

where R_1 and R_2 are the internal and external radii.

The integral self-balancing conditions should also be obeyed in various mechanical operations on the items, where there will be the corresponding stress redistribution. Methods of measuring the residual-stress distributions in tubular specimens are based on this, for example, the ring and band deformation method [2]. It is also possible to use x-ray methods.

As an example, Figs. 1 and 2 show the measured distributions of σ_θ^0 and σ_x^0 in the walls of two high-powered water-cooled channel reactor (RBMK) channel tubes, which are characterized by concentration of the tensile stresses at the outer wall. Conditions (1) are obeyed in both cases. The dashed lines show the stepped distributions approximating the positive and negative parts of the distribution curves 1 and 2, respectively.

Methods of Calculating Creep with Allowance for Residual-Stress Relaxation. The creep strain is considered for the working conditions for RBMK channel tubes [3]. The creep rate of the zirconium alloy [4] in the absence of internal stresses is described by a superposition of thermal and radiation components:

$$\dot{\varepsilon}_0\,[\text{h}^{-1}] = 7.2\cdot10^{-2}t^{-0.68}\operatorname{sh}\left(\frac{9.85s\sigma}{T}\right)\exp\left(-\frac{4575}{T}\right) + 3.7\cdot10^{10}\operatorname{sh}\left(\frac{21.1\sigma}{T}\right)\exp\left(-\frac{26000}{T}\right) + 1.135\cdot10^{-21}\varphi\sigma\exp\left(-\frac{6000}{T}\right), \tag{2}$$

where t is time in h, σ is stress in MPa, T is temperature in °K, and φ is neutron flux density, $\text{m}^{-2}\cdot\text{sec}^{-1}$.

Formula (2) has been derived by processing experimental data on the thermal and radiation creep in the tube material under uniaxial load. The factor s in the transient thermal creep component reflects the additional retardation of mobile dislocations by the damage cascades. The important point is that s decreases as the neutron fluence φt increases from s = 1 to the minimum value $s_\infty = 0.385$ at $\varphi t = 3\cdot10^{24}$ m^{-2}.

In calculating the creep in an anisotropic material such as a zirconium alloy, one uses the associated flow law for plastic deformation. The creep anisotropy is specified by the coefficients F, G, and H, which are analogous to the plastic-strain anisotropy coefficients

Translated from Atomnaya Énergiya, Vol. 58, No. 1, pp. 13-17, January, 1985. Original article submitted February 2, 1984.

0038-531X/85/5801-0015$09.50

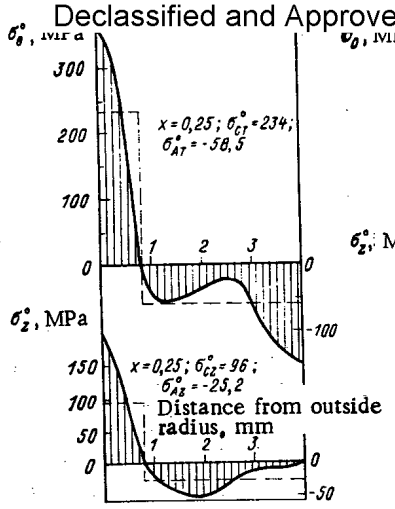

Fig. 1

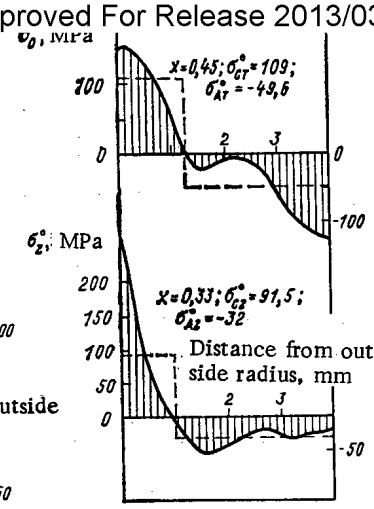

Fig. 2

Fig. 1. Patterns of the circumferential and axial residual stresses (type 1 distribution).

Fig. 2. Patterns of the circumferential and axial residual stresses (type 2 distribution).

introduced by Hill [5] for tube deformation.

The deviator expressions for the creep rates in the principal directions are

$$\begin{aligned}\dot{\varepsilon}_\theta &= \dot{\varepsilon}_0(\sigma_f)/\sigma_f\,[(F+G)\,\sigma_\theta - G\sigma_z - F\sigma_R];\\ \dot{\varepsilon}_z &= \dot{\varepsilon}_0(\sigma_f)/\sigma_f\,[(G+H)\,\sigma_z - G\sigma_\theta - H\sigma_R],\end{aligned} \tag{3}$$

where $\sigma_f = \sqrt{F(\sigma_R-\sigma_\theta)^2 + G(\sigma_\theta-\sigma_z)^2 + H(\sigma_z-\sigma_R)^2}$ is the effective stress, which defines the creep rate for a combined state of strain. The strain rates for all the principal directions will be defined by the observed creep rate $\dot{\varepsilon}_0(\sigma_f)$ as measured in uniaxial loading (for example, by (2), where one substitutes the corresponding value of σ_f for the uniaxial stress).

The creep anisotropy coefficients were calculated from the texture model TEXTUR. For a typical texture in a channel tube [4], F = 0.10, G = 0.49, H = 0.51; these values were used in the calculations. It is usually assumed that these characteristics are constant over the wall thickness for a given material.

Our task was to devise a method of calculating the strain on the basis of the residual-stress relaxation. The residual stresses add to the stresses from the external pressure in each layer, and so the strains could be appreciably different in uncoupled layers. However, the tube is coupled and continuous, so the strain is consistent in all layers. The corresponding stress relaxation occurs over the section.

One can calculate the strain with detailed incorporation of the relaxing stresses from a model implemented in the RELAXU program. However, the processes involving relaxation can be elucidated qualitatively by considering first a simpler two-layer model implemented in the RELAX2 program. In this model, the real residual-stress distributions are approximated as stepped functions in the layers H_C and H_A ($H_A + H_C = H$):

$$\begin{aligned}\sigma^0_\theta(r) &= \begin{cases}\sigma^0_{\theta C} & R_2 \geqslant r > R_2 - H_C \text{ (layer } C);\\ \sigma^0_{\theta A} & R_2 - H_C \geqslant r \geqslant R_1 \text{ (layer } A);\end{cases}\\ \sigma^0_r(r) &= \begin{cases}\sigma^0_{zC} & R_2 \geqslant r > R_2 - H_C \text{ (layer } C);\\ \sigma^0_{zA} & R_2 - H_C \geqslant r \geqslant R_1 \text{ (layer } A).\end{cases}\end{aligned} \tag{4}$$

Here we have introduced the parameters $x = H_C/H_A$, the ratio of the layer thicknesses, and $y = R_C/R_A$, the ratio of the median radii of the corresponding layers. Then x = 0.25 and y = 1.035 for distribution 1.

On the basis of the balancing conditions (1), we get relationships for the residual stresses in the layers:

$$\begin{aligned}\sigma^0_{\theta A} &= -x\sigma^0_{\theta C}; \quad \sigma^0_{zA} = -xy\sigma^0_{zC};\\ \sigma^0_{RA} &= y\sigma^0_{RC}; \quad \sigma^0_{RC} = Q\sigma^0_{\theta C},\end{aligned} \tag{5}$$

To calculate the strain increments in the circumferential and axial directions ($\Delta\varepsilon_\theta$, $\Delta\varepsilon_z$) occurring in a time interval Δt, we adopt the planar-section hypothesis:

$$\Delta\varepsilon_z = C = \text{const (over the cross section)} \tag{6}$$

and the condition for volume conservation during creep:

$$\Delta\varepsilon_\theta + \Delta\varepsilon_z + \Delta\varepsilon_R = 0. \tag{7}$$

To obey (6) and (7), we introduce the residual-stress relaxation in a step Δt, with the stress changes in the layers related by (5). The actual principal stresses in the layers with the additive increments are used to calculate the effective stresses in the layers σ_{fC} and σ_{fA} of (3), together with the corresponding deviators. Then from (3) we calculate the increments in the strain for the free layers, namely: $\varepsilon_{\theta C} = \dot{\varepsilon}_{\theta C}\Delta t$, $\varepsilon_{zC} = \dot{\varepsilon}_{zC}\Delta t$, etc.

From the conservation of the planar section for the tube of (6) we get that the axial strains in both layers are consistent, and therefore it is necessary to include fictitious elastic strains in order to allow for the residual-stress relaxation [2]. We have from (6) that

$$\Delta\varepsilon_z = C = \varepsilon_{zC} + \frac{\Delta\sigma^0_{zC}}{E} - \frac{\mu}{E}(\Delta\sigma^0_{\theta C} + \Delta\sigma^0_{RC}) = \varepsilon_{zA} + \frac{\Delta\sigma^0_{zA}}{E} - \frac{\mu}{E}(\Delta\sigma^0_{\theta A} + \Delta\sigma^0_{RA}). \tag{8}$$

Another expression is obtained for the circumferential strain from the volume conservation of (7). Then we use (8) and introduce the stress relaxation to express the circumferential creep strain for the outer radius of the tube R_2 in terms of the strains for the median radii of the layers R_C and R_A:

$$\begin{aligned}\Delta\varepsilon_\theta(R_2) &= \frac{R_C^2}{R_2^2}\left[\varepsilon_{\theta C} + \frac{\Delta\sigma^0_{\theta C}}{E} - \frac{\mu}{E}(\Delta\sigma^0_{zC} + \Delta\sigma^0_{RC})\right] - \frac{R_2^2 - R_C^2}{2R_2^2}\left[\varepsilon_{zC} + \frac{\Delta\sigma^0_{zC}}{E} - \frac{\mu}{E}(\Delta\sigma^0_{\theta C} + \Delta\sigma^0_{RC})\right] = \\ &= \frac{R_A^2}{R_2^2}\left[\varepsilon_{\theta A} + \frac{\Delta\sigma^0_{\theta A}}{E} - \frac{\mu}{E}(\Delta\sigma^0_{zA} + \Delta\sigma^0_{RA})\right] - \frac{R_2^2 - R_A^2}{2R_2^2}\left[\varepsilon_{zA} + \frac{\Delta\sigma^0_{zA}}{E} - \frac{\mu}{E}(\Delta\sigma^0_{\theta A} + \Delta\sigma^0_{RA})\right].\end{aligned} \tag{9}$$

We solve (8) and (9) with (5) to express the stress relaxation in terms of the differences of the calculated strains in the free layers:

$$\begin{aligned}&\frac{\Delta\sigma^0_{\theta C}}{E} = \frac{P_1}{\Delta}\Delta_1 + \frac{P_2}{\Delta}\Delta_2; \\ &\Delta_1 = \varepsilon_{\theta A} - y^2\varepsilon_{\theta C} - \beta_A\varepsilon_{zA} + \beta_C\varepsilon_{zC}; \\ &\frac{\Delta\sigma^0_{zC}}{E} = \frac{P_3}{\Delta}\Delta_1 + \frac{P_4}{\Delta}\Delta_2; \quad \Delta_2 = \varepsilon_{zA} - \varepsilon_{zC}; \\ &\beta_A = \frac{1}{2}\left(\frac{R_2^2}{R_A^2} - 1\right); \quad \beta_C = \frac{1}{2}y^2\left(\frac{R_2^2}{R_C^2} - 1\right),\end{aligned} \tag{10}$$

where $P_1 = 1 + xy$; $P_2 = \mu y(x + y) + \beta_C + xy\beta_A$; $P_3 = \mu[1 + x + Q(1 - y)]$; $P_4 = x + y + \mu(\beta_C + x\beta_A) + \mu Q(y^2 - y + \beta_C - y\beta_A)$; $\Delta = P_1P_4 - P_2P_3$.

We see that the relation in all cases tends to reduce the disequilibrium produced by the residual stresses, while the relaxation rate at any instant is determined by the difference in the calculated strains for the contacting layers.

On substituting (10) into (8) and (9), we get expressions for the creep deformations:

$$\begin{aligned}\Delta\varepsilon_\theta(R_2) = \left(\frac{R_C}{R_2}\right)^2 &\left\{\varepsilon_{\theta C} - \frac{\beta_C}{y^2}\varepsilon_{zC} + \frac{\Delta_1}{\Delta}\left[P_1\left(1 + \frac{\beta_C\mu}{y^2} - \mu Q\left(1 - \frac{\beta_C}{y^2}\right)\right) - P_3\left(\mu + \frac{\beta_C}{y^2}\right)\right] + \right. \\ &\left. + \frac{\Delta_2}{\Delta}\left[P_2\left(1 + \frac{\mu\beta_C}{y^2} - \mu Q\left(1 - \frac{\beta_C}{y^2}\right)\right) - P_4\left(\mu + \frac{\beta_C}{y^2}\right)\right]\right\};\end{aligned} \tag{11a}$$

$$\Delta\varepsilon_z = \varepsilon_{zC} + \frac{\Delta_1}{\Delta}[P_3 - \mu(1 + Q)P_1] + \frac{\Delta_2}{\Delta}[P_4 - \mu(1 + Q)P_2]. \tag{11b}$$

For a thin-walled tube, $y \approx 1$ (β_C, β_A, $|Q| \ll 1$); then (11a) and (11b) simplify to

$$\Delta\varepsilon_\theta(R_2) = \frac{\varepsilon_{\theta C}x}{1+x} + \frac{\varepsilon_{\theta A}}{1+x}; \qquad \Delta\varepsilon_z = \frac{\varepsilon_{zC}x}{1+x} + \frac{\varepsilon_{zA}}{1+x}. \tag{12}$$

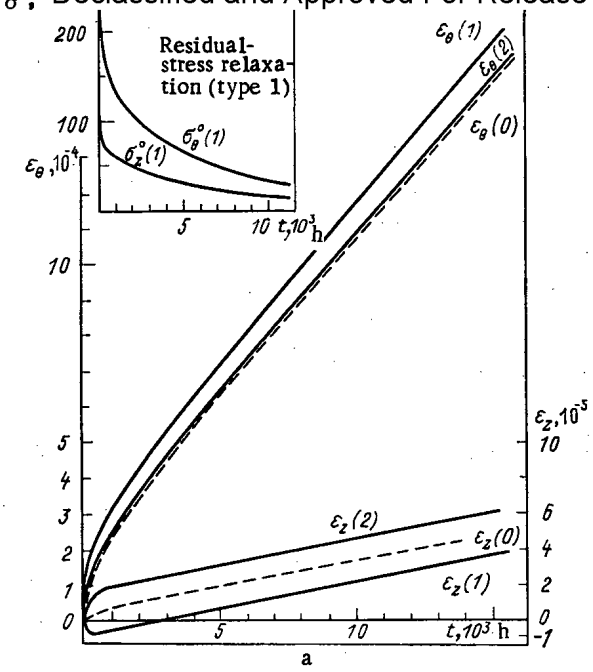

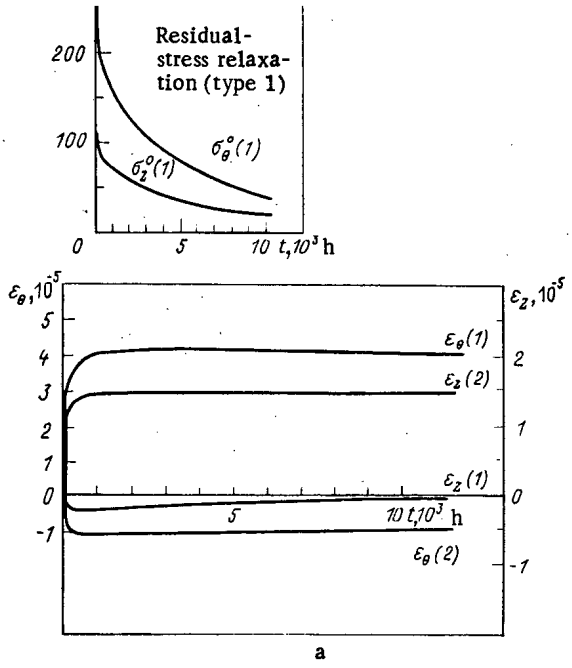

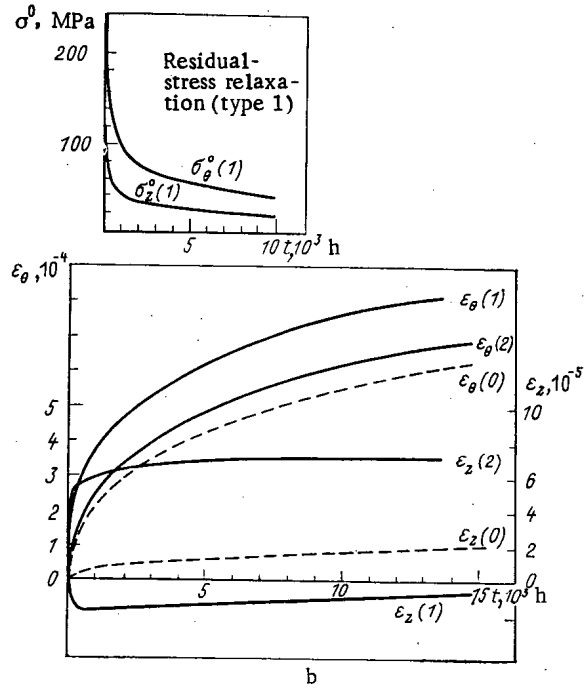

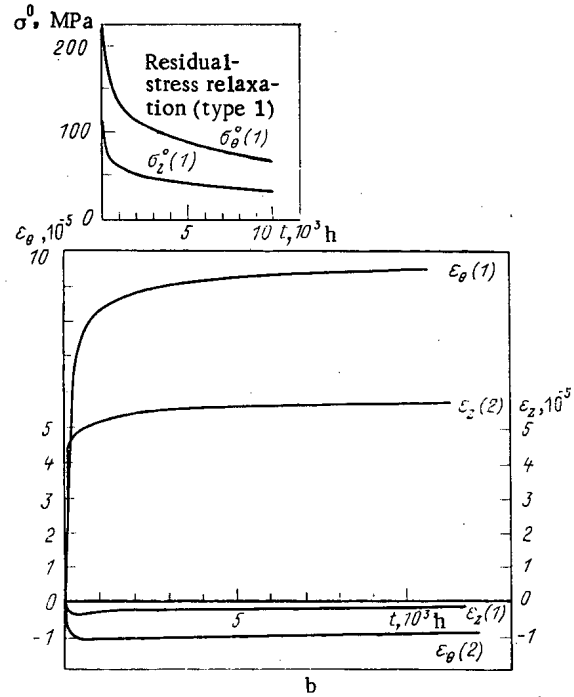

Fig. 1

Fig. 2

Fig. 3. Effects of residual stresses on creep in channel tubes (distributions 1 and 2) at a coolant pressure of 7.5 MPa: a) fast neutron flux density 10^{17} $m^{-2} \cdot sec^{-1}$; b) no irradiation.

Fig. 4. Deformation of channel tubes due to residual stresses alone (distributions 1 and 2): a) fast neutron flux density 10^{17} $m^{-2} \cdot sec^{-1}$; b) no irradiation.

If there are no residual stresses and there is no temperature gradient, when $\varepsilon_{\theta C} = \varepsilon_{\theta A} = \varepsilon_\theta$, we get the usual case of free layer deformation. In the general case, however, the resultant strain is determined by the calculated strains averaged over the section for the free layers. These expressions enable one to evaluate the effects of various residual-stress distributions on the deformation.

means of a model for the stress–strain state in a fuel pin having close contact between the core and the sheath [6]. Here we considered a sleeve fuel core of size from R_1 to R_2 and a thin outer sheath. The thickness of the fuel core was divided into a finite number of layers, and an iterative procedure was used to solve for the strain for a set of radial coordinates. We considered strains of different types: thermoelastic strains accompanied by fuel swelling, which give volume deformation $\Delta\varepsilon_V$, and also inelastic creep and plastic strain, for which the volume is conserved, i.e., $\Delta\varepsilon_\theta^C + \Delta\varepsilon_z^C + \Delta\varepsilon_R^C = 0$. Then we use the planar-section hypothesis, i.e., $\Delta\varepsilon_z = C = \text{const}$ over the section of the fuel and sheath.

We use this method to determine the deformation in a channel tube containing residual stresses, where we made the following assumptions for the model implemented in the RELAXU program. Instead of the sleeve core, we considered a zirconium tube, while the outer sheath was taken as negligibly thin and soft. The tube wall thickness was split up into 12 layers, i.e., we considered the conforming strain at 13 radial points. The wall material was taken as anisotropic as regards creep, which was defined by specifying the creep anisotropy coefficients F, G, and H. In principle, we can specify a distribution for these coefficients if necessary and also distributions for other characteristics such as the temperature over the cross section, which may substantially influence the relaxation and deformation in the layers.

The time step was chosen automatically, and for each radial coordinate $R_1 \leqslant R_i \leqslant R_2$ we calculated the creep via (3) for anisotropic creep flow. Here the residual stresses $\sigma_\theta^\circ(R_i)$, $\sigma_z^\circ(R_i)$, $\sigma_R^\circ(R_i)$ appear in the values for the principal stresses for the radial coordinates.

The contact conditions give three linear equations defining the parameters $C = \Delta\varepsilon_z$, $\Delta\varepsilon_\theta(R_2)$ for each stage, together with the constant D, from which one can calculate the strain distribution over the points R_i and the corresponding stress relaxations $\Delta\sigma_\theta^\circ$, $\Delta\sigma_z^\circ$, $\Delta\sigma_R^\circ$ [6]. The absolute values and signs of these relaxations will vary over the layers, but the self-balancing conditions are automatically obeyed. During the calculation, the residual-stress distribution alters, and in accordance with (10) we find that the greatest relaxation occurs in the regions were the stresses change sharply.

To isolate the inelastic creep strain, we subtract the thermoeleastic component from the total strain, this component being attained during the heating period C_1. The time conditions for heating C_1, constant temperature C_2, and cooling C_3 were specified.

Results. Figures 3 and 4 show the results on the creep for typical characteristics of channel-tube materials [4]. In all cases, the constant wall temperature of 300°C was assumed. The time required to attain stationary conditions was 24 h. We show the time course of the circumferential inelastic strain ε_θ and the axial component ε_z for residual-stress distributions of types 1 and 2, as indicated by the numbers on the corresponding curves. The coolant pressure was 7.5 MPa [3]. The dashed lines show the calculated strain curves without residual stresses. The residual stresses make themselves felt in a certain increase in the circumferential strain, particularly for the type 1 distribution. The effects of the residual stresses on the much smaller axial strains are substantially less. For example, the axial strains become negative for distribution 1. For distribution 2, there is a positive increase, particularly in the absence of irradiation.

The stress-relaxation curves show that there is a substantial contribution from the unsteady thermal creep, which effectively operates in the initial period, when the stresses are large. Here the factor s plays an important part, which describes the dislocation retardation by cascades. This factor begins to have an effect after a few dozen hours, and it reduces the relaxation rate for the irradiated material. Correspondingly, the strain rate is reduced in the initial period. At large times, the thermal creep rate is substantially less than the radiation one, and then the strain is determined by the latter.

Figure 4 gives the corresponding strain curves for tubes without external pressure, i.e., due to the residual stresses alone. Here the distribution type has a more pronounced effect, since there is no smoothing factor due to the external stresses. For example, $\varepsilon_\theta(1) > 0$ and $\varepsilon_z(1) < 0$, whereas $\varepsilon_z(2) < 0$ and $\varepsilon_z(2) > 0$.

The stress relaxation is particularly rapid in the initial period, when the strain differences for the layers are given by (10) as particularly large. After a period of rapid relaxation (less than 10^3 h), the strain attains a limit. Here the s factor also makes itself felt by decreasing the contribution from the unsteady thermal creep due to irradiation.

 tures with allowance for the relaxation of the residual stresses distributed over the wall thickness in the presence of radiation and temperature fields. The result for RBMK channel tubes is that the residual stresses have only a minor effect on the strain in prolonged operation. However, in short-time tests, this factor may appreciably distort the results and may even alter the sign of the strain. The internal stresses may also make themselves felt when one measures the strain due to radiation growth in zirconium-alloy specimens.

LITERATURE CITED

1. A. A. Pozdeev, Yu. I. Nyashin, and P. V. Trusov, Residual Stresses [in Russian], Nauka, Moscow (1982).
2. N. A. Birger, Residual Stresses [in Russian], Mashgiz, Moscow (1963).
3. N. A. Dollezhal' and I. Ya. Emel'yanov, The Channel Nuclear Power Reactor [in Russian], Atomizdat, Moscow (1980).
4. V. Goncharov, P. Platonov, A. Ivanov, and I. Frolov, J. Nucl. Mater., 90, 224 (1980).
5. R. Hill, The Mathematical Theory of Plasticity [Russian translation], Gostekhizdat, Moscow (1957).
6. Yu. I. Likhachev and V. Ya. Pupko, Strength in Fuel Elements in Nuclear Reactors [in Russian], Atomizdat, Moscow (1975), pp. 138-141.

EFFECT OF DIFFUSION ON THE SELECTIVE SPUTTERING OF COMPOSITE MATERIALS ON A CARBON BASE WITH HYDROGEN IONS

M. I. Guseva, A. M. Izmailov, V. V. Kuchinskii, Yu. V. Nikol'skii, and V. A. Stepanchikov

UDC 621.039.63:661.66.665

Owing to the relatively low coefficient of sputtering [1] and the stability towards thermal shock, composite materials (carbon base—metal carbide) are considered promising as stopping diaphragms and a shield in thermonuclear fusion facilities. At a temperature of about 300°K, when the role of diffusion processes is small and with strongly differing coefficients of cathode sputtering, enrichment of the surface with atoms of a difficultly atomized element occurs. Heating up of composite materials during irradiation can lead to a significant redistribution of the components due to diffusion processes.

In the present paper, the effect of diffusion was studied on the erosion properties and the distribution of the metal concentration and carbon in the surface layer of a niobium target, irradiated with hydrogen ions with energy 10 keV at a different temperature. The coating of NbC was deposited on a graphite backing by the gas-diffusion method. Bombardment with H^+ ions was conducted in the ILU-3 ion accelerator [3]. In all experiments, the ion current density amounted to 30 μA/cm² and the irradiation dose was $\sim 10^{19}$ cm^{-2}. The surface of the samples, before and after irradiation, was analyzed by the Auger-spectroscopy method with simultaneous etching of the surface layers with relatively low-energy Ar^+ ions (2 keV), which allowed the distribution of the metal and carbon concentrations to be obtained over the depth of the target.

The basic equation describing the rearrangement process of the surface of a two-component material by the action of ion bombardment [2], applicable to modeling of the interaction of a plasma with the surface by means of the ion beam, can be represented in the form

$$\frac{\partial \rho_1}{\partial t} = \frac{\partial}{\partial \xi}\left\{ g \frac{\partial \rho_1}{\partial \xi} + Nh^2 \left[(S_{01} - S_{02}) \int_0^{\varphi} \rho_1 \, d\varphi' + S_{02}\varphi \right] \rho_1 - \right.$$

$$\left. - Nh^2 S_{01} \int_0^{\varphi} \rho_1 \, d\varphi' \right\} - \frac{\partial^2 \rho_1}{\partial \xi^2} \frac{Nh^2}{2} \left[(S_{01} - S_{02}) \int_{\varphi}^{1} \rho_1 \, d\varphi' + S_{02}(1-\varphi) \right], \quad (1)$$

Translated from Atomnaya Énergiya, Vol. 58, No. 1, pp. 18-20, January, 1985. Original article submitted March 14, 1984.

 0038-531X/85/5801-0020$09.50

where $g \equiv D/h^2 + ue^{-\alpha\xi} + Nh^2[(S_{01} - S_{02})\int_0^\varphi \rho_1 d\varphi' + S_{02}]/2$, $\rho_1 \equiv \rho_1(\xi, t)$ is the relative concentration of the easily sputtered component of the material ($\rho_2 = 1 - \rho_1$); ξ is a running coordinate, reckoned from the boundary of the solid in units of distance between atomic layers h; t is the time; N is the ion flux on unit area of the surface being sputtered; S_{01} and S_{02} are the coefficients of sputtering of the easily and difficultly atomized components before the start of the ion bombardment, converted to 100% content of the component in the material; $\varphi = \int_0^\xi f(\xi')d\xi' = 1 - e^{-\beta\xi}$; $f(\xi) = \beta e^{-\beta\xi}$ is the normalized function describing the distribution with respect to depth ξ of the sputtering power of the ion flux; $\beta = h/H_{dsp}$ (H_{dsp} is the characteristic depth of the region of sputtering); $ue^{-\alpha\xi}$ ($\alpha = h/H_{mix}$) is the distribution with respect to depth of the probability of exchange with the sites of atoms of the different components under the action of collision cascades; H_{mix} is the characteristic depth of the region of effective intermixing; D is the coefficient of diffusion. The boundary condition for solving Eq. (1) can be written in the form of an equation of balance of the particle flux of the easily atomized component through an area infinitely distant from the surface of the solid [4]:

$$N[S_1(t) + S_2(t)]\rho_{01} = NS_1(t) + h^{-2}\int_0^\infty (\partial\rho_1/\partial t)\, d\xi', \tag{2}$$

where $S_k(t) = S_{0k}\int_0^\infty f(\xi')\rho_k(\xi', t)\, d\xi' = S_{0k}\int_0^1 \rho_k d\varphi'$ is the selective coefficient of sputtering of the k-th component; ρ_{0k} is the relative concentration of the k-th component in the original material. At the initial instant, $S_k(0) = S_{0k}\rho_{0k}$. In the steady sputtering regime ($\partial\rho_1/\partial t = 0$), we obtain from Eq. (2) the expressions for the selective sputtering coefficients $\tilde{S}_k$ and the total sputtering coefficient $\tilde{S}$:

$$\begin{aligned} \tilde{S}_k &\equiv S_k(t)\,|_{t\to\infty} = \rho_{0k}\tilde{S}; \\ \tilde{S} &\equiv \tilde{S}_1 + \tilde{S}_2 = [\rho_{01}/S_{01} + \rho_{02}/S_{02}]^{-1}, \end{aligned} \tag{3}$$

whence $\tilde{S}_1/\tilde{S}_2 = \rho_{01}/\rho_{02}$ when $t \to \infty$. The second boundary condition is obvious: $\rho_k(\xi, t)\,|_{\xi\to\infty} = \rho_{0k}$.

It is well known that with an energy of several keV and above, the probability of the intermixing process u and the effective region of intermixing H_{mix} are considerably greater than the probability $Nh^2\tilde{S}$ and the region of sputtering H_{dsp} respectively (usually limited to 2-4 layers): $u >> Nh^2\tilde{S}$ and $H_{max} >> H_{dsp}$. Therefore, as the estimates show, the contribution of the last term (with $\partial^2\rho_1/\partial\xi^2$) in Eq. (1) is insignificant by comparison with $g(\partial^2\rho_1/\partial\xi^2)$, and this term can be neglected.

It can be supposed that sputtering occurs only from the first near-surface layer (or from the first 2-3 layers, within the limits of which sputtering can be described by an averaged characteristic). In the deeper layers, rearrangement is achieved due to diffusion and intermixing conversions under the action of collision cascades. The hypothesis about the surface nature of sputtering leads to the following formula:

$$S_1 = S_{01}\int_0^\varphi \rho_1 d\varphi, \tag{4}$$

and we assume approximately that S_1 is close to the steady-state value of $\tilde{S}_1$. The simplifications introduced only slightly affect the accuracy of the final result, but allow an analytical solution to be obtained of the very complex Eq. (1) with the boundary conditions (2) and $\rho_k(\xi, t)\,|_{\xi\to\infty} = \rho_{0k}$ by the Laplace transform method with the initial condition $\rho_1(\xi, 0) = \rho_{01}$.

The distribution of the relative concentration of the easily atomized component $\rho_1(\xi, t)$ in space and time is obtained in the form

$$\rho_1(\xi, t) \equiv \rho_{01}\{1 + [\rho_1(\xi)/\rho_{01} - 1]\, Q(\xi, t)\}, \tag{5}$$

where $\rho_1(\xi)$ is the solution of the steady-state Eq. (1) for $\partial\rho_1/\partial t = 0$:

$$\rho_1(\xi) = \rho_{01}\left\{1 + \left(\frac{\tilde{S}}{S_{01}} - 1\right)\exp\left[-\frac{Nh^2\tilde{S}}{g_0}\left(\xi + \frac{1}{\alpha}\ln\frac{g_0 + ue^{-\alpha\xi}}{g_0 + u}\right)\right]\right\}. \tag{5a}$$

Here, $g_0 = D/h^- + Nh^-S/2$, and the function $Q(\xi, t)$ is given by the equation

$$Q(\xi, t) = \{bP(z+y) + (b-1)P(y-z) - (2b-1)\ P[z(2b-1)+y]\}\ \exp[-(y-z)^2]/(2b-2). \qquad (5b)$$

The following notations are introduced for brevity: $b \equiv \frac{S_{01}S_{02}}{\tilde{S}^2[1+u\alpha/(Nh^2\tilde{S})]}$; $y \equiv \xi/\sqrt{4t(g_0+u)}$; $z \equiv (Nh^2\tilde{S} + u\alpha)\sqrt{t/(g_0+u)}/2$; $P(z) \equiv [1 - \Phi(z)]e^{z^2}$; $\Phi(z)$ is the integral of the errors. The function P(z) or $z \gg 0$ is approximated by a simple polynomial [5]. As, in the model, sputtering from the surface ($\xi = 0$) is being considered, the selective coefficients of sputtering are calculated by the obvious formulas

$$S_1(t) = S_{01}\rho_1(0, t) = \rho_{01}[S_{01} + (\tilde{S} - S_{01})Q(0, t)];$$
$$S_2(t) = S_{02}[1 - S_1(t)/S_{01}], \qquad (6)$$

whence it can be seen that the change of the selective coefficients of sputtering is determined by the function Q(0, t) represented in Fig. 1 for different values of the parameter $b = S_{01}S_{02}/\tilde{S}^2[1 + u\alpha/(Nh^2\tilde{S})]^{-1} = S_1(0)S_2(0)/\tilde{S}_1\tilde{S}_2[1 + u\alpha/(Nh^2\tilde{S})]^{-1}$, which is proportional to the ratio of the derivative of the selective coefficients of sputtering before rearrangement to their derivative after rearrangement. Formula (6) and the nomogram in Fig. 1 allow the changes of the selective coefficients of sputtering of the two-component material to be estimated.

A qualitative interpretation of the changes of composition of the samples versus the temperature can be carried out easily by means of the nomogram in Fig. 1, from which it can be seen that the coefficient of selective sputtering (and, corresponding to it, the concentration of the surface layer) reaches a steady value (for $b \approx 3$) with $z \approx 0.5$ [$z \approx Nh^2S\sqrt{t/(g_0 + u)}$]. At a low temperature, the parameter g_0 is relatively small and even at low irradiation doses, $z \approx 0.5$. But at a high temperature z is reduced due to a sharp increase of D, which appears in the parameter g_0, and therefore with one and the same irradiation dose, the steady state still will not be achieved rapidly and in the case when $z \ll 1$, the composition of the surface generally will differ but little from the original. According to formula (5), with increase of g_0, the change of the surface concentration involves an even greater number of layers, which retards the establishment of a stationary composition of the surface and of the sputtering regime.

Calculations by formulas (3)-(6) are combined with a choice of values of the input parameters S_{01}, S_{02}, u, and α. In the absence of rearrangement, the selective coefficients of sputtering $S_k(0) = S_{0k}\rho_{0k}$ and, as a comparison of theory with experiment shows, values of S_{01} and S_{02} frequently can be used for pure elements (for example, from [6]). The calculation for the coefficient of sputtering of niobium is given in [7], and the coefficient of sputtering of carbon is approximately a factor of 10 greater. When choosing the parameter α, it can be assumed that the characteristic depth of the region of effective intermixing due to collision cascades H_{mix} is approximately similar to the average depth of penetration of an ion $\bar{H}$, i.e., $\alpha \approx h/\bar{H}$. The value of $\bar{H}$ can be obtained by different methods, for example, it is estimated by the method of calculation in [8]. On the other hand, in the stationary case, the dimensions of the region in which effective rearrangement of the surface layers $\xi_0 h$ has occurred [according to expression (5a) with D = 0)] and the distribution of the concentration of the easily atomized component with respect to depth is described by the expression $\exp[-Nh^2\tilde{S}e^{\alpha\xi}/(u\alpha)]$ amount to approximately $e^{\xi_0 h}Nh^2\tilde{S}\bar{H}/(uh) \approx 2$. If we assume that the dimension $\xi_0 h$ is equal to the average depth of penetration of an ion $\bar{H}$, then in order to estimate the parameter u, we obtain the simple formula $u \approx \bar{H}Nh\tilde{S}$. The diffusion term of the parameter g_0 can be calculated from the value of the coefficient of mutual diffusion D.

In view of the absence of data about the mutual diffusion coefficients of the components for the composite material C — NbC, the standard relation $D \approx D_0\exp(-\Delta e/kT)$ was used for the determination from experimental data of the parameters D_0 and ΔE. The choice of the other parameters was made by the above-stated method. The validity of the relations obtained is confirmed by the coincidence between the experimental data and the results of a calculation by formula (5). The distribution of the components is shown in Fig. 2a for T = 320°K, when the effect of diffusion processes is found to be insignificant and therefore there is no adjusting parameter, but in Fig. 2b and c the coefficients of mutual diffusion $D = 2\cdot10^{-13}$ cm^2/sec for T = 1100°K and $D = 2\cdot10^{-12}$ cm^2/sec for T = 1470°K are determined by comparison of the calculated and experimental data; this corresponds to $D_0 = 2\cdot10^{-9}$ cm^2/sec and ΔE = 20 kcal/mole (for T = 320°K, $D \approx 10^{-23}$ cm^2/sec). The fact that redistribution of the components was observed even at very high temperature values of the sample, when diffusion should have led to quanti-

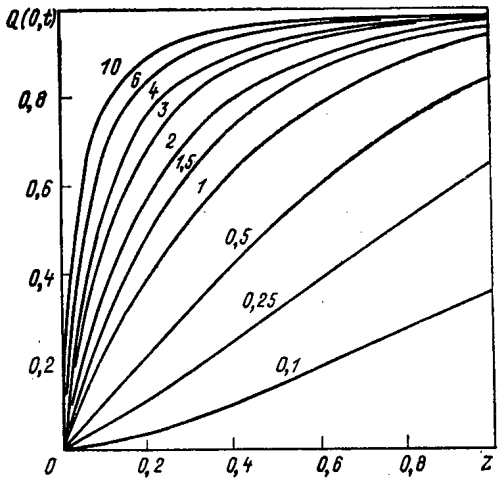

Fig. 1

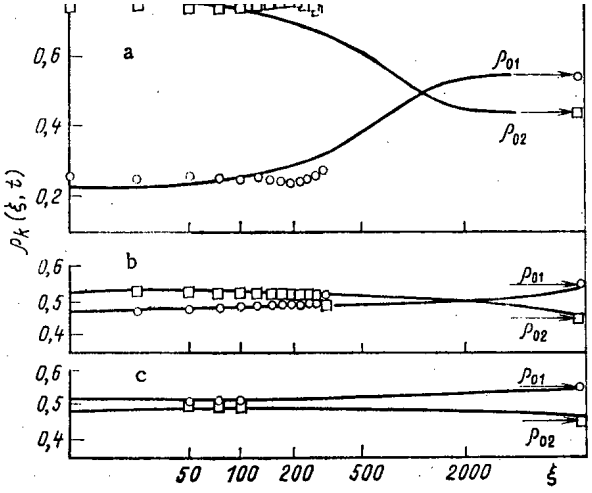

Fig. 2

Fig. 1. Nomogram for the function Q(0, t), determining the dependence on the time of the selective coefficients of sputtering in formula (6). The figures at the curves are the values of the parameter b.

Fig. 2. Distribution of the concentration of metal $\rho_2(\xi, t)$ and carbon $\rho_1(\xi, t)$ with respect to depth ξ for a constant ion irradiation dose at temperature 320 (a), 1100 (b), and 1470°K (c): ○, □) the concentrations of carbon and metal atoms, respectively, calculated by formula (5); ion irradiation dose $2 \cdot 10^{19}$ cm^{-2}.

zation of the composition, testifies to the validity of the values obtained for D. Thus, the formulas obtained allow the change in time and space of the composition of the surface layer of a two-component material and the selective coefficients of sputtering of its components to be calculated in the presence of diffusion. On heating the composite material C — NbC to a temperature >1100°K, almost no rearrangement of the surface or enrichment of the near-surface layers with metal atoms occurs.

LITERATURE CITED

1. M. I. Guseva, A. P. Zakharov, E. S. Ionova, et al., "Graphite and metal carbides as materials for the limiter, shield, and injector plates of a thermonuclear reactor," At. Energ., 51, No. 4, 247 (1981).
2. V. V. Kuchinskii, Poverkhnost'. Fiz. Khim. Mekh., No. 4, 93 (1982).
3. V. M. Gusev, N. P. Busharov, S. M. Naftulin, and A. M. Propichev, Prib. Tekh. Eksp., 4, 19 (1968).
4. A. G. Zhiglinskii, A. M. Izmailov, and V. V. Kuchinskii, in: Sixth All-Union Conference on the Physics of a Low-Temperature Plasma (Collection of Theses) [in Russian], Vol. 1, Leningrad (1983), p. 204.
5. Handbook on Special Functions [in Russian], Nauka, Moscow (1979), p. 120.
6. F. Behrish, in: Sputtering by Particle Bombardment. I: Physical Sputtering of Single-Element Solids, Berlin—New York (1980).
7. M. I. Guseva and Yu. V. Martynenko, Fiz. Plazmy, 2, 593 (1976).
8. K. Nielsen, in: Electromagnetically Enriched Isotopes and Mass Spectrometry, London (1956), p. 68.

AN APPARATUS FOR MEASURING BENDING-STRESS RELAXATION IN REACTORS

G. F. Lepin, N. P. Losev,
A. Ya. Rogozyanov, and B. V. Samsonov

UDC 621.039

It is of interest to measure the stress relaxation at the low strains usually characteristic of fuel-pin sheaths in order to describe the stress–strain state in them and to determine the viability. Such measurements can be combined with other tests to give a more reliable description of the stress–strain state.

It thus is necessary to have an apparatus for relaxation tests on structural materials under irradiation, particularly for the SM-2 and RBT-6 reactors. Some additional specifications had to be met. The transverse dimension of the irradiation device should not exceed 45 mm, while the length of the loading ties should be a few meters. All the operations during the measurements have to be made by remote control and do not allow halts in the tests. It is impossible to place any complex measuring system near the irradiated specimen. The permissible temperature fluctuations are ±5-7°C for the specimen, while those in the components of the irradiation device are ±20-30°C. The radiation resistance of the structural materials should allow one to perform tests at fast-neutron fluxes (E > 0.1 MeV) of 10^{10}-10^{14} $cm^{-2} \cdot sec^{-1}$, temperatures of 300-700°C, and times up to 5000 h. No existing stress-relaxation test method for uniaxial stretching meets these requirements [1, 2].

The method based on specimens in the form of Oding rings [3] is the most suitable for reactor tests. It is then not necessary to place complicated measurement systems in the irradiation zone, since the strain is not neasured but instead is set by the thickness of the loading wedge inserted in the slot in the specimen. Also, the effects of specimen temperature fluctuation are eliminated. It is necessary to reduce all dimensions of the standard Oding ring (about 65 mm) by about a factor 2, but this does not affect the character of the stress–strain state (Fig. 1).

A shortcoming of this method is that in fact one derives the relaxation curve for the bending moment, not the stresses. This required additional development in the method of determining the relaxation characteristics from tests on ring specimens in uniaxial stretching [4, 5]. A balance method of determining the stress was used to ensure continuity in the reactor tests and remote measurement. A monotonically increasing force is applied at the time of measurement to the ends of the specimen from the wedge along the tangent to the average circle, and one determines its value Q at the instant of failure of the electrical contact between the specimen and the wedge. The wedge is made of two metallic parts separated by a thin section of radiation-resistant insulation (Fig. 2). Knowing the force Q [N], which is equal to the reaction of the wedge on the specimen, one can [6] determine the nominal stress σ (in MPa):

$$\sigma = \frac{2r}{W_0} Q = \frac{12r}{bh_0^2} Q = 1{,}029 \cdot 10^8 Q, \qquad (1)$$

where W_0 is the resistance moment of the radial section diametrically opposite the slot, and b and h_0 are the width and thickness of the ring in that section (Fig. 1), which are $2.5 \cdot 10^{-3}$ m. The improved method of [7] enables one to eliminate halts in the tests and to automate the measurements.

The structural scheme for the reactor relaxation tests (Fig. 3) includes the specimen and wedge, the loading device, the electric heater, the load transducer, the thermal measurement transducers, and systems for pneumatic loading, electrical control, and measurement. These systems are located outside the reactor channel, while the other components form the irradiation device. The specimen (Fig. 1) is made with high accuracy in order to provide stress determination with an error of not more than ±2%. The working (thinner) part of the specimen is fitted with three thermal measurement transducers by electrospark welding.

Translated from Atomnaya Énergiya, Vol. 58, No. 1, pp. 21-23, January, 1985. Original article submitted January 13, 1984.

 0038-531X/85/5801-0024$09.50

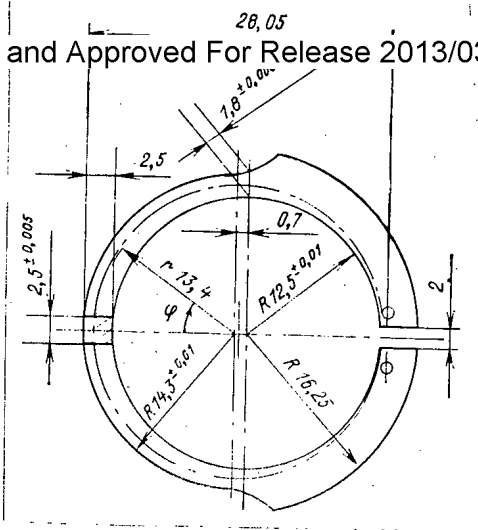

Fig. 1

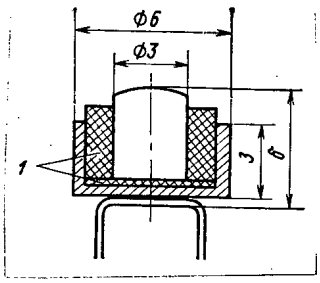

Fig. 2

Fig. 1. Ring specimen for reactor tests.

Fig. 2. Wedge for loading ring specimens: 1) insulating layer.

The wedge design (Fig. 2) provides identical attachment of the lower metal part to the specimen by welding, as well as reliable insulation between the metal parts and monolithic structure after coating with KO-12 organosilicon paint. The electrical connection between the two metal parts of the wedge and the control system is provided by leads welded to it.

The separating force is applied to the specimen at the time of measurement by means of the loading tie, which is connected to the bellows unit in the loading device. Compressed gas is supplied to the bellows from the pneumatic loading system. A reduction valve restricts the pressure to 0.5 MPa. The system provides the required rate of pressure increase (by the use of a throttle and additional vessel in front of the bellows), and the pressure ceases to increase when the contact between the specimen and the upper metal part of the wedge is broken, while the pressure is reduced when the force Q has been measured. The electrical control system provides for loading and unloading the specimen and indicates the execution of the operations, and it also protects the specimen from overload and plastic strain.

To measure the force, the upper part of the tie contains a load transducer near the loading device in the form of a dynamometric transformer transducer of diameter 14 mm and length 177 mm (Fig. 4), which consists of the body 1, differential transformer winding 2, plunger 3, elastic component 6, and additional elastic components 7 to define the zero position of the plunger. The lower end of the tie 4 is connected to the plunger 3, while the upper end 5 is connected to the body 1 of the transducer. When the force is applied to the specimen, the deformation of the elastic element 6 displaces the plunger, which produces a signal in coil 2, which defines the force by means of the standard instrument KSD-2 forming part of the measurement system.

The measurement system also includes an ÉPP-09 multipoint automatic potentiometer to measure the temperature in the specimen by means of the sensors. A VRT-3 regulator controls the electric heater to maintain a given temperature in the specimen.

The system as in Fig. 3 was installed on the SM-2 and RBT-6 reactors in 1982.

Technical Specifications of the Measurement System

Specimen type	Oding ring of reduced dimensions
Number of specimens tested simultaneously	1
Specimen test temperature, °C	300-700
Reduced temperature measurement error, %	
Nominal force, N	40
Force measurement range, N	0-50
Reduced force measurement error, %	±2.0

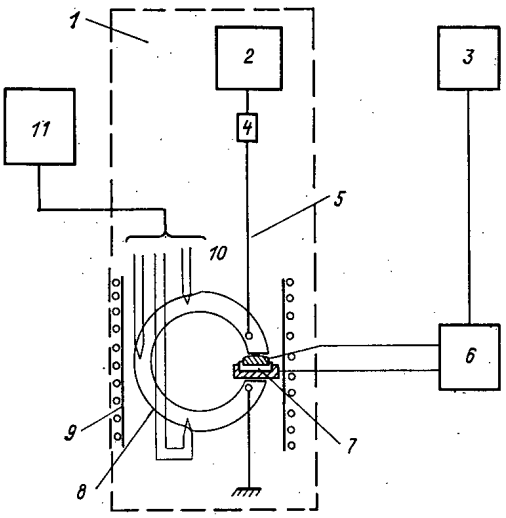

Fig. 3

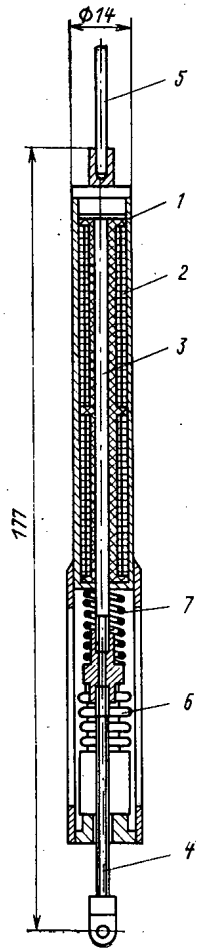

Fig. 4

Fig. 3. Structural diagram of the apparatus for reactor tests on stress relaxation: 1) irradiation device; 2) loading device; 3) pneumatic loading system; 4) load transducer; 5) tie; 6) electrical control system; 7) wedge; 8) specimen; 9) heater; 10) thermal measurement transducer; 11) measurement system.

Fig. 4. Load transducer.

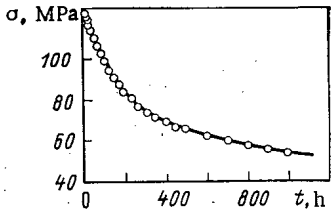

Fig. 5

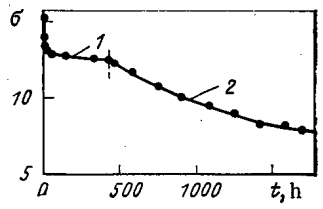

Fig. 6

Fig. 5. Relaxation curve for steel 0Kh16N15M3B.

Fig. 6. Relaxation curve recorded for 0Kh16N15M3B steel without irradiation (1) and under irradiation (2).

Fast neutron flux, $cm^{-2} \cdot sec^{-1}$	10^{10}-10^{14}
Test duration, h	Up to 5000

 made of OKh16N15M3B steel. The first relaxation curve (Fig. 5) was recorded at a fast-neutron flux of $3 \cdot 10^{13}$ $cm^{-2} \cdot sec^{-1}$. This is typical of the stress-relaxation tests.

Also, the calculated initial stress at a given temperature $\sigma_{0,T}$ was equal to the stress $\sigma_{1,T}$ derived from the first measurement of Q when the reactor had been run up to power and the specimen had acquired the required temperature ($\sigma_{0,T} = \sigma_{1,T} = 1.22$ MPa). The value of $\sigma_{0,T}$ was defined by

$$\sigma_{0,T} = \frac{E_T}{E_0} \sigma_0, \tag{2}$$

where σ_0 is the actual value of the initial stress at 20°C, which was determined before the specimen was loaded into the reactor and was 165 MPa, while E_0 and E_T are Young's modulus at 20°C and at the test temperature, which are $2.04 \cdot 10^5$ and $1.51 \cdot 10^5$ MPa, respectively.

The effects of irradiation on the stress-relaxation rate are illustrated by the second relaxation curve for the same specimen (Fig. 6), first part of which characterizes the relaxation outside the reactor, while the second characterizes that in the reactor at the relatively low fast-neutron flux density of $2 \cdot 10^{12}$ $cm^{-2} \cdot sec^{-1}$. The irradiation increased the relaxation rate appreciably. This result agrees with the observed [8, 9] increase in the creep rate for OKh16N15M3B steel specimens at 650°C under irradiation. The stress relaxation and creep are coupled, and the above agreement confirms the qualitative reliability of the test results.

The Oding rings were made from rod supplied by the industry, and when the results are transferred to fuel-pin sheaths (thin-walled tubes), it is necessary to allow for the possible differences in the metal structure.

LITERATURE CITED

1. A. M. Borzdyka, Hot Mechanical Test Methods [in Russian], Metallurgizdat, Moscow (1962).
2. A. M. Borzdyka and L. B. Gertsov, Stress Relaxation in Metals and Alloys [in Russian], Metallurgiya, Moscow (1972).
3. I. A. Oding, "A study of relaxation and creep in metals by means of a ring specimen," in: A New Method of Testing Metals for Relaxation and Creep [in Russian], Mashgiz, Moscow (1949), pp. 5-22.
4. G. F. Lepin and Yu. D. Bondarenko, "Constructing stress-relaxation curves from test results for ring specimens," Probl. Prochn., No. 5, 81-84 (1971).
5. V. N. Rozenblyum, "Relaxation tests on metals," Probl. Prochn., No. 10, 16-19 (1954).
6. I. A. Oding, V. S. Ivanova, V. V. Burdukskii, and V. S. Geminov, The Theory of Creep and Long-Term Strength in Metals [in Russian], Metallurgiya, Moscow (1956).
7. G. F. Lepin, V. F. Gorpinich, B. V. Samsonov, et al., "A method of stress-relaxation testing in bending," Inventor's Certificate No. 896489, Byull. Izobret., No. 1, 196 (1982).
8. G. S. Pisarenko, B. V. Tsykanov, V. N. Kiselevskii, et al., "An experimental study of the effects of reactor radiation on the creep resistance and long-term strength of heat-resisting steels," in: Radiation Effects on the Mechanical Properties of Structural Materials and Methods of Examining Them [in Russian], Naukova Dumka, Kiev (1977), pp. 3-11.
9. N. P. Losev, A. Ya. Rogozyanov, B. V. Samsonov, and A. G. Fin'ko, "Comparative studies on the effects of reactor irradiation on the heat-resistance characteristics of planar, cylindrical, and tubular specimens of 9Kh16N15M3B steel," Fiz. Khim. Obrab. Mater., No. 4, 3-8 (1979).

STRUCTURE OF MOLYBDENUM BOMBARDED WITH LOW-ENERGY HYDROGEN AND HELIUM IONS DURING CREEP TESTS

V. N. Chernikov, I. B. Savvatimova, A. A. Babad-Zakhryapin, and A. P. Zakharov

UDC 669.28:620.187.192:620.172.251.2

High-temperature bombardment with light ions accelerated in the region of the cathode drop of a glow discharge changes the dislocation structure of a metal [1] and affects its behavior during creep tests under uniaxial tension [2]. Specimens of standard shape (diameter of the test section 4 mm) were made from rods of single-crystal molybdenum, oriented along the [111] direction. Below we give the parameters of the creep tests and the conditions of bombardment from a plasma-forming medium (H_2 or an He + H_2 mixture in a 4:1 ratio): T = 1500-1650°C, σ = 0.5-0.8 kg/mm^2, u = 350-500 V, j = 100-150 mA/cm^2. It turned out that the creep resistance in molybdenum specimens, tested under bombardment, is considerably higher than in specimens tested without bombardment (in a vacuum). Under the conditions of the bombardment in this case the curves of the stationary creep rate $\dot{\varepsilon} = \dot{\varepsilon}(\sigma)$ in the range of stresses σ studied were steeper than those obtained during tests in a vacuum. The intersection of the two curves corresponds to $\sigma \cong 0.75$-0.80 kg/mm^2, i.e., at stresses $\sigma < \sigma_0$ ion bombardment leads to hardening of the metal.

To find the causes of the increase in the creep resistance as a result of ion bombardment, methods of high-voltage and analytic transmission electron microscopy were used to make a detailed study of the three-dimensional dislocation structure of specimens of single-crystal molybdenum, deformed without irradiation and under bombardment with low-energy ions from a glow discharge. Foils for transmission electron microscopy (TEM) were prepared from the axial test sections of the molybdenum specimens, which had been earlier subjected to creep tests [2].

Since bombardment with ions from a glow discharge causes bulk changes in the structure of the metal by acting on its surface, it seemed natural to expect the most significant and informative (in relation to an understanding of the phenomenon as a whole) structural changes near the surface. Accordingly, we first made a detailed study of the defect structure of the surface layers in the specimens subjected to bombardment without a mechanical load. For this purpose a series of disk-shaped (diameter 3 mm) single-crystal specimens of molybdenum were prepared [3] and were bombarded with helium and hydrogen ions from a glow discharge (T = 1500°C, τ = 1 h), after which the well-known methods of [4, 5] were used to prepare foils for TEM and their surface structure was studied with the aid of tomography. Most of the foils were examined in JEM-1000 and EM-301 G microscopes at an accelerating voltage of 1 MV and 100 kV, respectively. The three-dimensional dislocation structures of the specimens bombarded in a discharge of H_2 or a mixture of He + H_2 under strain differ considerably from the structures of specimens tested in a vacuum. Figure 1 presents photomicrographs of low-angle boundaries in molybdenum specimens after creep testing without (a, b) and with (c, d) irradiation from a medium of pure hydrogen. Even though the average size ($\sim$100 μm) and shape of the blocks in both specimens are roughly the same, the dislocation structures of the interblock boundaries and the form of the dislocations themselves differ markedly, as can be seen well from the photomicrographs. In the specimen tested under bombardment the dislocations are highly curved, while in block boundaries they are intertwined, often forming pileups that cannot be resolved by TEM. Near block boundaries are dislocation loops of a size of 30-80 nm, whose density varies within wide limits.

Extremely diverse dislocation configurations are formed in specimens that have been bombarded under strain with ions from a glow discharge in an He + H_2 mixture (Fig. 2). The photomicrographs in Fig. 2a, b show a large-cell hexagonal dislocation wall and a wall with elements of tetragonal cells formed in the bombarded specimen under strain. In practically all of the dislocation lines of such walls, including purely screw dislocation lines, a fine serrated structure was detected at higher magnifications. Even larger-celled dislocation walls with a less regular structure are encountered (Fig. 2c) and so are individual phase precipitates of

Translated from Atomnaya Énergiya, Vol. 58, No. 1, pp. 24-27, January, 1985. Original article submitted January 26, 1984.

 0038-531X/85/5801-0028$09.50

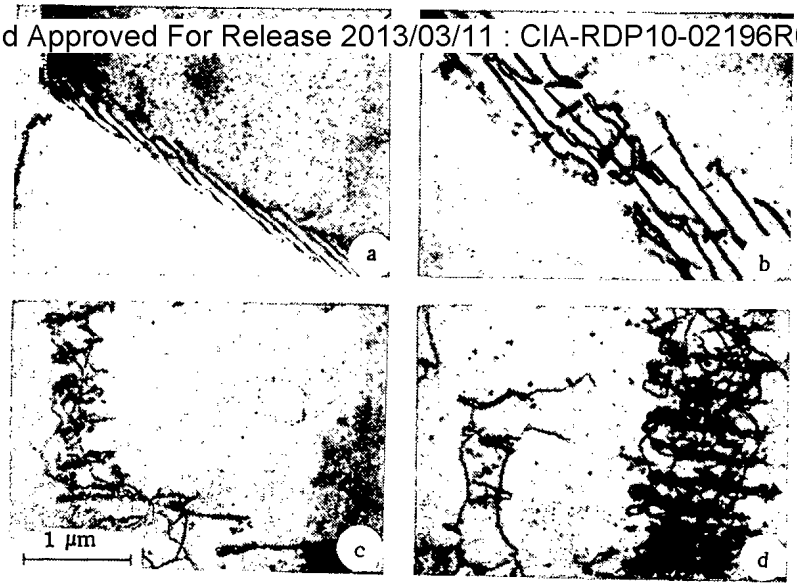

Fig. 1. Low-angle boundaries in the bulk of a molybdenum single crystal after creep testing (T = 1500°C, σ = 5.7 MPa) without bombardment (a, b) and under irradiation from a glow discharge in hydrogen (c, d). The scale is the same in all the photomicrographs.

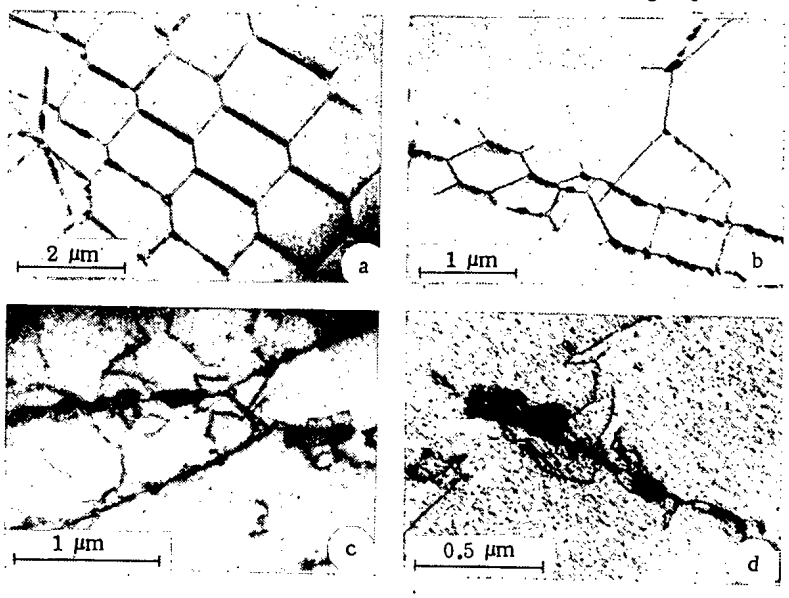

Fig. 2. Dislocation structures in molybdenum single crystals subjected to creep tests (T = 1500°C, σ = 5.7 MPa) under ion bombardment from a glow discharge in a helium–hydrogen mixture.

a size of ∿1 μm with dislocations pinned on them, and they are easily identifiable from their characteristic system of thickness contours (Fig. 2d). It is important to point out that large-celled dislocation walls, characterized by a different degree of perfection, were also found in the central part of cylindrical molybdenum specimens that had been subjected only to high-temperature ion bombardment, without tension (Fig. 3).

Common to all the specimens, bombarded with ions in a discharge under a load as well as without the application of strain, is an increased average dislocation density in comparison with that in specimens that had not been bombarded; an important circumstance in this case is that part of the dislocations are decorated with second-phase particles. The latter follows from analysis of the contrast in such dislocations, which does not vanish in any of the three nonequivalent virtual reflections g of the <110> type, despite the fact that all the images were recorded in the photomicrographs in the two-beam dynamic approximation. Decoration is also indicated by the fine serrated structure of the screw dislocations [6], demonstrating a

strc dislocations or separate parts of them have anomalously wide double images (see Fig. 2a, b), this probably being due to the action, around these dislocations, of additional fields of elastic stresses generated by phase precipitates along the dislocation cores [7]. Direct structural identification of the phase precipitates in the bulk is hindered, but we can assume that this is fcc molybdenum carbide Mo_2C since precisely this compound is often detected on the surface of irradiated specimens by means of the microdiffraction method [3]. When x-ray microspectral probe analysis was carried out in an EM-400T transmission electron microscope with a scanning attachment (which detects elements with $Z > 10$) no elements apart from molybdenum were detected in these phase precipitates, but this does not contradict the assumption that they have a carbide nature. The total carbon content in the carbide precipitates in terms of volume concentration is considerably lower than the limit of carbon solubility in molybdenum at the temperature of the tests.

Since in none of the creep tests of molybdenum under tension in a vacuum did we detect second-phase precipitates in the bulk of the specimens, we can assume that this effect is due to saturation of the specimen with carbon as a result of the action of a glow discharge since the vapor phase contained products of the decomposition of heavy hydrocarbon molecules from diffused oil and greases.

As a result of a study of the surface structure (at a depth of up to 10 μm) of molybdenum after high-intensity ion bombardment from a glow discharge (1500°C for 1 h) [3] we established that when a mixture of He + H_2 (in contrast to pure hydrogen) is used as the plasma-forming medium pronounced gas (helium) swelling ($\Delta V/V \approx 5$-10%) develops in the layer of thickness ∿300 nm closest to the surface, the average diameter of the bubbles being 20-50 nm, and the density of dislocations associated with the bubbles increases sharply [to $\rho \approx (1\text{-}5)\cdot 10^9$ cm^{-2}]. In the bulk of these specimens, after ion bombardment from a hydrogen glow discharge as well as from a glow discharge in a mixture of He + H_2 or pure helium we detected numerous, very long screw dislocations with Burgers vectors **b** of the type $a/2\langle 111\rangle$ in the process of slip and interaction (Fig. 4). It was established that these dislocations are capable of slipping in intersecting {110} slip planes and interacting, thus forming irregular dislocation networks, especially in the layers closest to the surface.

Comparison of the data about creep in specimens in a plasma-forming medium of pure hydrogen and an He + H_2 mixture shows that the formation, in the last case, of a highly swelled surface layer with a high dislocation density is not the main reason why these specimens have a higher creep resistance than do those tested in a vacuum.

As is known, in the stage of steady-state creep during ordinary tensile testing the structure of a single-crystal molybdenum specimen has a block structure, as was observed in the experiments conducted. In some respects similar changes in the structure also arise when the specimen is subjected to intense high-temperature bombardment with low-energy ions without a mechanical load. Indeed, bombardment of molybdenum single crystals in a glow discharge, as already indicated, leads to the generation of screw dislocations which most likely are formed in the surface layer and penetrate into the bulk by means of slip. In the process the dislocations actively interact with each other and with impurities, as a result of which after 3-5 h of bombardment (ion fluence $\sim 10^{22}$ cm^{-2}) a columnar large-block structure is formed with the axes of the blocks oriented perpendicular to the bombarded surface [2]. The generation of dislocations under such bombardment is probably caused by shear stresses due to the high degree of supersaturation of the lattice in the surface layer of the metal with atoms of the implanted gas [3]. From this we can conclude that the overall stressed state of a specimen tested for creep under bombardment is the superposition of the uniform field of stresses (in the cross section of the specimen) produced by an applied external field and the nonuniform field of stresses generated by atoms of the implanted gas. The interaction of dislocations generated by the action of these fields probably plays a certain role in changing the creep characteristics of such specimens in comparison with specimens tested in a vacuum.

At the same time, the results of the experiments indicate one more, much more significant, cause of the observed change in these characteristics. We should consider that this cause is the process of formation of finely dispersed precipitates of the carbide phase on elements of the dislocation structure, including block-boundary dislocations. Indeed, the low solubility of carbon in metals of subgroup VIA creates favorable conditions for its segregation on structural imperfections [8], and this, in turn, is capable of causing considerable hardening of these metals up to a temperature above $0.5T_m$, which has been demonstrated,

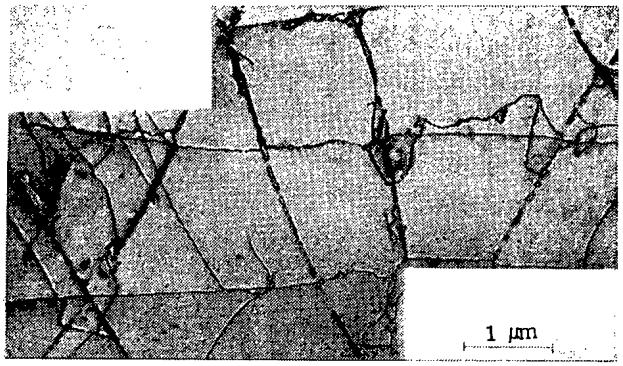

Fig. 3

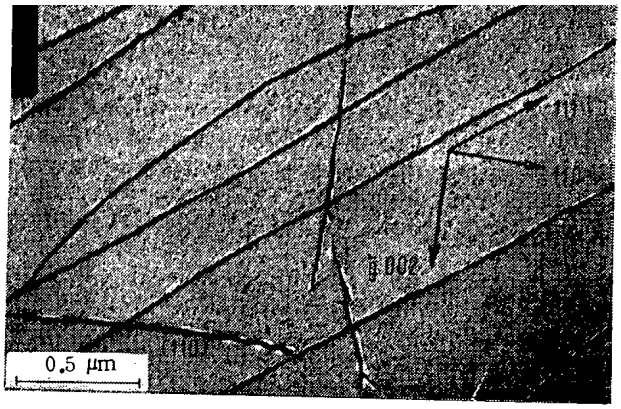

Fig. 4

Fig. 3. Fragment of a dislocation wall in a single-crystal molybdenum rod of diameter 4 mm, bombarded for 28 h with ions from a glow discharge in hydrogen at 1500°C.

Fig. 4. Dislocation structure in a single-crystal molybdenum disk bombarded with ions from a glow discharge in hydrogen, at a depth of 3.3 μm from the bombarded surface (the plane of the surface is (110); T = 1500°C, τ = 1 h).

e.g., on tungsten [9]. As was shown in [10], in the stage of steady-state creep deformation is effected by the motion of dislocations from the block boundaries through the blocks, the rate of this process being determined by the climbing of the dislocations over barriers in the block boundaries. The formation of microprecipitates of the new phase on elements of the dislocation structure of the boundaries clearly should substantially retard the climbing over these barriers and this is the main cause of the increase in the creep resistance. The presence of a large number of dislocation loops near the block boundaries in this case is treated as the result of the interaction of dislocations with phase precipitates and other dislocations. The proposed explanation is also supported by the fact that an increase in creep resistance was observed [2] only in those specimens whose bombardment had begun no less than 0.5-1.5 h (ion fluence $\sim 2 \cdot 10^{21}$ cm^{-2}) before the application of the load. Indeed, diffusion estimates show that after carbonization for 1 h at 1600°C the average carbon concentration in the bulk of a cylindrical molybdenum specimen of diameter 4 mm is no less than 20% of its maximum concentration in the thin surface layer. It must be pointed out, however, that high-temperature ion bombardment can cause both carbonization and decarbonization of a metal [11], depending on the quasistationary concentration of carbon in the thin surface layer, which is determined by the conditions and parameters of the bombardment [12].

Thus, the most probable cause of the hardening of single-crystal molybdenum during creep tests under ion bombardment is the formation of finely dispersed carbon precipitates on elements of the dislocation structure, primarily on dislocations of the block boundaries. These precipitates retard the mobility of the dislocations and decrease the creep rate. Since carbon atoms enter into the bulk of the metal by means of diffusion from the ion-bombardment surface, the hardening under consideration differs from that observed earlier, e.g., in steel because of the blocking of dislocations by carbide precipitates formed as a result of aging [13]. In accordance with the data obtained in this work and also taking into account the conclusions of [2], we can conclude that intensive high-temperature bombardment with low-energy light ions in the plasma of a glow discharge can be considered as an effective means of enhancing the strength characteristics of single-crystal molybdenum over a wide range of temperatures. There are reasons to believe that this conclusion will be valid for all metals of subgroup VIA.

LITERATURE CITED

1. A. A. Babad-Zakhryapin and M. I. Lagutkin, Metalloved. Term. Obrab. Met., No. 7, 70 (1976).
2. A. A. Babad-Zakhryapin, I. B. Savvatimova, P. V. Zubarev, and N. G. Tachkova, Fiz. Khim. Obrab. Mater., No. 6, 155 (1981).
3. V. N. Chernikov and A. P. Zakharov, Poverkhnost'. Fiz., Khim., Mekh., No. 2, 79 (1984).
4. V. I. Chernikov, in: Eleventh All-Union Conference on Electron Microscopy [in Russian], Vol. 1, Nauka, Moscow (1979), p. 175.

5. Zakopane (Poland), Eindhoven (1979), p. 20.
6. J. Friedel, Dislocations, Addison-Wesley, Reading, Mass. (1964).
7. F. Montheillet, J. Haudin, and G. Frade, Phys. Status Solidi (a), 17, 593 (1973).
8. V. I. Trefilov, Yu. V. Mil'man, and S. A. Firstov, Physical Foundations of the Strength of Refractory Metals [in Russian], Naukova Dumka, Kiev (1975), p. 26.
9. R. Schitzel, Trans. Am. Soc. Met., 58, 687 (1965).
10. V. G. Glebovskii, Ch. V. Kopetskii, M. M. Myshlyaev, and Yu. A. Romanov. Fiz. Met. Metalloved., 41, No. 3, 621 (1976).
11. A. A. Babad-Zakhryapin and G. D. Kuznetsov, Chemical-Heat Treatment in a Glow Discharge [in Russian], Atomizdat, Moscow (1975), p. 175.
12. V. N. Chernikov, "Structural and phase changes in molybdenum under low-energy bombardment with hydrogen and deuterium ions," Candidate's Dissertation, Institute of Metal Physics, Academy of Sciences of the Ukrainian SSR, Kiev (1980).
13. S. Keown, in: Electron Microscopy, 1968, Vol. 1, Tipografia Poliglotta Vaticana, Rome (1968), p. 497.

STUDY OF THE DIFFUSION OF HYDROGEN IN MATERIALS BY THE METHOD OF ELASTIC SCATTERING OF FAST NEUTRONS

A. N. Valiev, V. N. Kadushkin, Z. P. Kiseleva, V. N. Serebryakov, B. G. Skorodumov, A. P. Sokolov, V. A. Shpiner, P. K. Khabibullaev, and I. O. Yatsevich

UDC 533.15:532.546:539.171.016

Interest in the behavior of hydrogen in different materials has increased especially in connection with problems of nuclear, thermonuclear, and hydrogen power. Nondestructive methods, based on the interaction of accelerated ions with dissolved hydrogen [1], have been used in recent years to study the diffusion of hydrogen in materials.

In this paper we examine a method for studying the concentration profile and, based on it, the diffusion of hydrogen in materials with the use of elastic scattering of fast neutrons by hydrogen isotopes. In this case, the calculation of the concentration profile simplifies and the possibilities for performing experiments increase in connection with the higher penetrability of neutrons and the absence of any need for placing the sample into the vacuum system of the accelerator; it is possible to study the diffusion of any isotope or mixture of isotopes of hydrogen; there is practically no limit on the total thickness of the samples; the range of measured coefficients of diffusion is extended; and, finally, the particles under study do not affect the process of hydrogen diffusion as a result of heating of the material and formation of defects.

The experimental setup (Fig. 1) consists of a source of 14.5-MeV neutrons (neutron generator), a vacuum chamber with a diffusion cell, a telescope of detectors, a gas-vacuum stand, and electronic apparatus with a two-dimensional pulse-height analyzer.

The vacuum chamber contains three silicon detectors 1, which together with the disphragms 2 form the telescope 3. The target disk 4, aside from a diffusion cell 5, containing a membrane 6 consisting of the material studied, also contains a target for alignment, energy calibration, and providing a reference for the measurements. The targets are changed and fixed in the working position through the vacuum input 7 with the help of a power unit and terminal switches 8. The chamber cover 9 contains connectors 10, which, with the help of flexible hoses 11, connect the injection chamber 12 and the collection chamber 13 of the diffusion cell with the gas-vacuum stand.

The chamber is evacuated through an outlet 14. Signals from the detectors are fed into the electronics system through the vacuum inputs on the cover 15. The housing of the diffusion cell is surrounded by the electrical heater 16 and is thermally insulated by a Teflon holder 17. The temperature of the membrane is measured with a Chromel–Alumel thermocouple. The injection chamber of the cell has two channels for pumping gas. The collection chamber

Translated from Atomnaya Énergiya, Vol. 58, No. 1, pp. 27-32, January, 1985. Original article submitted December 23, 1984.

 0038-531X/85/5801-0032$09.50

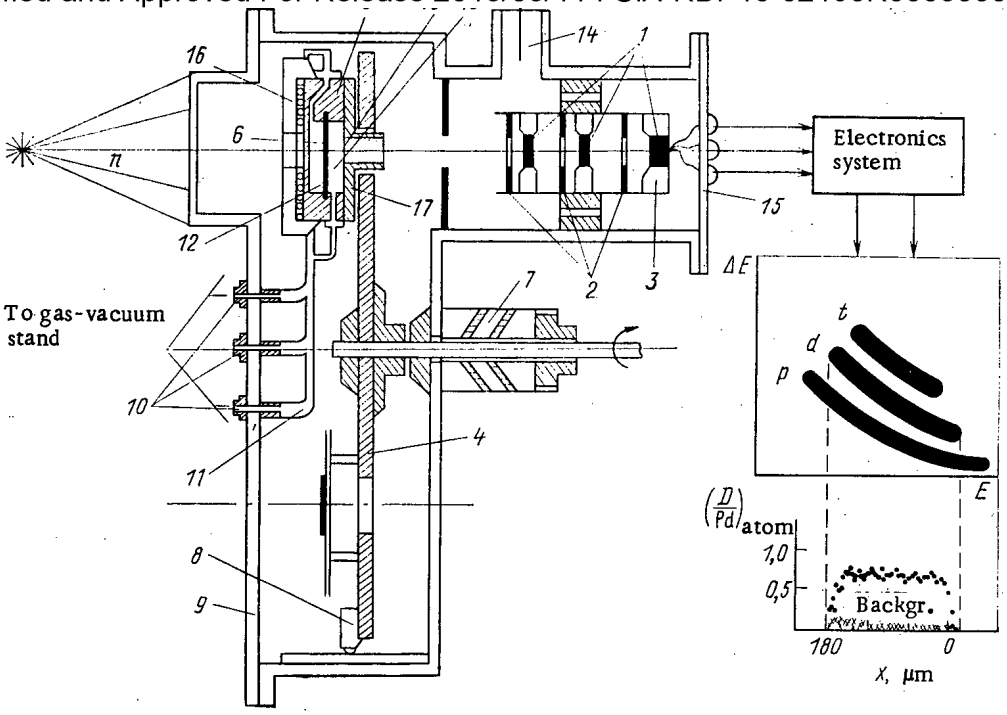

Fig. 1. Diagram of the experimental setup.

is separated from the vacuum chamber by a 7-μm-thick Lavsan window 18 for outflow of the products of nuclear reactions in the direction of the telescope.

The purpose of the gas-vacuum stand is to evacuate and fill the diffusion cell with any gaseous isotope of hydrogen or its mixture with other gases, as well as to measure the gas flow through the membrane. Liquid mixtures can be injected into the injection chamber.

The vacuum chamber, preamplifiers of the signals from the detectors, and the gas-vacuum stand are mounted on a special table, positioned in front of the neutron source. The control panel is located in a separate location, where information enters from detectors and also from pressure and temperature sensors.

When any target placed between the neutron source and the telescope is irradiated, the particles — reaction products — are recorded by the detectors with the help of the electronic apparatus, which includes a two-dimensional pulse-height analyzer and enables the identification of the type of particles and the determination of its energy [2, 3]. The particle loses part of its energy ΔE in the first two detectors and all of the remaining energy E_{rem} in the third detector. Information is accumulated in the analyzer, fed into the computer, and plotted on a graphical display in the form of a spectrum in the plane with coordinates ΔE and $E = \Delta E + E_{rem}$. Since $\Delta E \times E \approx$ const, in this two-dimensional field the events fall on hyperbolas, corresponding to protons (p), deuterons (d), and tritons (t). The hyperbolas are "traced" and projected on the total-energy axis, forming the energy spectra for each hydrogen isotope.

Figure 2 shows a photograph of the graphical display after accumulation of information with irradiation of a reference sample — a complex target consisting of five films of deuteropolyethylene (∿2 mg/cm²), interlaid with four aluminum films (90 μm). The channels of the analyzer, proportional to E, are plotted along the horizontal axis. In the two-dimensional spectrum, channels proportional to ΔE are plotted along the vertical axis at the bottom, and the number of counts in the spectrum-projection channel are plotted at the top. The points in the two-dimensional spectrum reflect the program of drawing the deuteron hyperbola.

The thickness of the first two detectors of the telescope (100 μm each) determines energy threshold of detection, corresponding to the energy of the given type of particles, whose range is equal to the total thickness of the detectors. The thickness of the detectors is chosen taking into account the fact that when the thickness is increased, the identification of the particles is improved, but the depth of the analysis simultaneously decreases. The thickness of the third detector (500 μm) corresponds to the range of deuterons with maximum

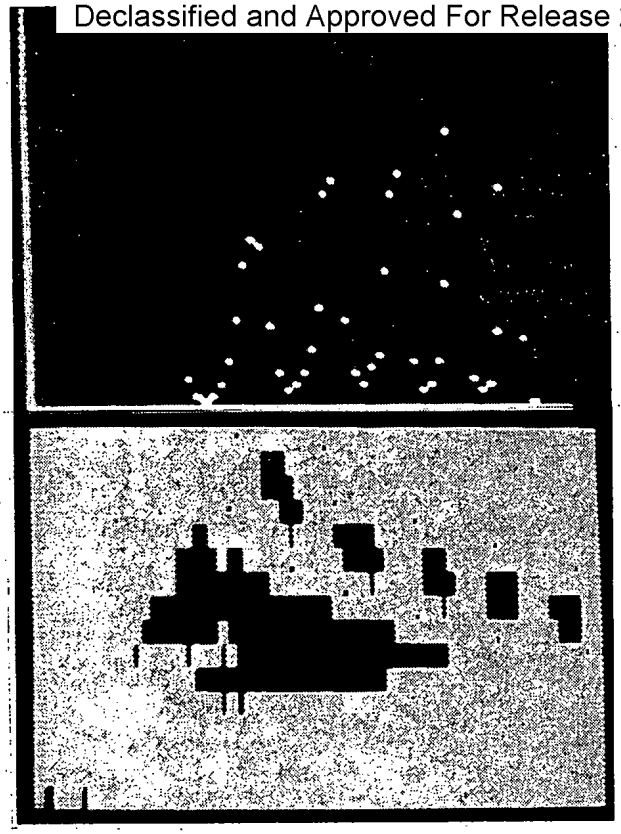

Fig. 2. Photography of the screen of a graphical display displaying the spectrum of a complex target. The two-dimensional spectrum is shown at the bottom and the projection of the deuteron locus on the energy axis is shown at the top.

possible energy of 12.9 MeV and the flight path of protons with energy not exceeding 10 MeV. For this reason, the proton hyperbola has a "turned up" form, which improves the discrimination of the deuteron spectrum. We note that an increase in the thickness of the detectors increases the intensity of the entering phonon pulses, due to the reactions of neutrons with the silicon.

It is evident from Fig. 2 that the energy spectrum of recoil deuterons contains information on the distribution of the concentration of the given hydrogen isotope in the sample. Indeed, at any depth of the sample the neutrons are scattered elastically by the nucleus of the hydrogen isotope with mass m with the same energy E_n, forming recoil particles with energy

$$E_0 = \frac{4m}{(m+1)^2} E_n \cos^2\theta, \tag{1}$$

where $\theta = \theta_1 + \theta_2$ can differ from zero due to the finite angular aperture of the systems neutron-source–sample (θ_1) and sample–detector (θ_2).

Under the conditions of the experiment the maximum values were equal to $\theta_1 = 6°$ and $\theta_2 = 8°$, which leads to the appearance of an energy spread ΔE due to the spread over angles $\Delta\theta$

$$\Delta E/E_0 = 2\,\mathrm{tg}\,\bar{\theta}\Delta\theta, \tag{2}$$

where $\bar{\theta} = 6°$ is the average value of the scattering angle at the maximum of the angular resolution function of the setup, while $\Delta\theta = 7°$ is the half-width of this function [4].

After passing through a thickness x of the material, the particle reaches the telescope with an energy E, which is related to the depth at which the hydrogen is located in the sample by the relation

$$x/\cos\theta_2 = R(E_0) - R(E) = \int_E^{E_0} dE/S(E) \approx \frac{E_0 - E}{\bar{S}}, \tag{3}$$

where R(E) and S(E) = dE/dx(E) are the range and the stopping power of the sample material for particles with energy E; $\bar{S}$ is the stopping power averaged over the interval from E_0 to E. It is useful to insert the stopping power into expression (3) when analyzing thick samples, and the range when analyzing thick samples. Since $\cos\theta_2 = 1$ to within less than 1%, the expression (3) can be additionally simplified.

Fig. 3. Photograph of the two-dimensional spectrum obtained with the interaction of neutrons with a lithium target; p, d, and t are the localization of protons, deuterons, and tritons, respectively.

The number of events in channel k of the spectrum-projection constitutes

$$dN/dk = J\,(d\sigma/d\omega)\,C\,(x)\,dx\Delta\omega, \tag{4}$$

where J is the number of neutrons hitting the sample; $d\sigma/d\omega$ is the differential elastic-scattering cross section of neutrons scattered by the given hydrogen isotope; C(x) is the concentration of hydrogen in the layer dx at a depth x of the sample, related to the energy of the detected particle $E = \gamma k$ by expression (3); $\gamma = dE/dk$ is the energy value of the spectrometer channel; and $\Delta\omega$ is its solid angle. Applying Eq. (4) when analyzing the sample and the reference, we obtain the relations for finding from the measured instrumental spectrum either the concentration profile of the isotope

$$C\,(x) = \frac{J_r n_r}{N_r J n_M}\,\frac{dN}{dk}\,\frac{dk}{dE}\,\frac{dE}{dx}, \tag{5}$$

or the total content of this isotope

$$C = NJ_t\,n_r/N_r J n_M l. \tag{6}$$

Here N and N_r are the total number of counts in the spectrum for measurements of the sample studied and of the reference, respectively; n_e is the number of hydrogen atoms per cubic centimeter of the reference, multiplied by the thickness of the reference; $n_M l$ is the number of atoms of the material per cubic centimeter of sample volume, multiplied by the thickness of the sample. The concentration is measured as the ratio of the number of hydrogen atoms to the number of metal atoms $(H/M)_{at}$.

The selectivity of the spectrometer relative to the particle type is illustrated by the photograph (Fig. 3) of the two-dimensional spectrum of the products of interaction of neutrons with the target from a mixture of lithium isotopes based on the reactions (n, p), (n, d), and (n, t). It is evident that all three hyperbolas are well separated.

The limit of detection of a given hydrogen isotope is determined by the intensity of the background pulses, which, based on relation (5), can be rescaled to the equivalent hydrogen concentration. The main source of the background is the nuclear reactions with the formation of charged particles in the membrane material and the material of the first detector. The cross section of these reactions is 10-100 times lower than the elastic-scattering cross section of hydrogen.

The reactions (n, d) and (n, t) have a lower yield than the reaction (n, p) and, in addition, their energy threshold exceeds 5 MeV, which shifts the background in analyzing deuterium and tritium into the low-energy range, i.e., large depth. The background level for diffusion of deuterium in paladium is shown in Fig. 1 together with the distribution of the deuterium concentration over the thickness of the membrane. The background is minimum [$<10^{-3}\cdot (D/M)_{at}$] for a small depth of analysis, but increases up to $0.05(D/M)_{at}$ as the depth increases. The background is somewhat lower for tritium than for deuterium, and for hydrogen it is somewhat higher [$\sim 0.1(H/M)_{at}$] and uniform over the depth. The proton background can be decreased by replacing the first silicon detector by a gaseous proportional counter filled with CO [2].

The maximum depth of the analyzed region of the sample, in accordance with expression (3), is equal to

$$x_{max} = R\,(E_0) - R\,(E_{thr}), \tag{7}$$

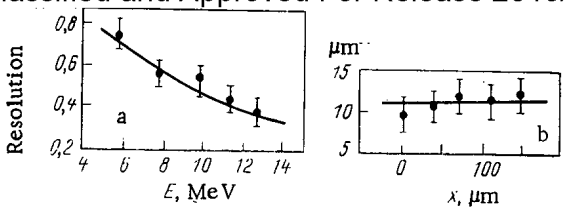

Fig. 4. Dependence of the resolution on the energy (a) and on the depth (b).

where E_{thr} is the energy threshold of the spectrometer. If the total thickness of the first two detectors is equal to 150 μm, and the energy threshold in the E channel is equal to 0.5 MeV, then the maximum depth of analysis of deuterium in palladium is equal to 150 μm, and 430 μm in aluminum. The total sample thickness, due to the large penetrability of fast neutrons, is practically unlimited.

By differentiating expression (3) we obtain the equality

$$dx = -dE/S(E), \tag{8}$$

from which it follows that the depth resolution depends on the stopping power of the sample material and with a given energy resolution improves as the depth is increased. The energy resolution of the spectrometer is determined by the characteristic resolution of the detectors, the nonmonochromaticity of the neutron source, and primarily by the energy spread due to the geometry in accordance with expression (2).

It is evident in the reference spectrum in Fig. 2 that as the recoil-deuteron energy decreases, the distance between the peaks increases in accordance with expression (8), but the width of the peak also increases due to fluctuations in the energy losses and multiple scattering. The dependence of the half-width of the peaks on the energy obtained for palladium (Fig. 4a) and the dependence of this half-width on the depth (Fig. 4b) rescaled based on expression (8) indicate that the resolution is virtually independent of the depth.

We shall examine as an example the sorption of deuterium by a palladium membrane 80 μm thick at room temperature and under a pressure of 10^5 Pa and the subsequent desorption of deuterium into a vacuum. To accelerate the surface processes, we covered both sides of the membrane with palladium black. We switched on the spectrometer simultaneously with the injection of deuterium into the diffusion cell on both sides of the membrane and we measured the concentration profile of deuterium over the membrane thickness at definite time intervals.

The results are presented in Fig. 5. The average (taking into account the exposure time) time from the moment that the deuterium is injected into the diffusion cell or from the beginning of evacuation is indicated on each profile. The kinetics of the change in the total content of the deuterium in the membrane is presented at the bottom of the figure.

The solution of the nonstationary Fick equation for the sorption process under the condition of instantaneous establishment of the equilibrium concentration of deuterium C_0 on the surfaces of the membrane, taking into account the time of analysis τ, leads to the expression

$$C(x) = C_0\left\{1+\frac{2}{\pi D\tau}\sum_1^n\left(\frac{l}{\pi n}\right)^2\left(\exp\left[-t\left(\frac{\pi n}{l}\right)^2 D\right]-\exp\left[-(\tau+t)\left(\frac{\pi n}{l}\right)^2 D\right)\sin\frac{\pi n x}{l}\,\frac{\cos(\pi+n)-1}{n}\right\}. \tag{9}$$

Due to the finite resolution of the spectrometer, the instrumental profile of the concentration C(x), obtained by rescaling the energy spectrum with the help of expression (5), is related to the true distribution of hydrogen over the depth of the material $C_{true}(x)$ by the expression

$$C(x)\int_0^l C_{true}(x')\,f(x,\,x')\,dx', \tag{10}$$

where f is the resolution function, which can be approximated by a Gaussian function with a half-width obtained by averaging the data in Fig. 4b.

The continuous lines drawn on the sorption profiles (see Fig. 5) were obtained by transforming the computed distributions (9) using formula (10) and then fitting to the experimental distributions by the method of least squares with respect to the parameter D. The following values of the diffusion coefficient were obtained for the first three sorption profiles: $0.5\cdot10^{-8}$, $1.15\cdot10^{-8}$, and $2.15\cdot10^{-8}$ cm²/sec, respectively, which is much lower than the published values for the α phase ($4\cdot10^{-7}$ cm²/sec) and for the β phase ($2\cdot10^{-6}$ cm²/sec) of palladium

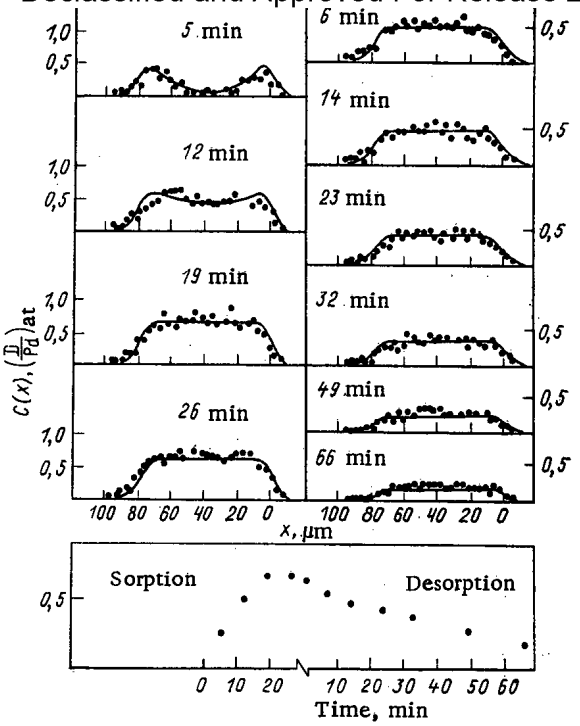

Fig. 5. Change in the profiles of the deuterium concentration in palladium during the sorption and desorption processes.

deuteride [5, 6]. The desorption of deuterium is much slower than sorption. The concentration profiles are practically uniform. The solid lines show the result of the transformation of a rectangular distribution with the help of expression (10).

This behavior of the concentration profiles apparently indicates the following:

sorption of deuterium cannot be described by Fick's equation with a constant coefficient of diffusion, especially since α—β transformation occurs;

desorption is limited by the rate of the surface reactions and, possibly, by the reverse β—α transformation also.

The proposed technique permits studying the diffusion of hydrogen isotopes in membranes from any solid materials. The accuracy of the measured parameters is determined by the statistical errors, which depend on the solubility of hydrogen in the studied material (hydrogen-rich materials are preferable) as well as on the degree of stationariness of the state studied. An important feature of the method is the possibility of measuring simultaneously the dynamics of the concentration profiles and the hydrogen flow through the membrane.

The authors thank their colleagues at the Institute of Electronics of the Academy of Sciences of the Uzbek SSR T. D. Radzhabov and L. A. Vaiman for preparing the activated palladium membranes.

LITERATURE CITED

1. B. G. Skorodumov, Problems in Atomic Science and Technology. Series on Nuclear-Hydrogen Power and Technology, No. 2(15), 22 (1983).
2. L. Kuo, M. Petravic, and B. Turko, Nucl. Instrum. Methods, 10, 53 (1961).
3. K. P. Artemov et al., Yad. Fiz., 12, 1180 (1970).
4. V. K. Voitovetskii, I. L. Korsunskii, and Yu. F. Pazhin, Prib. Tekh. Eksp., No. 2, 54 (1965).
5. F. Lewis, The Palladium Hydrogen System, Academic Press, New York (1967).
6. Hydrogen in Metals [Russian translation], Mir, Moscow (1981).

POSSIBILITIES OF REDUCING RADIATION EROSION BY THE USE OF PROTECTIVE COATINGS

B. A. Kalin, I. I. Chernov, D. M. Skorov,
P. I. Kartsev, and E. P. Fomina

UDC 621.039.531

At the present time, one of the most promising structural materials for thermonuclear reactors is considered to be austenitic stainless steels and alloys [1], which have quite high physicomechanical properties and a satisfactory radiation resistance in neutron fields [2, 3]. However, the erosion resistance of these materials during bombardment with helium ions is low, and the coefficient of erosion can attain ∿1 atom/ion [4]. This leads to contamination of the plasma with impurities with a high atomic number Z, which diffuse towards the center of the plasma cord [5], lowering the fuel concentration and impairing the energy balance of the particles in the plasma.

One of the effective routes for reducing the concentration of heavy impurities in the plasma is the use of protective coatings with a low Z and a low coefficient of erosion [6-8]. Wilson et al. [7] proposed to protect the wall from plasma radiation by sputtering aluminum on the material of the discharge chamber, and they investigated the radiation resistance of the coatings obtained during irradiation with helium ions of energy 20 and 300 keV. In [9], the outlook was mentioned for aluminized steels and alloys as materials for thermonuclear reactors. The purpose of the present paper is to investigate the erosion resistance of austenitic steels and nickel alloys with coatings of aluminum with a different thickness and silicon and also with coatings produced by aluminizing in lithium, during irradiation with He^+ ions.

Deposition of silicon and aluminum on the surface of electropolished samples was conducted by thermal vaporization in vacuo at not above 10^{-3} Pa; the coatings were deposited on one half of the sample and the other half (control) was shielded. A layer of silicon with a thickness of 20 nm was deposited on samples of steel 16-15; samples of steel 18-10 were investigated with aluminum coatings of variable thickness 80, 160, and 320 nm, which corresponds approximately to $R_p/2$, R_p and $2R_p$ (R_p is the projective range of He^+ ions with energy 20 keV in aluminum). Aluminization of steel 18-10 and nickel alloy 20-45 was carried out in a bath (10% Al + 90% Li) during 5 h at a temperature of 870 and 970°K.

The samples were irradiated with He^+ ions with energy 20 keV in a mass monochromator [10] and with energy 40 keV in the ILU-3 accelerator [11]. For identical irradiation conditions of the samples during bombardment with 20 keV ions, the center of the beam coincided with the boundary between the shielded and unshielded surfaces; for irradiation with 40 keV ions, a cassette method was used: eight samples were placed in a metal cassette which was ir-

TABLE 1. Materials Investigated, Phase Composition, Microhardness of the Coatings, and Irradiation Conditions with He^+ Ions

Backing material	Method of deposition of coating	Phase composition of coating	Thickness of coating, nm	Microhardness, MPa	Irradiation conditions		
					E, keV	$D \cdot 10^{-22}$ m^{-2}	T, K
Steel 16-15	Thermal vaporization in vacuo	Si	20	—	20	1—7,5	< 370
					40	1	570
Steel 18-10	Thermal vaporization in vacuo	Al	80	—	20	0,5; 1	300; 470
			160	—	20	0,5; 1	300; 470
			320	—	20	0,5; 1	300; 470
Steel 18-10	A-1*	$FeAl$, $FeAl_3$, $NiAl$, $AlCr_2$	10^4	$4{,}4 \cdot 10^3$	40	0,5—4	300—770
	A-2	$FeAl$, $NiAl$, $AlCr_2$, $FeAl_3$, Li_2O	$7 \cdot 10^3$	$3{,}5 \cdot 10^3$	40	1; 2	300—570
Steel 20-45	A-1	$FeAl$, $NiAl$, Fe_3Al, α-Fe, Ni, Fe_2Al_5	$1{,}5 \cdot 10^4$	$5{,}0 \cdot 10^3$	40	1	470—570

*A-2, A-1) Aluminized in a bath of 10% Al + 90% Li during 5 h at 970 and 870°K, respectively.

Translated from Atomnaya Énergiya, Vol. 58, No. 1, pp. 32-38, January, 1985. Original article submitted February 23, 1984.

 0038-531X/85/5801-0038$09.50

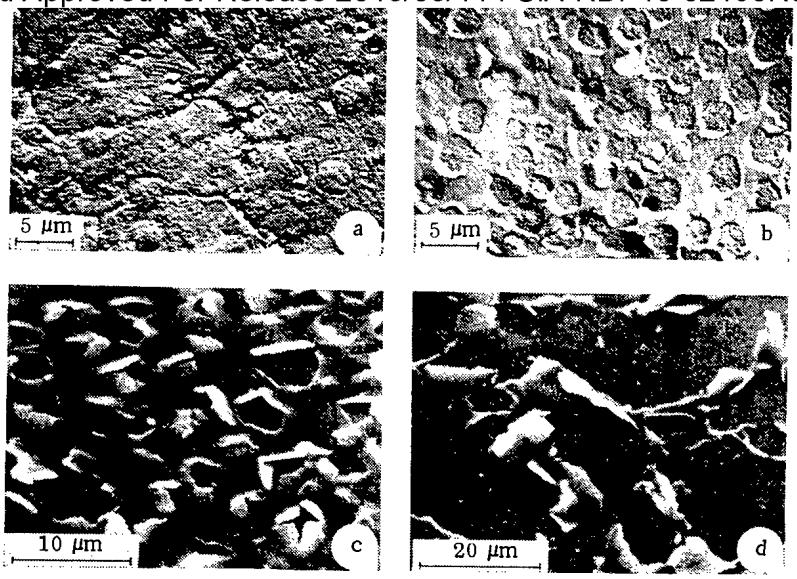

Fig. 1. Photomicrographs of the surface of samples of steel 16-15 irradiated with He^+: a, b) E = 20 keV, D = $7.5 \cdot 10^{22}$ m^{-2}, T = 300°K; c, d) E = 40 keV, D = $1 \cdot 10^{22}$ m^{-2}, T = 570°K; a, c) samples with a silicon coating of thickness 20 nm; b, d) control samples.

radiated with a beam of He^+, sweeping over the hirozontal. The materials investigated and their irradiation conditions are shown in Table 1. The surface of the irradiated samples was studied in the REM-200 scanning electron microscope and by the method of single-step angular replicas in the EMV-100L electron microscope.

The qualitative and quantitative phase composition of the aluminized layer was investigated on the URS-50IM diffractometer and the MAP-1 microanalyzer at a depth of ∿1 μm.

Silicon Coatings. It can be seen in Fig. 1a that by irradiation with He^+ ions of energy 20 keV, blistering in the samples of steel 16-15 with a coating of silicon of thickness 20 nm is significantly suppressed, and right up to an ion dose of $7.5 \cdot 10^{22}$ m^{-2} erosion is insignificant. Irradiation in similar conditions of the control samples (without coatings) produces considerable erosion due to blistering (Fig. 1b). An increase of the ion energy up to 40 keV leads to the formation of blisters and surface erosion of the steel with the coating (Fig. 1c). However, the sizes of the blisters and of the peeled sections of the surface on samples with a coating are significantly less (Fig. 1c and d). The thickness of the blister caps (or detached layer), determined both by the scanning electron microscope and by the method of high-resolution angular replicas (Fig. 2), on coated samples is greater than on the control samples and is equal to 305 ± 175 and 275 ± 90 nm, respectively. The erosion coefficients on these samples are 0.25 and 0.84 atom/ion, respectively. Deposition of the coating also changes the nature of the surface damage: if peeling occurs predominantly over the periphery of the cupola (see Fig. 1d) on the control samples, i.e., as for brittle materials, then the blisters on the samples with coating, as a rule, are collapsed over the top of the cupola (see Fig. 1c), i.e., like plastic materials.

Thus, the radiation erosion caused by blistering can be reduced significantly or suppressed by the deposition of thin silicon coatings (for example, renewable in the course of operation of the reactor). At the same time, the degree of reduction of erosion depends on the ratio of the coating thickness h and the projective range of the He^+ ions in the material, R_p; with increase of the ratio h/R_p, blistering is reduced markedly. Therefore, an investigation of blister formation and erosion of materials with coatings of different thickness is of considerable interest.

Aluminum Coatings. The deposition of aluminum coatings considerably changes the nature of blister formation and the degree of surface erosion (Table 2): the presence of coatings significantly reduces the surface erosion by blistering; with increase of thickness of the aluminum film the erosion resistance of steel increases.

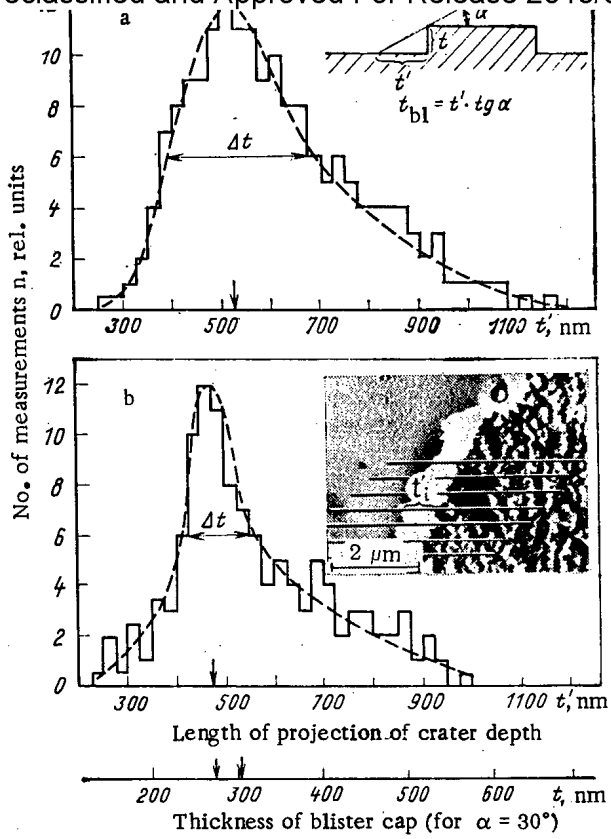

Fig. 2. Thickness of blister caps (depth of craters on the detached sections of the surface) on samples with silicon (a) coating and without coating (b), irradiated with He^+ ions with E = 40 keV, D = $1 \cdot 10^{22}$ m^{-2}, T = 570°K.

TABLE 2. Effect of Thickness of Aluminum Coatings on the Blistering Parameters* of Steel 18-10 during Bombardment with He^+ with Energy 20 keV

Item No.	Irradiaton cond.		Samples with coating					Control samples			
	T, K	$D \cdot 10^{-22}$, m^{-2}	h, nm	d_{max}, μm	$\bar{d}$, μm	$\rho \cdot 10^{-12}$, m^{-2}	S, atom/ion	d_{max}, μm	$\bar{d}$, μm	$\rho \cdot 10^{-12}$, m^{-2}	S, atom/ion
1	300	0,5	80	1,4	0,35	1,54	~0	2,4	1,35	0,38	0,08±0,02
2	300	1	80	5,2	0,45	1,42	0,02±0,01	2,4	1,35	0,34	0,25±0,06
3	300	0,5	160	8,0	0,25	1,10	~0	—	—	—	—
4	300	1	160	9,0	0,25	1,10	~0	—	—	—	—
5	300	0,5	320	10,0	0,25	2,70	~0	—	—	—	—
6	300	1	320	12,0	0,25	2,20	~0	—	—	—	—
7	470	0,5	80	1,2	0,45	1,91	<0,01	4,0	1,35	0,36	0,48±0,12
8	470	1	80	2,8	0,35	1,54	0,10±0,03	3,6	1,35	0,38	0,57±0,14
9	470	0,5	160	4,0	0,90	0,70	~0	—	—	—	—
10	470	1	160	6,0	0,70	0,42	0,01±0,005	—	—	—	—
11	470	0,5	320	2,8	0,25	0,20	~0	—	—	—	—
12	470	1	320	2,8	0,25	1,90	~0	—	—	—	—

*d_{max}, $\bar{d}$) The maximum and average sizes of the blisters; ρ) the density of the blisters; S) the coefficient of erosion occurring in consequence of surface peeling. When calculating the density of the blisters, only blisters with d > 0.2 μm were taken into account; in samples 5 and 6, the density of the fine blisters (d ≤ 0.2 μm) exceeds the density of the coarse blisters (d > 0.2 μm) by a factor of 100.

At T = 300°K (Tables 2 and 3), the density of the blisters on the samples with coatings is significantly higher and their average sizes are lower than on the control samples. However, together with the fine and medium blisters, individual very coarse blisters are encountered on these samples, the sizes of which attain 5-10 μm. An increase of the coating thickness leads to an increase of d_{max} of the blisters from 1-5 μm for h = 80 nm to 10-12 μm for h = 320 nm. At the same time, an increase of the fraction of the finest blisters (d < 0.5 μm) on the surface of the samples is characteristic with increase of the coating thickness, which are formed even on the cupolas of coarse blisters of several micrometers (see Fig. 3b). This leads to two maxima in the distribution of the blisters by sizes. A similar distribution of the blisters was observed earlier in the case of molybdenum and complexly alloyed nickel alloy irradiated with 20 keV He^+ ions [4, 12].

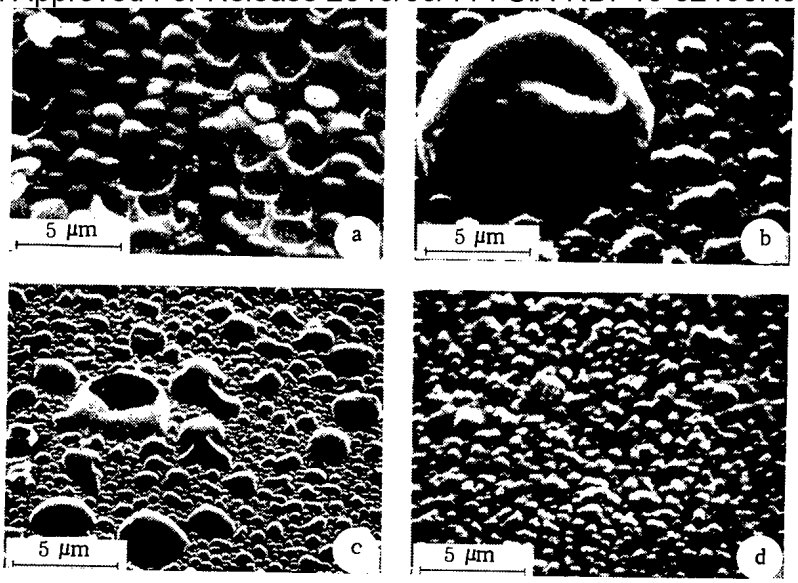

Fig. 3. Blistering of steel 18-10 without coating (a) and with aluminum coatings of thickness 160 (c) and 320 nm (b, d) as a result of irradiation by He^+ ions with energy 20 keV at T = 300°K (a, b) and 470°K (c, d) up to a dose of $5 \cdot 10^{21}$ (a) and $1 \cdot 10^{22}$ m^{-1} (b, d).

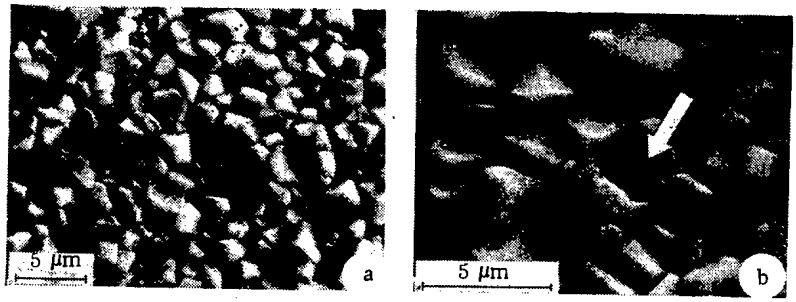

Fig. 4. Surface topography of aluminized alloy 20-45 (conditions 970°K, 5 h): a) before irradiation; b) after irradiation with He^+ at E = 40 keV, D = $1 \cdot 10^{22}$ m^{-2}, T = 470°K (the peeled sections are indicated by the arrow).

With increase of the irradiation temperature to 470°K, the erosion coefficients of the control samples and of the samples with coatings increase (see Table 2), but the erosion of the latter nevertheless is considerably lower. At 470°K, the nature of the erosion of samples with a coating of thickness 80 nm is similar to the nature of the surface damage of the control samples, i.e., peeling of the surface takes place by means of peripheral rupture of the blister cupolas and their detachment. However, with increase of thickness of the coatings, erosion is reduced and suppressed (see Fig. 3c, d). At T = 470°K and h = 360 nm, the coarse blisters vanish (see Table 2 and Fig. 3d). Even the fine blisters ($d \leq 0.2$ μm) also disappear, and their distribution with respect to sizes has only one maximum.

Coatings Obtained by Aluminization. By aluminization in a melt of 10% Al + 90% Li, coatings are obtained for which the thickness attains several micrometers (see Table 1), i.e., significantly higher than the projective range of He^+ ions with energy 20 and 40 keV in metals. For all the coatings obtained by aluminization, a surface microrelief is characteristic (Fig. 4a), which has a cellular structure. At the same time, a reduction of the aluminization temperature from 970 to 870°K leads to a significant reduction of the cell sizes. As it can be seen from Table 3, at a higher aluminization temperature the surface layer is markedly depleted in chromium and titanium, but enriched in aluminum.

of the Coatings Obtained by Aluminization, mass %

Backing material	Conditions	Al	Fe	Ni	Cr	Ti	Rem.
18-10	A-1	21	53	12	7,5	0,1	6,4
18-10	A-2	11	50	20	13	4	2
20-45	A-1	28	10	55	1	—	6
20-45	A-1	4	30	40	3	—	23

ings Obtained by Aluminization, Irradiated with He^+ Ions with Energy 40 keV

Material	Irradiation conditions		Samples with coating		Control samples
	T, K	$D \cdot 10^{-22}$, m^{-2}	regime	S, atom/ion	
Steel 18-10	300	0,5	A-1	~0	—
	300	0,8		~0	—
	300	2		0,04±0,01	0,19±0,05
	470	2		0,04±0,01	0,21±0,05
	470	4		0,02±0,01	—
	570	1		0,09±0,02	0,28±0,07
	770	1		0,13±0,03	0,05±0,01
	300	2	A-2	~0	0,19±0,05
	470	2		0,02±0,01	0,21±0,07
	570	1		0,05±0,01	0,28±0,07
Nickel steel 20-45	470	1	A-1	0,10±0,02	1,58±0,39
	570	1		0,26±0,06	1,14±0,28

The cellular structure of the coating obtained by aluminization on a nickel alloy of the type 20-45 has a more contoured topography by comparison with steels, which obviously is due to the higher rate of dissolution of nickel (the principal component of the alloy) in lithium and to the high diffusion mobility of the alloy components at 970°K.

The contouring of the cellular structure at a low (870°K) temperature for this reason is expressed more weakly. The higher rate of interaction of the nickel in comparison with steel is confirmed also by the greater thickness of the coating (see Table 1).

A qualitative phase analysis showed (see Table 1) that the coatings consist of a number of intermetallides. In steel 18-10 aluminized at 870°K, by the method of secondary ion emission, lithium oxide Li_2O is detected, which is absent at 970°K. In coatings on alloy 20-45 obtained at 970°K, phases of the intermetallide Fe_2Al_5 are detected. The complex intermetallide composition of aluminized alloy at a depth of 7-15 μm determines the microhardness of the coating, increasing with increase of thickness of the layer, which, in its turn, is proportional to the aluminization temperature (see Table 1).

The results of an electron-microscopic investigation of the surface of irradiated samples are given in Table 4, and typical photomicrographs of the surface are shown in Fig. 4. Radiation damage of the surface of the aluminized layers is effected by a peeling mechanism without visible swelling (Fig. 4b), which, evidently, is due to the complex structure of the coating and to the high bond energy of the intermetallide phase, causing large-scale damage. As it can be seen from Table 4, the coefficients of erosion of the aluminized materials increase with temperature right up to 770°K, while the erosion maximum of austenitic steels is found in the range 570-670°K. In this case, erosion of the aluminized alloy 20-45 is somewhat higher than the erosion of aluminized steel 18-10 during irradiation in identical conditions. A reduction of the cells of the surface microrelief (by a change of aluminizing conditions from A-1 to A-2) causes a reduction of the coefficients of erosion (see Table 4). A comparison of the coefficients of erosion of aluminized steel and alloy with the erosion of the original materials indicates a significant reduction (by a factor of 10-100) of erosion as a result of deposition of the coating (see Table 4, Fig. 4b, and Fig. 1d).

Discussion of Results. The data obtained confirm the considerable suppression of blister formation and erosion of the materials investigated, by the deposition on them of silicon and aluminum coatings by means of thermal vaporization, or of intermetallide coatings produced by aluminization. This effect is maintained for coatings in all ranges of thickness h investigated for both small and large values of R_p. With increase of h, the effect of erosion reduction is enhanced. If the reduction or suppression of blistering as a result of the deposition of the coatings by aluminization is explained by the formation of a rough cellular structure on the surface, which destroys the coplanarity of occurrence of the implanted helium [9], then the silicon and aluminum coatings used had an improved uni-

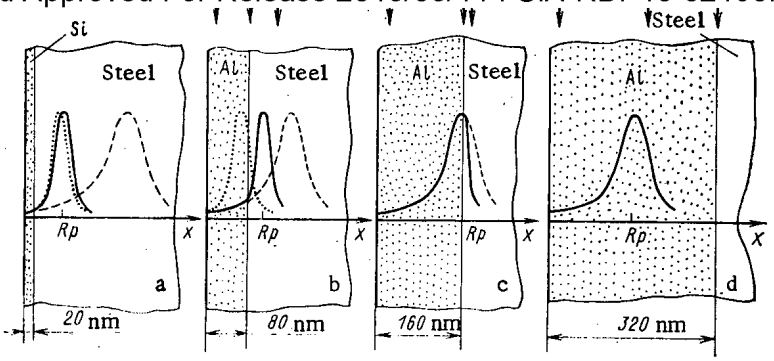

Fig. 5. Distribution of helium with energy 20 keV and probable sites of origin of blister cracks in steels with silicon (a) and aluminum coatings (b-d): ---) helium profiles in pure silicon and aluminum, as if there were no backing; ...) helium profiles in iron (backing), as if there were no coating; —) actual helium profiles in a two-layer system of coating—steel; X_1) origin of fine ($d < 0.5$ μm) blisters; X_2) origin of normal (typical for the given energy of He^+ ions) blisters; X_3) origin of anomalously large ($d \sim 10$ μm) blisters at the coating—backing boundary.

form surface (see, for example, Fig. 1a). Therefore, the development of blistering must have proceeded just the same as in pure aluminum (if $h > R_p$) or in steel (for $h < R_p$); i.e., according to [13, 14] in both cases peeling must have occurred. As this was not observed, then it remains to be supposed that suppression of peeling must be due to destruction of the profile of occurrence (deposition) of helium through the depth of the samples [14] and to the properties of the coating—backing system. It is possible that with different ratios of h and R_p, different suppression mechanisms of blistering act. Let us consider from these aspects the results obtained.

In accordance with the calculated values of the range of He^+ ions in Si, Al, and Fe (steel) [15], a thickness of the silicon coating of 20 nm amounts to ∿10 and 6% of R_p for He^+ ions with energy 20 keV and 40 keV in silicon, i.e., the silicon film cannot significantly deform the distribution of helium (and defects) in the backing (Fig. 5a), and the whole process of the creation of blisters, including the formation of helium bubbles and primary cracks, takes place in the depth of the steel backing. At the same time, the difference in thickness of the blister caps on samples of steel without coating (275 ± 90 nm) and with a silicon coating (305 ± 175 nm) mentioned above confirms that silicon, firstly, in practice does not reduce the range of He^+ ions in steel (see Fig. 5a) and, secondly, somewhat shifts the site of formation of a blister crack into the depth of the target.

This shift can be due to a number of causes, to which can be related a change of mechanical properties and, in particular, an increase of the strength and rigidity of the surface layer of the steel as a result of the implantation of silicon atoms and an increase of the dislocation density in consequence of the Rebinder effect. An electron-microscopic investigation of the dislocation structure of steel with and without coating confirms the higher dislocation density in the near-surface layers of samples with a coating. An increase of strength of the implanted layer promotes an increase of the level and gradient of the lateral compressive stresses originating during the implantation of helium ions, which, evidently, causes a redistribution of helium into the depth of the target. Hardening of the material, moreover, increases the resistance of the steel to blister formation. As a result of the combined effect of the thin silicon coating, the effect of suppression of blistering is observed during irradiation with ions of energy 20 and 40 keV.

The characteristic feature of the effect on the blistering of aluminum coatings is the dependence of the blister sizes on the thickness of the film. In order to refine this relation, we shall carry out an analysis of the relation between the average ranges of helium ions and the thickness of the coating in a two-layer system of aluminum—steel, shown in Fig. 5. This system, with $h = R_p/2$ and $h = R_p$, distorts the profiles of the helium distribution. With $h \leqslant R_p$ (for h = 80 and 160 nm), the helium distribution profile includes the coating—backing

bour[illegible] is wholly located in the coating (see Fig. 3d). The overlap by the helium distribution of the boundary of separation at a thickness of 80 and 160 nm, obviously, is the principal cause of formation of the anomalously large convex blisters (see Fig. 3c). With h = 320 nm, the escape of helium at the coating–backing boundary also is possible in principle, but in a much smaller quantity by comparison with the thicker coatings, and therefore the number of such blisters also is significantly less (see Fig. 3b). In all cases, the aluminum–steel boundary of separation is the site of the preferable accumulation of helium and the formation of blisters. The correlation between the diameters of the coarse blisters and the thickness of the coating testifies in favor of this supposition. In fact, if the diameter of the blisters is related with the thickness of the cupola as $d \sim t^k$, where k is a constant, then in the case of the formation of blisters at the coating–steel boundary, the ratio $\log d_1/\log h_1 = \log d_2/\log h_2 = \log d_3/\log h_3$ must be satisfied. If we take the maximum sizes of the coarse blisters from Table 2 (d_1 = 5.2 μm, d_2 = 9.0 μm, and d_3 = 12.0 μm) on samples with coatings of thickness h_1 = 80 nm, h_2 = 160 nm, and h_3 = 320 nm, respectively, then this equation is satisfied quite well, and taking account of the error in the measurement of the blister diameters and the thickness of the coatings, the ratio $\log d_i/\log h_i$ amounts to 1.790 ± 0.154.

The relative increase of the fraction of coarse blisters with increase of the irradiation temperature also testifies in favor of the supposition concerning the escape of helium at the boundary and the role of the boundary in the formation of anomalously large blisters. It should be emphasized that the coarse blisters are ruptured in the first place with increase of the temperature of the samples to 470°K. However, with increase of the coating thickness to 180 and 320 nm, the effect of temperature on erosion is weakened (see Table 2), as the blisters with a thick cap are in a position to endure a greater plastic deformation than blisters with h = 80 nm.

Thus, the results in this paper confirm the feasibility of reducing the erosion of the primary wall of thermonuclear facilities and reactors by the use of coatings deposited by thermal sputtering in vacuo and coatings obtained by aluminization. At the same time, for a choice of the optimum coatings, in order to reduce radiation erosion, to refine the mechanisms of suppression of blistering, and to study the behavior of helium in two-layer systems, further investigations in this direction are necessary.

LITERATURE CITED

1. J. Davis and G. Kulcinski, "Major features of DT tokamak fusion reactor systems," Nucl. Fusion, 16, No. 2, 355-373 (1976).
2. B. A. Kalin, N. M. Kirilin, D. M. Skorov, and V. G. Tel'kovskii, Problems of the Choice of Materials for Thermonuclear Reactors, in: Reports of the All-Union Conference on Engineering Problems of Thermonuclear Reactors [in Russian], Vol. 1, D. V. Efremov Scientific Research Institute of Electrophysical Equipment, Leningrad (1977), pp. 114-119.
3. I. V. Gorynin, Sh. Sh. Ibragimov, O. A. Kozhevnikov, et al., "Special features of structural transformations in high-nickel austenitic alloys and their effect on radiation damage," in: Reactor Material Behavior [in Russian], Central Scientific-Research Institute of Atomic Information, Moscow, Vol. 2 (1978), pp. 274-316.
4. E. E. Goncharov, M. I. Guseva, B. A. Kalin, et al., "Effect of thermal treatment and alloying on the radiation erosion of austenitic stainless steels and alloys," At. Energ., 53, No. 4, 243-250 (1982).
5. R. Behrisch and B. Kadomtsev, "Plasma impurities and their significance in fusion reactors," in: Proc. Int. Conf. on Plasma Physics and Controlled Thermonuclear Fusion Research, Vienna, Vol. 2 (1975), pp. 229-249.
6. G. Kulcinski, R. Conn, and G. Lang, "Reduction of plasma contamination effects and first-wall erosion in fusion devices," Nucl. Fusion, 15, 327-333 (1975).
7. K. Wilson, G. Thomas, and W. Bauer, "Reduced erosion in helium implanted aluminum coatings," J. Nucl. Mater., 61, No. 1, 113-116 (1976).
8. M. I. Guseva, E. S. Ionova, and Yu. V. Martynenko, "The problem of erosion of the first wall of the tokamak facility," At. Energ., 48, No. 3, 162-166 (1980).
9. E. S. Ionova, B. A. Kalin, P. I. Kartsev, et al., "Investigation of the erosion resistance of aluminized steel during irradiation with helium ions," Fiz. Khim. Obrab. Mater., No. 3, 8-11 (1983).
10. L. B. Begrambekov, O. A. Malofeev, S. B. Skulanov, and V. G. Tel'kovskii, "Angular distribution of atoms, sputtered from a metallic surface by light ions," in: Interaction of Atomic Particles with a Solid Body [in Russian], Kharkov State Univ., Pt. 1 (1976), pp. 100-127.

11. accelerator with ion separation by mass," Prib. Tekh. Eksp., 4, 19-25 (1969).
12. B. A. Kalin, S. N. Korshunov, D. M. Skorov, and V. L. Yakushin, "Blistering of materials during cyclic irradiation over a wide spectrum of incidence of the ions," At. Energ., 49, No. 2, 132-134 (1980).
13. W. Bauer and G. Thomas, "Helium implantation effects in SAP and aluminum," J. Nucl. Mater., 63, No. 1, 299-306 (1976).
14. V. V. Gann, I. M. Neklyudov, L. I. Pivovar, et al., "Structure of the surface of stainless steel after irradiation with a beam of helium ions, scanning with depth," Problems of Nuclear Science and Technology. Series Physics of Radiation Damage and Radiation Material Behavior [in Russian], No. 1(12) (1980), pp. 79-82.
15. A. F. Burenkov, T. I. Zhukova, F. F. Komarov, et al., Distribution of Ranges of Accelerated Ions. Isotopes of Helium and Lithium [in Russian], Preprint IAÉ-3468/6, Institute of Atomic Energy, Moscow, p. 60.

OPTIMIZING EXTRACTANT MOLECULAR STRUCTURE FOR REPROCESSING SPENT NUCLEAR POWER STATION FUEL

A. M. Rozen, A. S. Nikiforov, V. S. Shmidt,
Z. I. Nikolotova, N. A. Kartasheva, and B. S. Zakharkin

UDC 621.039.59

Researches in the USSR and elsewhere have been designed to improve solvent-extraction systems based on tributyl phosphate (TBP), which is widely used throughout the world in reprocessing spent nuclear power station fuel, particularly to eliminate the disadvantages of TBP: its relatively high solubility in water and the formation of a third phase in the extraction of high concentrations of actinoids(IV).

In the USSR, it has been suggested [1, 2] that tributyl phosphate should be replaced by esters of phosphoric acid (trialkyl phosphates) having long branched hydrocarbon chains: total number of carbon atoms N_C from 14 to 21. In [3, 4], there is a discussion of improving extraction systems by replacing the diluents, and it is also stated that TBP can be replaced by trialkyl phosphates with long hydrocarbon chains (N_C = 15.21) having isomeric structures.

A review from the USA [5] states that trihexyl phosphate (N_C = 18) has advantages over TBP, as does triisooctyl phosphate (N_C = 24), but no data are given to confirm this. Recommendations supported by data are to be found in [6]. The extraction agents that can replace TBP are given as trihexyl phosphate, triisooctyl phosphate, triisoamyl phosphate (N_C = 15), and triisohexyl phosphate (N_C = 18). It was stated that successful tests have been performed on solvent extraction with a cascade of mixers and settlers in hot cells.

Here we provide a scientific basis for optimizing the reagent structure and confirm the conclusions of [1-4].

Advantages and Disadvantages of Tributyl Phosphate

Tributyl phosphate has been widely used in the last 30 years because of its good extraction features [7]. On the one hand, the extraction capacity of TBP is sufficient to extract the valuable elements — uranium, plutonium, and neptunium — without the use of unextracted salting-out agents; on the other, the etraction capacity of TBP is not too great, which enables one to perform the necessary technological operation of reextraction without the use of chemical reagents by reducing the acidity of the solution and raising the temperature. The selectivity of TBP is also high [7]. Therefore, TBP continues to be the main reagent in radiochemical technology, although we now know of neutral compounds having incomparably higher extraction capacity, such as the phosphine oxides, but the reextraction of metals from such media requires the additional use of effective chemical reagents.

Translated from Atomnaya Énergiya, Vol. 58, No. 1, pp. 38-43, January, 1985. Original article submitted May 28, 1984.

0038-531X/85/5801-0045$09.50

quadrivalent metals (plutonium and thorium) are poorly compatible with hydrocarbon diluents [8, 9]. For example, if one uses a 30% solution of TBP in n-dodecane, a second organic phase is formed when the plutonium concentration in the extract is about 40 g/liter [10], and the same occurs with n-tetradecane at 20 g/liter. It has previously been demonstrated [8] that there is a deterioration in the compatibility as the hydrocarbon chain in the diluent lengthens by reference to systems containing U(VI) and Th(IV). This disadvantage is particularly undesirable in reprocessing spent fuel from fast reactors.

Secondly, there is the comparatively high (about 0.4 g/liter) solubility of TBP in the aqueous phase, which leads to losses of the agent and contamination of the extracted metals with phosphorus, which is accentuated when the diluents are long-chain hydrocarbons.

Thirdly, rates of hydrolysis and radiolysis of TBP are comparatively high.

It is thus of practical interest to synthesize extraction agents having the extraction capacity of TBP but with improved physicochemical characteristics and at least free from the first of these two disadvantages.

Possible Solutions

A solution is available from the following results on the physical chemistry of extraction and the relation between extraction capacity and structure [8, 11-14]. An electron donor–acceptor mechanism is involved in the formation of complexes between metals and organophosphorus compounds $R_1R_2R_3PO$ (the donor is the phosphoryl oxygen and the acceptor is the metal atom). The strength of the complex is the higher, the larger the electron density on the oxygen, and the latter is determined by the electronegativity of the substituents X_R. The larger X_R, the lower the electron density and correspondingly the extraction. The substituent electronegativities are dependent on the chemical natures of them, being lowest for the alkyl radicals C_nH_{2n+1} ($X_{Ra} = 2.0$ for $n \geq 4$). For the alkoxy groups $C_RH_{2n+1}O$, the electronegativities are much higher ($X_{RO} = 2.9$), so replacing the RO group by R increases the extraction, which increases in the series from phosphates (3 RO groups, $\Sigma X = 8.7$) to the phosphonates ($\Sigma X = 7.8$) and onward to the phosphine oxides (3 R groups, $\Sigma X = 6$). The extraction capacity is very sensitive to the nature and electronegativity of the substituents: for example, replacing one RO group by R raises the extraction constants for uranium and plutonium nitrates by factors of 50 [11-14]. On the other hand, the length of the hydrocarbon chain has little effect on the extraction capacity. The changes are appreciable only for short radicals: $n_C = 1$ and 2 for methyl ($X_{CH_4} = 2.07$) and ethyl ($X_{C_2H_4} = 2.02$), while $X \approx 2$ on further extension, and the electron density on the oxygen remains virtually constant, and there is little change in extraction capacity. When allowance is made for the effects of the steric factor on the $K_{extr} = f(n_C)$ curves, one finds a weak maximum at $n_C = 8$ [8, 12].

Therefore, there is virtually no change in the chemical parameters of the reagent or the extraction capacity when the hydrocarbon chain length alters, whereas the physicochemical properties (solubility and capacity to form a second organic phase) are very much dependent on the chain length and structure. Therefore, if one wishes to keep the extraction performance at the TBP level, one must keep substituents of the same chemical nature, i.e., one must use trialkyl phosphates $(R_1O)(R_2O)(R_3O)PO$, where $R = C_nH_{2n+1}$. The necessary changes in the physicochemical properties must be obtained by varying the length and structure of the hydrocarbon chain.

The separation of organic solutions of the actinoids into two phases is a consequence of the high positive deviation from ideal behavior (large values of the activity coefficients* γ [8]), which is due to the large differences in the intermolecular force fields and in the solubility parameters δ of the solvate $Me(NO_3)_4(TBP)_2$ and the n-alkanes (we recall that $RT\ln\gamma = V(\delta^2_{sol} - \delta^2_{alk})$. To reduce the difference in the δ (or rather in the dispersion components) and thereby improve the compatibility of the solvates and the long-chain n-alkanes, it is necessary to make the hydrocarbon chains more nearly equal in length, i.e., to lengthen the hydrocarbon chains in the ester, and also to use the iso structure. The same measures will also tend to weaken the association between the complexes, which is a major reason (if not the main one) for the large positive deviations from Raoult's law (positive nonideal behavior) in the system formed by the complex with the n-alkane. Lengthening the hydrocarbon chain also reduces the solubility of the ester in the aqueous phase.

*For example, the activity coefficient of the solvate of thorium in hexane amounts to $\sim$60 [8].

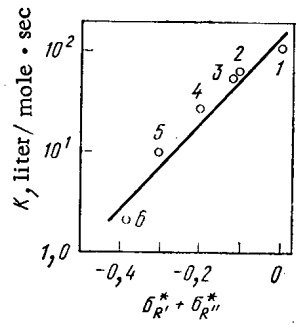

Fig. 1

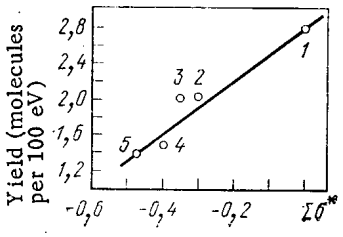

Fig. 2

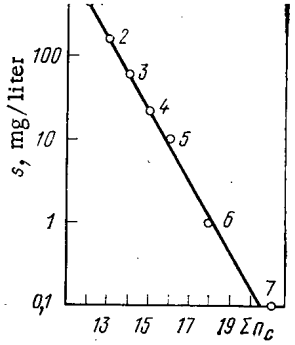

Fig. 3

Fig. 1. Effects of structure of the esters (RO)(R')P(O)F on the rate constants K for hydrolysis at 25°C constructed from the data of [15] for R/R': 1) CH_3/CH_3; 2) C_2H_5/CH_3; 3) n-C_3H_7/CH_3; 4) iso-C_3H_7/CH_3; 5) iso-C_3H_7/C_2H_5; 6) iso-C_3H_7/iso-C_3H_7.

Fig. 2. Effects of structure in the esters $(C_nH_{2n+1}O)_3PO$ on the yields of dialkyl phosphoric acids on irradiation constructed from the data of [23], the numbers by the points being the values of n.

Fig. 3. Dependence on the overall length of the hydrocarbon chains Σn_C for the water solubilities of trialkyl phosphates: 1) TBP; 2) DiBiAP; 3) iBDiAP; 4) TiAP; 5) DiBiOP; 6) TiHP; 7) TiHepP.

There is the following basis for reducing the phosphate hydrolysis. The data of [15] on hydrolysis rates for organophosphorus compounds (Fig. 1) can be described by the equation

$$\lg K_{hyd} = 2 + 4\Sigma\sigma^* = 2 + 8\Sigma\,(X - 2.07),$$

where σ^* is the Taft constant, $\sigma^* \approx 2(X - 2.07)$ [12]. Therefore, to reduce the hydrolysis, the electronegativity of the substituents should be reduced as much as possible, which can be done by using long-chain iso structures (there is a positive effect on the hydrolysis from going to the iso structure, namely from TBP to TiBP [16]). However, the scope for this is very limited, since the changes in X and σ^* are small: while $\sigma^* = 0$ for the methyl radical, $\sigma^* = -0.13$ for n-butyl and n-amyl, and $\sigma^* = -0.16$ for isoamyl, i.e., $\Delta\sigma^* = 0.03$, $\Delta X = 0.015$. The above equation was used in the forecast, according to which $\Delta \log K_{hyd} = 8\Sigma\Delta X$, together with the values of the Kabachnik constant σ^Φ, which for C_3H_7, C_4H_9, and C_5H_{11} are −1.18, −1.22, and −1.21, while for the iso analogs they are −1.30 and −1.27 [17]. As $X \approx 2.4 + \sigma^\Phi/3$ for alkyl groups, the changes in electronegativity on going to the iso structure for C_4H_9 and C_5H_{11} are −0.027 and −0.02 ($\Delta X = -0.017$ if we take −1.22 for C_5H_{11}). As $\Sigma\Delta X = 3\Delta X$, the reduction in the hydrolysis rate predicted by the above equation for the n-C_4H_9/iso-C_4H_9 pair is about a factor 4.3, while for the pair n-C_4H_9/iso-C_5H_{11} it is from −2.5 to 3. A relationship analogous to this equation is also obeyed by the radiolysis rate (Fig. 2), but the dependence is much weaker: the yield of radiolysis products should be reduced by about 7% as Σn_C goes from 12 to 15.

Experimental Check on the Theoretical Forecasts

To check these forecasts and to identify the optimum structures, we synthesized trialkyl phosphates with hydrocarbon chains longer than in TBP and with the iso structures indicated in Table 1, and we examined their physicochemical and extraction features.

We also synthesized acid phosphates, which enabled us to examine the purification of the reagents from acid impurities.

Physicochemical Parameters of Trialkyl Phosphates Having Optimized Hydrocarbon Chains.

To establish the lower and upper bounds to the overall chain length, we examined the solubilities of the esters in water (which determines the lower limit to Σn_C) and the washing of the reagents free from acid impurities (which determines the upper limit to Σn_C). Figure 3 shows that the forecast is confirmed: an increase as Σn_C reduces the solubility in water s to any desired extent (s decreases exponentially as Σn_C increases, which corresponds to a known regularity [18]). With Σn_C = 13-14, the solubility is still quite large, but increasing the number of carbon atoms to 15-16 reduces the solubility by comparison with TBP by more than an order of magnitude, which is sufficient.

Name	Abbreviation	Formula	Σn_C	Density, kg/dm³
Diisobutyl isoamyl phosphate	DiBiAP	$(iC_4H_9O)_2(iC_5H_{11}O)PO$	13	0,962
Isobutyl diisoamyl phosphate	iBDiAP	$(iC_4H_9O)(iC_5H_{11}O)_2PO$	14	0,955
Triisoamyl phosphate	TiAP	$(iC_5H_{11}O)_3PO$	15	0,950
Diisobutyl isooctyl phosphate *	DiBiOP	$(iC_4H_9O)_2(iC_8H_{17}O)PO$	16	0,944
Triisohexyl phosphate	TiHP	$(iC_6H_{13}O)_3PO$	18	0,938
Triisoheptyl phosphate	TiHepP	$(iC_7H_{14}O)_3PO$	21	0,922
Triisooctyl phosphate *	TiOP	$(iC_8H_{17}O)_3PO$	24	0,918

*Isooctyl is 2-ethylhexyl.

TABLE 2. Results from Soda Washing

Reagent	Acid impurity	Distribution coefficient for $(RO)_2POONa$	Degree of elution in one contact for O:W = 5.0%
TBP	$(C_4H_9O)_2POOH$	$0,7\cdot10^{-2}$	> 96
iBDiAP	$(iC_4H_9O)(iC_5H_{11}O)POOH$	—	—
TiAP	$(iC_5H_{11}O)_2POOH$	$2,3\cdot10^{-2}$	90
DiBiOP	$(iC_4H_9O)_2POOH$	$0,7\cdot10^{-2}$	> 96
	$(iC_4H_9O)(iC_8H_{17}O)POOH$	$7\cdot10^{-2}$	74
TiHP	$(iC_6H_{11}O)_2POOH$	10^{-1}	67
THP	$(C_6H_{11}O)_2POOH$	$1,1\cdot10^{-1}$	66
TiHepP	$(iC_7H_{15}O)_2POOH$	$3,4\cdot10^{-1}$	40
TiOP *	$(iC_8H_{17}O)_2POOH$	2,0	9

*In three washings with n = 10, the concentration of TiOP (D2EHPA) was reduced by about 13%.

The upper limit to the chain length must be chosen on the basis that as Σn_C increases, there is an increase in the distribution coefficient for the sodium alkyl phosphates $(RO)_2POONa$ formed on soda washing of the reagent to remove hydrolysis and radiolysis products (the dialkyl phosphoric acids $(RO)_2POOH$), with a corresponding deterioration in the washing effect. Experiments on soda washing (1.09 moles/liter solution in saturated hydrocarbons) were performed with a volume ratio O:W = 5:1, with especially synthesized acis impurities added to the organic solution (Table 2).

The data show that heptyl and octyl compounds (Σn_C = 21-24) result in the acid impurities not being well eluted. This means that we should have $\Sigma n_C \leq 18$, and the subsequent development was based on esters having Σn_C = 15-18.

Checking Compatibility of the Esters with the Hydrocarbon Diluent. We tested the extraction of Th(IV) nitrate from 3 moles/liter HNO_3 and solutions of certain phosphates of concentration 1.09 moles/liter in n-tetradecane. Table 3 and also Fig. 3 of [2] give the results. The theoretical forecast is confirmed: extending the chain to Σn_C = 15-16 improves the compatibility with the normal hydrocarbon diluent to the necessary extent for the trialkyl phosphate complexes of plutonium and thorium nitrates.*

Effects of the Iso Structure and Chain Length on the Hydrolytic and Radiation Stability of Organophosphorus Extraction Agents. The yields of hydrolysis products were measured by heating the compounds to 96°C with 2 moles/liter HNO_3 for 12 h. The results are given in Table 4 (TBP is taken as 100%). The above suggestions are confirmed, but only qualitatively: the hydrolysis rates decrease somewhat as the radicals lengthen and are appreciably reduced when the iso structure is employed, but the effects of both factors weaken as the chain

*It has been found [8, 9] that the solvates of Pu(IV) nitrate are more compatible with n-alkanes than are Th(IV) solvates.

Th(IV) at Which the Second Organic Phase Is Formed

Phosphate	Σn_C	[Th] in organic phase	[Th] in aqueous phase
TBP	12	23	18
TiAP	15	65	265
DiBiOP	16	Not formed	
TiHP	18	Not formed	

TABLE 4. Hydrolytic Stability of Esters

Reagent	Yield of acid hydrolysis products, %	Theoretical forecast, %
TBP	100	100
TAP*	90	80
TiAP	78	33—40
DiBiOP	60	33
TiHP	60	—
TiBP†	35	23

*Tri-n-amyl phosphate.

†Triisobutyl phosphate. Unfortunately, the TiBP complexes formed by uranium and plutonium produce a second organic phase with the normal hydrocarbon diluent even at low concentrations, although the isostructural effect is larger for these (the results of [16] are confirmed); the solubility of TiBP in water is also comparatively high.

between Equilibrium Phases

Compound	Concentration in aqueous phase	Concentration in organic phase			
		TBP	TiAP	DiBiOP	TiHP
HNO_3, moles/liter	1	0,23	0,24	0,23	0,23
HNO_3, moles/liter	3	0,61	0,61	0,62	0,61
$UO_2(NO_3)_2$, moles/l.	0,1	0,35	0,36	0,35	0,36
$UO_2(NO_3)_2 + 3HNO_3$, moles/liter	0,3	0,46	0,47	0,46	0,48
$Th(NO_3)_4$, g Th/liter	15	19	20	19	20
$Th(NO_3)_4 + 3$ moles/liter HNO_3, g Th/liter	60	Two phases	40	39	41

TABLE 6. Distribution Coefficients for Trace Amounts of Elements between the Organic and Aqueous Phases α on Extraction from Nitric Acid Solution (3 moles/liter HNO_3)

Compound	TBP	TiAP	DiBiOP	TiHP
$Pu(NO_3)_4$	11	12	11,5	12,5
$Np(NO_3)_4$	3,5	3,6	3,5	3,7
$Zr(NO_3)_4$	0,19	0,19	0,18	0,20
Ru*	1,2	0,9	1,1	1,0

*Contact time 5 min, O:W = 0.1.

lengthens. Also, the effects are appreciably less than those predicted.

The changes in radiolytic resistance were small (the differences from TBP were within the experimental accuracy). One assumes that using the iso structure and lengthening the chain would enable one to reduce the hydrolysis rate somewhat and thereby increase the working life.

Phase Separation Rate. We compared the rates of phase separation in systems containing TBP (volume fraction 30%) and DiBiOP (35%) in n-dodecane; the aqueous phases were 3 moles/liter HNO_3 and 3 moles/liter HNO_3 + 300 g/liter U(VI), the mass proportion of Na_2CO_3 was 5%. We used the simplest method [19]: the two solutions were shaken together in a graduated cylinder (with O:W = 1:1).

We found that the separation rates in systems containing TiAP were approximately as with TBP, while they were somewhat lower with DiBiOP (for example, 1.9 mm/sec for TBP with 3 moles/liter HNO_3, but 1.4 mm/sec with DiBiOP). Therefore, replacing TBP by esters with longer chains has little effect on the phase separation time. The fire hazard naturally is somewhat reduced as the hydrocarbon chain lengthens, since the flashpoint increases.

Extraction Parameters of Trialkyl Phosphates Having Optimized Hydrocarbon Chains. Tables 5 and 6 and also [2] give some data on the extraction parameters of trialkyl phosphates having Σn_C = 15-18. We used solutions in n-tetradecane of concentration 1.09 moles/liter.

The data show that the theoretical forecast is completely confirmed. The extraction parameters for the proposed compounds are virtually the same as those for TBP, although an exception must be made for elements extracted in the form of trisolvates (Am, Tc, and so on), where steric hindrance (iso structure and elongated hydrocarbon chain) reduces α (Fig. 4).

Laboratory Check on Valuable-Element Extraction. The mathematical description and simulation of the extraction [20, 21] indicate that the technological parameters are entirely determined by the distribution coefficients for the target elements and fission products. We

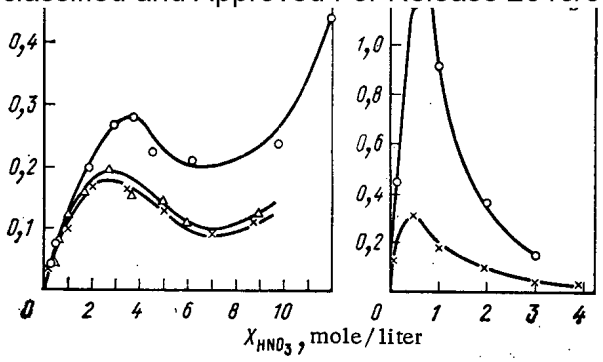

Fig. 4. Dependence of the distribution coefficients for Am (a, undiluted reagents) and Tc (b, volume proportion of reagents in n-dodecane 30%) on the equilibrium nitric acid concentration in the aqueous phase: ○) TBP; △) TiAP; ×) DiBiOP.

have shown that the test esters and TBP have virtually identical extraction performance, which means that the technological parameters in the extraction and purification of the elements in multistage systems should be identical.

This conclusion was additionally confirmed on the operations of solvent extraction, washing, and reextraction for uranium and plutonium. The experiments were performed by Alder's method of countercurrent simulation [22]. The method was used in multistage extraction of the uranyl and plutonium nitrates followed by washing. The acidities of the initial and wash aqueous solutions were 3 moles/liter. Five extraction stages and three wash stages were used. The initial uranium concentration was 300 g/liter, and that of plutonium was 300 mg/liter, with O:W = 3.3 in the flows of reagents, while O:W = 10 in the wash section (Table 7). We also performed experiments on four-stage reextraction of uranium from the organic phase with acidified water (0.05 mole/liter HNO_3) with a flow volume ratio of 1:1 at 30°C (Table 8).

Tables 7 and 8 show that these reagents provide a high extraction of the valuable components when used in place of TBP. The simulation data [20, 21] show that identical distribution coefficients for fission products (for example, Zr and Ru in Table 6) do not adversely affect the purification coefficients K_p for the valuable elements relative to the fission products* (provided that the technical reagents have the same purity as TBP, which can be checked by measuring the distribution coefficients given in Table 6). Another important point is that the technical reagent and the hydrolysis products from it should not contain surface-active impurities capable of increasing the phase unmixing time appreciably or of stabilizing the emulsion (this can also be checked under cold conditions).

These studies completely confirm the theoretical forecasts and show that trialkyl phosphates with lengthened chains and the iso structure are practically identical with TBP as regards extraction behavior, which applies whether they are symmetrical in radicals (TiAP and TiHP) or have different radicals (DiBiOP), while they have two major advantages: increased compatibility of the actinoid(IV) solvates with long-chain normal hydrocarbon diluents (the undesirable formation of the second organic phase is virtually excluded), and lower solubility in the aqueous phase. The hydrolytic stabilities are also increased somewhat. These advantages are attained while retaining the parameters for the recovery and purification of the valuable elements at the level of those for TBP.

*$K_p = 1/(\alpha_1^l n')(\alpha_2^l n')\ldots(\alpha_l^l n')$ (α, n), where α is the distribution coefficient (α_1 is the supply stage), n is the ratio of the phase flows, a prime denotes a quantity in the wash section, and l is the number of wash stages [20].

TABLE 7. Results from the Extraction-Washing Stage (trialkyl phosphate concentration 1.09 mole/liter)

Reagent	N_C	Uranium in outgoing organic phase, g/liter	Uranium contents of tail solutions, mg/liter	Degree of uranium extraction, %	Plutonium content of tail solution, mg/liter	Degree of plutonium extraction, %
TBP	12	91	30	99,99	0,06	99,98
TiAP	15	91	20	99,99	0,05	99,98
DiBiOP	16	91	20	99,99	0,05	99,98
TiHP	18	91	20	99,99	0,05	99,98

TABLE 8. Results on Uranium Reextraction

Reagent	Uranium content in reextract, g/liter	Residual uranium in organic phase, mg/liter	Degree of uranium extraction, %
TBP	91	3	99,996
TiAP	91	2	99,996
DiBiOP	91	2	99,996
TiHP	91	2	99,996

1. A. M. Rozen, A. S. Nikiforov, V. S. Shmidt, et al., Inventor's Certificate No. 841140, Byull. Izobret., No. 14, 319 (1982) (with priority from 7.2.80).
2. A. M. Rozen, Z. I. Nikolotova, N. A. Kartasheva, V. S. Shmidt, and A. S. Nikiforov, Dokl. Akad. Nauk SSSR, 27, No. 5, 1139 (1984).
3. A. S. Nikiforov, V. S. Shmidt, and A. M. Rozen, Abstracts for the Twelfth Mendeleev Congress [in Russian], Vol. 1, Nauka, Moscow (1981), p. 182.
4. A. S. Nikiforov, V. S. Shmidt, A. M. Rozen, and A. P. Ilozhev, Radiokhimiya, 24, No. 5, 631 (1982).
5. R. Shonn and R. McDowell, in: Proc. Symp. Actinide Separation, Am. Chem. Soc., Ser. 117, Washington, D.C. (1980), p. 71.
6. D. Crouse, W. Arnold, and F. Hurst, in: Int. Proc. Conf. Solvent Extraction Chem. ISEC-1983 (ORNL), pp. 90-91.
7. H. McKay, "TBP — meeting-point of science and technology," in: Proc. Conf. Solvent Extraction Chemistry, Gothenburg, North-Holland, Amsterdam (1967), p. 185.
8. A. Rozen, in: Proc. Conf. Solvent Extraction Chemistry, Gothenburg, North-Holland, Amsterdam (1967), p. 223; Radiokhimiya, 10, No. 3, 273 (1968).
9. A. Mills and W. Logan, in: Int. Proc. Conf. Solvent Extraction Chem. ISEC-1983 (ORNL), p. 322.
10. V. E. Vereshchagin and É. V. Renard, At. Energ., 44, Issue 5, 422 (1978); 45, Issue 1, 45.
11. A. M. Rozen and Z. I. Nikolotova, Zh. Neorgan. Khim., 9, No. 7, 1725 (1964).
12. A. M. Rozen et al., Proceedings of the Third Geneva Conference, 1964, USSR Paper No. 364.
13. A. M. Rozen, "Controlling the extraction capacities of organic compounds," in: Hydrometallurgy [in Russian], Nauka, Moscow (1976), p. 194.
14. A. M. Rozen, Z. I. Nikolotova, and N.A. Kartasheva, Zh. Neorg. Khim., 24, No. 6, 1642 (1979).
15. R. D. O'Brien, Toxic Phosphorus Esters, Academic Press (1960).
16. V. V. Yakshin and E. A. Filippov, Radiokhimiya, 19, No. 6, 715 (1977).
17. T. A. Mastryukova and M. I. Kabachnik, Usp. Khim., 38, Issue 10, 1751 (1969).
18. G. Pierotti et al., Ind. Eng. Chem., 51, No. 1, 95 (1959).
19. V. G. Voden, N. E. Obukhov, and M. F. Pushlenkov, Radiokhimiya, 18, No. 5, 722 (1976).
20. A. Rozen, At. Energy Rev., 6, No. 2, 98 (1968).
21. A. M. Rozen and Yu. V. Reshet'ko, At. Energ., 37, No. 3, 187 (1974).
22. L. Alders, Liquid–Liquid Extraction, Am. Elsevier (1959).
23. G. F. Egorov, in: Proceedings of the Third COMECON Symposium on Research on Reprocessing Irradiated Fuel [in Russian], Vol. 1, KAE Czechoslovakia, Prague (1975), p. 302.

DETERMINATION OF THE EFFICIENCY OF A DETECTOR IN GAMMA SPECTROMETRY OF LARGE-VOLUME SAMPLES

É. G. Tertyshnik and A. T. Korsakov

UDC 539.1.074.55:539.166.06

Measurements on large-volume (up to 1000 ml) preparations in the analysis of environmental samples and samples of rocks is an important problem of applied gamma spectrometry, whose accuracy is in many ways determined by the technique used. The use of the method of direct comparison with a standard presumes the existence of reference or standard preparations, containing a known amount of gamma-emitting nuclides, uniformly distributed in a nonactive inert filler. The standard preparation must exactly model the sample both with respect to geometrical dimensions and with respect to the coefficient of attenuation of γ radiation in the filler material. The technique used to prepare standard preparations is quite complicated, since it is necessary to ensure a uniform distribution of the introduced radioactive substance by repeated mixing while avoiding uncontrollable losses of radionuclides [1]. In addition, the samples to be analyzed have a different chemical composition and are distinguished by their bulk density (samples of ion-exchange resin, soil samples, ashes from plants, etc.). For this reason, the coefficients of attenuation of radiation in the sample and in the sample preparation are practically never equal, and the reliability of the results obtained by the method of direct comparison with a standard is lowered. In many laboratories γ-spectrometric analyses are performed with the help of detectors whose efficiency is known.

The calibration of detectors over a wide range of γ-quanta energies is performed by filling measuring containers of standard sizes with water and adding standard radioactive solutions (SRS) to the water. Since the mass of the added SRS is determined on analytical scales and an ideal distribution of radionuclides over the container volume is ensured in the water, the detection efficiency is measured with high accuracy. By detection efficiency of γ quanta we mean the ratio of the number of counts recorded under the total absorption peak during a chosen interval of time to the number of γ quanta arising in the preparation over the same time interval. The number of γ quanta arising in the preparation is calculated starting from the mass of the sample solution introduced into the container and the data on the certificate accompanying the SRS.

The calibration curves obtained can be used to calculate the content of radionuclides in the soil samples, bottom deposits, etc., if the radionuclides being determined emit hard γ rays (for example, cesium 137), since it is known that for high γ-ray energies the self-absorption of radiation is approximately the same in water and in the sample material.

In the general case, the efficiency $\varepsilon(E)$ of detection of γ radiation from the sample, placed in a standard container, differs from the values $\varepsilon_0(E)$ which are obtained for the container filled with water with known specific activity. This difference is all the more noticeable the larger the difference between the attenuation coefficients of the sample materials and the water.

In this paper we examine a method which permits determining the coefficient $\omega(E) = \varepsilon/\varepsilon_0$ and, therefore, calculating the function $\varepsilon(E)$, if the dependence $\varepsilon_0(E)$ for water has been obtained, for a sample with arbitrary density and unknown chemical composition.

Quantity ω is a function of the geometrical dimensions of the preparation and of the detector, their mutual arrangement, and also the attenuation coefficients of the sample material and the water. The flux density of γ rays for volume sources with different configuration was calculated, taking into account self-absorption, in [2] by integrating the effects produced by point sources taking into account the attenuation kernels (the influence function of a point source). In [3] the results of such calculations were used to estimate the influence of variations in the density of the measured samples on the characteristics of the γ-spectrometric setup with a small number of channels.

Translated from Atomnaya Énergiya, Vol. 58, No. 1, pp. 44-47, January, 1985. Original article submitted March 20, 1984.

 0038-531X/85/5801-0052$09.50

rays Φ ($cm^{-2} \cdot sec^{-1}$) at the center of its base is equal to

$$\Phi = SG(\mu H, \mu R)/2\mu,$$

where S is the specific yield of the volume source, i.e., the number of quanta emitted per unit volume per unit time, $cm^{-3} \cdot sec^{-1}$; μ is the linear coefficient of attenuation of radiation, cm^{-1}; G is a special function whose values are found from the curves in [2, 4]. Therefore, for a cylindrical container the coefficient ω can be determined from the following formula

$$\omega = \mu_0 G(\mu H, \mu R)/\mu G(\mu_0 H, \mu_0 R). \quad (1)$$

A source in the form of a hemisphere with radius l creates at the center of its base a γ-ray flux density of

$$\Phi = S[1 - \exp(-\mu l)]/2\mu.$$

For this reason, if the measured preparation is shaped like a hemisphere, then the coefficient ω is calculated using formula (2). The same formula is valid for a preparation in the form of a spherical layer with a thickness l with a point detector placed at the geometric center of the sphere. We note that in the latter case the value of ω does not depend on the radius of the sphere

$$\omega = \frac{\mu_0}{\mu} \frac{1 - \exp(-\mu l)}{1 - \exp(-\mu_0 l)}. \quad (2)$$

A container with a complex shape, with whose help the "well in the sample" geometry is realized (Fig. 1), can be viewed as a combination of two cylindrical sources, and the source of height h and radius r should be viewed as a source with a negative intensity. For such a container the value of ω is found from the formula

$$\omega = \frac{\mu_0}{\mu} \frac{G(\mu H, \mu R) - G(\mu h, \mu r)}{G(\mu_0 H, \mu_0 R) - G(\mu_0 h, \mu_0 r)}. \quad (3)$$

The value of the coefficient of linear attenuation of radiation, which is necessary in calculating ω, can be measured quite simply for any bulk material or liquid. It is known [5] that the flux density of unscattered γ quanta behind the absorbing layer for a diverging beam of radiation from a point source is determined from the formula

$$\Phi = \Phi_0 b^2 \exp(-\mu t)/(b + t)^2,$$

where Φ_0 is the flux density of γ quanta on the surface of the absorber, Φ is the flux density of quanta of unscattered radiation after passage through an absorber of thickness t and b is the distance from the source to the surface of the absorber.

Since at the peak of total absorption the detector registers unscattered γ quanta, and the coefficient of linear attenuation for air is small (for example, for 60-keV quanta μ = 0.00022 cm^{-1} [6]), when determining the coefficient of linear attenuation of radiation of any substance it is sufficient to: fix the source, emitting quanta with energy E_1, relative to the detector; measure the counting rate under the corresponding total-absorption peak with an empty container (a layer of air) and with the absorber placed into the container; calculate the value of $\mu(E_1)$ from the relation

$$\mu(E_1) = \frac{\ln(n/m)}{t}, \quad (4)$$

where $\mu(E_1)$ is the linear coefficient of attenuation of γ rays with energy E_1 (cm^{-1}), t is the thickness of the layer of absorbing material in the container, n is the counting rate with an empty container, and m is the counting rate with the absorber or sample placed into the container.

As sources of radiation, it is convenient to use sources from the set of standard spectrometric γ sources (SSGS). They are fixed with the help of a centering insert, placed on the top of the measurement container, as shown in Fig. 1. If the coefficient of attenuation is being measured for active samples, then m in formula (4) must be replaced by k = m — f, where f is the counting rate under the total-absorption peak corresponding to E_1, arising due to the radioactivity of the sample. When measuring f, the source 4 (see Fig. 1) must be removed.

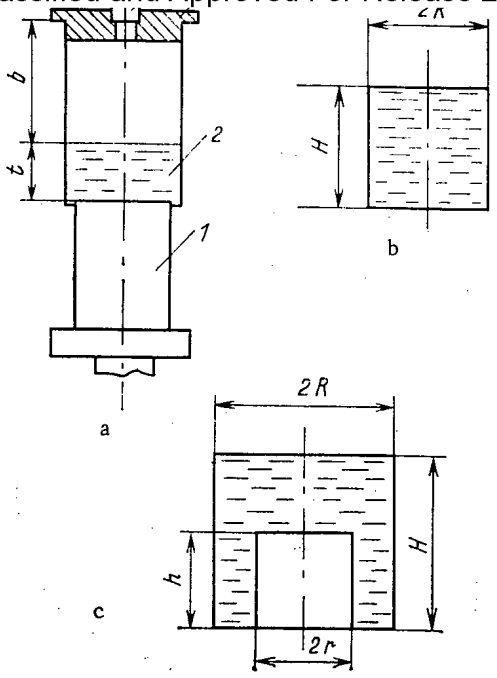

Fig. 1

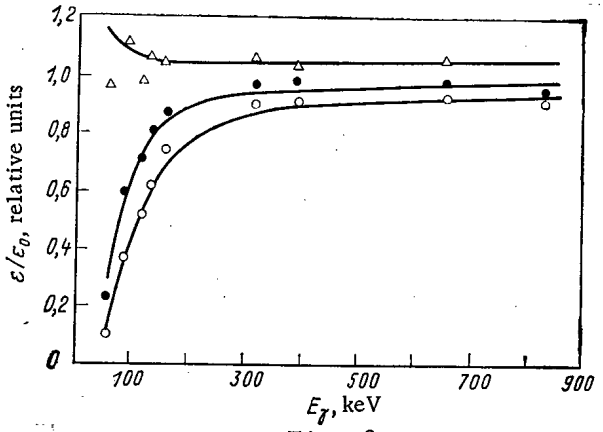

Fig. 2

Fig. 1. Measurement geometry: a) scheme for determining the coefficient of linear attenuation of radiation by the sample material: 1) detector; 2) sample; 3) stabilizing insert; 4) radiation source; b) cylindrical container with a volume of 500 cm^3 (H = 53 mm, R = 55 mm); c) complex-shaped container with a volume of 1000 cm^3 (H = 87 mm, R = 71 mm, h = 52 mm, r = 47 mm, the inner dimensions are indicated).

Fig. 2. Energy dependence of the ratio $\varepsilon/\varepsilon_0$ for materials with different density: Δ) ethanol; ●, o) solution with a density of 1.2 and 1.5 g/cm^3, respectively.

The suitability of the proposed method for calculating the efficiency was checked on a γ-spectrometric setup with a DGDK-80B Ge(Li) detector for two containers with volumes of 500 and 1000 cm^3. The diameter of the cryostat of the detector was equal to 90 mm. The values of μ were found with the help of the formula (4) for aqueous solutions of cadmium sulfate with a density of 1.2 and 1.5 g/cm and ethanol with a density of 0.8 g/cm^3. These solutions simulated samples with different attenuation coefficients. We used the numerical values of μ, characterizing solutions with different density, to calculate the coefficients ω according to formulas (1)-(3). It turned out that the values of ω obtained using formula (2) for both types of containers differ to a lesser extent from the experimental data than the values calculated using formula (1) or (3). In addition, formulas (1) and (3) are inconvenient for practical applications, because the function G(μH, μR) is not tabulated and determining the values of this function from graphs is a time-consuming process and introduces additional errors. The function Z(μH, μR, R/H, α/H), which describes the radiation field of a cylindrical volume source at a distance α from its end face, turned out to be unsuitable for calculating ω [4].

The values of ω for a complex-shaped container with a volume of 1000 cm^3, calculated using formula (2), are presented in Table 1. The table also gives the values of $\varepsilon/\varepsilon_0$ obtained experimentally. We performed the experiment as follows. We added several milliliters of the solution of radionuclide (for example, ^{241}Am) into the container with the absorber modeling the sample. After carefully mixing the contents of the container, we measured the counting rate under the corresponding total-absorption peak (60 keV) and scaled it to the volume of the solution introduced, finding the value of N, pulses/(sec·ml). We then determined the counting rate N_0, normalized to the volume of the solution introduced, with a container filled with water, tagged with the same radioactive solution, placed on the detector. Since the normalized counting rate is proportional to the detection efficiency, $\Omega = N/N_0$.

Using Formula (2) and Obtained Experimentally (Ω) for a Container with a Volume of 1000 cm³ (l = H − h)

Energy of γ rays, keV	Density, g/cm³					
	1,5		1,2		0,8	
	ω	Ω	ω	Ω	ω	Ω
60	0,18	0,18	0,38	0,37	1,1	1,01
88	0,44	0,45	0,67	0,71	1,05	1,1
122	0,64	0,65	0,79	0,80	1,03	1,03
135	0,71	0,72	0,86	0,85	1,05	1,01
166	0,78	0,82	0,91	0,91	1,02	1,02
320	0,93	0,98	0,94	1,02	1,05	1,09
392	0,92	0,97	0,96	1,06	1,02	1,05
662	0,95	0,92	0,98	0,98	1,03	0,97
835	0,95	0,91	0,99	0,97	1,02	—

In experiments of this type, powdered materials are usually used to model the sample: soda, quartz sand, chromium oxide, etc. [3]. The use of salt solutions in containers as absorbing media increases the accuracy with which $\varepsilon/\varepsilon_0$ is determined because of the uniform distribution of the radionuclides introduced over the volume of the container.

It follows from the table that for ethanol in the energy range 60-835 keV the computed and experimental values of ω are close to one. For solutions of cadmium sulfate the rms relative deviation of the computed values from the data obtained by model experiments is equal to 5%. The maximum deviation does not exceed 10%. Analogous results were obtained for a cylindrical container with a volume of 500 cm³ (Fig. 2). Taking into account the spread of the experimental data and the error in the determination of the coefficients of linear attenuation, it is evident that the computer and experimental values are in good agreement.

It has thus been shown that in order to determine the efficiency of detection of γ radiation by a detector when measuring samples with a large volume, the following are necessary:

using standard radioactive solutions, the dependence $\varepsilon_0(E)$ must be obtained with the measuring container filled with water;

the coefficient of linear attenuation of the sample material (matrix) must be determined using formula (4); the value of $\mu_0(E)$ for water can be taken from the tables [6];

the efficiency of the detector for radiation from the sample must be calculated using formula $\varepsilon(E) = \omega\varepsilon_0(E)$, finding the value of the coefficient ω for the relation (2).

For a cylindrical container l = H and for a complex-shaped container l = H − h.

The activity of the radionuclide, emitting γ rays with energy E_1, is calculated from the relation

$$A = F/T\eta\omega\varepsilon_0(E_1),$$

where A is the activity of the radionuclide in the sample in Bq; F is the area of the total absorption peak in counts; T is the duration of the measurements in sec; and η is the quantum yield of the radionuclide.

Compared with the method of calibration of the spectrometer based on the efficiency, which is proposed in [7] and recommended for wide application [8], the method described here is distinguished by its universality and lower labor intensiveness.

LITERATURE CITED

1. Ts. I. Bobovnikova, S. B. Iokhel'son, and V. N. Churkin, in: Apparatus and Methods for Studying Environmental Pollutants [in Russian], No. 2, Gidrometeoizdat, Leningrad (1970), p. 117.
2. Shielding of Nuclear Reactors [Russian translation], IL, Moscow (1958).
3. V. I. Parkhomenko, É. M. Krisyuk, and É. P. Lisachenko, Prib. Tekh. Eksp., No. 4, 46 (1983).
4. Handbook on Radiation Shielding for Engineers [in Russian], Atomizdat, Moscow (1973).

5. [an], Atomizdat, Moscow (1974).
6. V. P. Mashkovich, Shielding from Ionizing Radiation [in Russian], Énergoatomizdat, Moscow (1982).
7. G. G. Doroshenko et al., in: Problems of Ensuring Radiation Safety during Operation of Nuclear Power Plants [in Russian], Vol, 2, Prague (1976), p. 24.
8. Methodological Recommendations on Public-Health Monitoring of the Content of Radioactive Materials in Objects in the Environment [in Russian], Minzdrav SSSR, Moscow (1980).

ISOMERIC RATIOS OF THE YIELDS OF PHOTONUCLEAR REACTIONS FOR GAMMA-ACTIVATION ANALYSIS

M. G. Davydov, V. G. Magera,
A. V. Trukhov, and É. M. Shomurodov

UDC 543.0

The requirements for photonuclear data for γ-activation analysis are described in the review [1]. In this paper, the question of the needs, requirements, and means for providing data on the cross sections of photonuclear reactions with excitation of the isomeric states of nuclei for γ-activation analysis is examined in greater detail. Such reactions constitute ∿40% of all photonuclear reactions of interest for γ-activation analysis, including: (γ, n) — 14%, (γ, p) — 6%, (γ, 2n) — 5%, (γ, pn) — 12%.

The cross sections of photonuclear reactions ($\sigma_{\gamma,x}$) for γ-activation analysis are best represented in the form of Lorentz curves with the following parameters: half-width Γ; position of the maximum E_m; and cross section at the maximum σ_m. In addition, it is necessary to give the value of the energy threshold of the reaction E_n [1]. In our case, this means that it is necessary to obtain the values of the parameters of the cross sections for two reaction channels, corresponding to the formation of the final nucleus in the ground and metastable states. The thresholds of the reactions (γ, x) and (γ, x^m) differ by the value of the energy of the metstable state E_m, i.e., $E_n^m = E_n^g + E_m$.

It was previously established that with quite good accuracy the cross sections of the reaction channels studied in the region of the giant dipole resonance have a similar form: $E_m^m = E_m^g$ and $\Gamma^m = \Gamma^g$. If the cross section of the reaction (γ, x), measured, for example, by the methods of direct detection of the reaction products, is known, then it is sufficient to determine the so-called isomeric ratio of the cross sections $r(E_\gamma) = \sigma^m/\sigma^g$. It can be shown that this ratio for $E_\gamma > E_m + \Gamma$, to within a constant α practically equal to one, is equal to the isomeric ratio of the yields $d(E_{\gamma m})$ of the reaction (γ, x), corresponding to the formation of the final nucleus in the metastable and ground states:

$$d(E_{\gamma m}) \equiv \frac{Y_m}{Y_g} = \frac{\int_{E_n^m}^{E_{\gamma m}} \sigma^m(E_\gamma)\, W(E_\gamma, E_{\gamma m})\, dE_\gamma}{\int_{E_n^g}^{E_{\gamma m}} \sigma^g(E_\gamma)\, W(E_\gamma, E_{\gamma m})\, dE_\gamma} \cong \alpha r(E_\gamma).$$

Analogous results were obtained in [2-5]. In [4, 5] $d(E_{\gamma m})$ is determined with the help of the isomeric ratio of the cross sections $r(E_\gamma)$, weighted by the bremmstrahlung radiation spectrum, and in [3] the average photon energy $\bar{E}_\gamma$, with which the reaction occurs, is used to obtain the transition from $r(E_\gamma)$ to $d(E_{\gamma m})$.

The results of compilations, based on 40 works published before 1983, permit determining the completeness and quality of the data on $r(E_\gamma)$ and $d(E_{\gamma m})$ and facilitate the planning of the work for obtaining the missing data. The compilation did not include reactions as a result of which the number of nucleons in the nucleus changes by more than three. For γ-activation analysis, there is no particular reason for using the bremmstrahlung radiation with $E_{\gamma m} >$ 25-30 MeV. Due to the possible contribution of the direct processes, the values of $r(E_\gamma)$ and

Translated from Atomnaya Énergiya, Vol. 58, No. 1, pp. 47-50, January, 1985. Original article submitted February 13, 1984.

 0038-531X/85/5801-0056$09.50

dipole resonance of interest to us. For this reason, we included, as a rule, in the compilation the results of measurements of $r(E_\gamma)$ and $d(E_{\gamma m})$, obtained with $E_{\gamma m} \leqslant 30$ MeV.

The available experimental data are presented in publications in the most diverse form: $r(E_\gamma)$, $d(E_{\gamma m})$, $Y_m/(Y_m + Y_g)$, Y_h/Y_l (Y_h is the yield of the high-spin isomer; Y_l is the yield of the low-spin isomer). These primary data are rescaled to $r(E_\gamma)$ or $d(E_{\gamma m})$, which are used as the basic representations of the isomeric ratios.

Almost all of the first results, contained in publications in the 1950s and 1960s, were obtained with the help of scintillation spectrometers, and to calculate the isomeric ratios incomplete or inaccurate decay schemes of isomeric pairs were used. For this reason, the accuracy of these data is low, and the results of some works agree poorly with other known data. Kato [6], whose work was performed specially for γ-activation analysis, presents the isomeric ratios of the yields in the form $Y_m/(Y_m + Y_g)$ for 12 photonuclear reactions, which in some cases not only do not agree with the results of other works but are clearly contradictory — for two cases $Y_m/(Y_m + Y_g) > 1$. In recent years, the isomeric ratios of the cross sections of photonuclear reactions have been studied most actively by Bartsch's group [4], which can perform measurements for the short-lived states also. The largest number of measurements was performed for the isomers ^{58}Co, ^{44}Sc, ^{89}Zr (5-7 papers each, whose results, in general, agree within the limits of the measurement error. The remaining isomeric pairs were studied significantly less (1-3 papers each). The reaction (γ, n) was primarily studied (28 cases).

More or less reliable data on the isomeric ratios are available for a very small number of cases of activation of nuclei of interest for γ-activation analysis (13%). The experimental data were obtained for 21% of reactions (γ, n), for 13% of reactions (γ, 2n), 10% of reactions (γ, p) and 3% of reactions (γ, pn).

Approximations cannot be introduced for the parameters of cross sections as a function of N, Z, and A of nuclei in order to obtain $r(E_\gamma)$ because $r(E_\gamma)$ are to a large extent determined by the quantum characteristics of the metastable, ground, and all intermediate excited states of the nuclei, which do not have a systematic dependence on the number of nucleons in the nucleus.

The methods for calculating $r(E_\gamma)$, based on the statistical theory of nuclei, were first developed by Huizenga and Vanderboch [7, 8]. Usually, information on the parameter of the density of nuclear levels a and the parameter characterizing the spin-dependence of the density of states σ is obtained by comparing the computed and measured values of $ar(E_\gamma)$. In later works the Huizenga—Vanderboch formalism was improved by taking into account the parity of the levels, the pairing mechanism, and admixtures of quadrupole transitions in the γ cascade. Different models were used to describe the density of nuclear states: Fermi gas, independent pairing, and superconductivity. In some works attempts were made to take into account the contribution of the direct or preequilibrium processes within the framework of the preequilibrium statistical model. In order to perform concrete calculations a series of nuclear parameters, including primarily the parameters of the density of nuclear states, must be selected.

The most reliable, correct, and in many cases least laborious method for obtaining data on $r(E_\gamma)$ and $d(E_{\gamma m})$ is to measure these parameters directly. The fact that in the region of the giant dipole resonance $r(E_\gamma) = d(E_{\gamma m}) = \text{const}$ makes it possible to restrict the measurements at the first stage to measurements of $d(E_{\gamma m})$ with the same value of the energy $E_{\gamma m}$. This energy can be taken as $E_{\gamma m} = 22$ MeV, because in this case for most photonuclear reactions the condition $E_{\gamma m} \geq E_m + \Gamma$ holds and the contribution of direct processes cannot be especially important. Of course, in some cases there will be no similarity between $\sigma^m(E_\gamma)$ and $\sigma^g(E_\gamma)$ (experimental indications of this exist in the form of a nontrivial energy dependence of the isomeric ratios). For this reason, the data obtained for $E_{\gamma m} = 22$ MeV must be used with care.

The techniques used to measure the isomeric ratios of the yields are described in great detail in the literature, including in [9], and we shall consider only the methodological features of our measurements. In the measurements we used the well-known technique of direct pairing of measurements at the photo peaks of the γ lines, characteristic for the metastable and ground states, obtained from one γ spectrum (GS) of an activated sample, and the technique of decomposing the curve of the decay or accumulation, measured based on one γ line (RS). The accuracy of the measurements of $d(E_{\gamma m})$ by these methods (the error does not exceed 3-8%)

Reaction	d or r	$E_{\gamma m}$ or E_γ	Detector	Method	Source
$^{45}Sc(\gamma, n)^{44}Sc$	0,23±0,02	22	SFD	GS	This work
	0,21	30	SFD	GS	[6]
	0,23±0,03	—	—	—	[12]
	0,21±0,04	50	SS	—	[3]
	0,16±0,02	22	SS	RS	[13]
	0,19±0,02	36	SS	RS	[13]
	0,19±0,02	48	SS	RS	[13]
	0,28±0,08	—	—	—	[14]
	0,18±0,03	22	—	—	[15]
	0,21±0,02	30	—	—	[15]
	0,19±0,02	36	—	—	[15]
	0,19±0,02	48	—	—	[15]
$^{59}Co(\gamma, n)^{58}Co$	0,92±0,02	22	SFD	RS	This work
	0,82±0,03	30	SS	RS	[16]
	0,79±0,04	30	SS	RS	[17]
	1,33±0,09	48	SFD	RS	[18]
	1,33±0,05	35	SS	RS	[19]
	1,33±0,05	54	SS	RS	[19]
	0,8±0,1	—	SS	RS	[20]
	1,63±0,08	68	SS	RS	[21]
	0,85±0,04	150	SFD	RS	[22]
$^{82}Se(\gamma, n)^{81}Se$	0,54±0,03	22	SFD	GS	This work
	1,0±0,5	20	SS	RS	[23]
$^{74}Se(\gamma, n)^{73}Se$	0,10±0,02	22	SFD	GS	This work
	0,13±0,02	14,5	SFD	RS	[29]
$^{81}Br(\gamma, n)^{80}Br$	0,48±0,03	22	SFD	RS	This work
	0,40±0,02	25	—	—	[24]
	0,49±0,01	16	SS	—	[25]
	0,47±0,03	30	—	—	[17]

Reaction	d or r	$E_{\gamma m}$ or E_γ	Detector	Method	Source
$^{85}Rb(\gamma, n)^{84}Rb$	0,31±0,02	22	SS	GS	This work
	0,37±0,01	45	SFD	RS	[5]
	0,172	30	SFD	GS	[6]
$^{86}Sr(\gamma, n)^{85}Sr$	0,14±0,02	22	SS	GS	This work
	1,78±0,25	30	SS	GS	[17]
	2,0±0,4	—	SS	GS	[20]
	1,46±0,15	14,5	SFD	RS	[29]
$^{90}Zr(\gamma, n)^{89}Zr$	1,44±0,02	22	SFD	GS	This work
	0,61	30	SFD	GS	[6]
	1,58	> 17	—	—	[26]
	1,27±0,17	> 18	SS	GS	[27]
	1,0	> 18	SS	GS	[28]
	2,0±0,6	30	SFD	GS	[17]
	0,66±0,02	14,5	SFD	RS	[29]
$^{98}Mo(\gamma, p)^{97}Nb$	0,71±0,02	22	SFD	GS	This work
$^{116}Cd(\gamma, n)^{115}Cd$	0,12±0,02	22	SFD	GS	This work
	0,27	30	SFD	GS	[6]
	0,25	30	SS	GS	[17]
$^{112}Sn(\gamma, p)^{111}In$	0,044±0,001	22	SFD	GS	This work
$^{118}Sn(\gamma, p)^{117}In$	9,53±2,68	22	SFD	GS	This work

is much higher than with a separate measurement of the yields in the ground and isomeric states of the final nucleus (error of 20-30%) [19].

We activated the samples, prepared from porous materials (in the elemental form, in the form of oxides or porous salts) in the form of disks with a diameter of 35 mm and a mass of 10-15 g, in the beam of bremmstrahlung radiation of the B 25/30 betatron with $E_{\gamma m}$ = 22 MeV at a distance of 20 cm from the stopping target. The error of the values of $E_{\gamma m}$ presented does not exceed 0.2 MeV taking into account the possible drift of the energy scale of the beatron. We measured the γ spectra and the decay curves on the scintillation spectrometer with a 150 × 100 mm NaI(Tl) crystal (SS) or on a Ge(Li) spectrometer with a sensitive area of 13 cm^2 and a thickness of 1.15 cm (SFD). We calibrated the spectrometers with respect to the energy with the help of standard spectrometrical γ sources. The Ge(Li) spectrometer had a resolution of 2.2 keV for the 12-keV line and 2.9 keV for the 1332-keV line. We determined the areas of the photopeaks by the well-known Wasson method. We determined the ratio of the detection efficiencies of the Ge(Li) spectrometer $\varepsilon(E_\gamma)$ for γ lines with different energy with the help of the semiempirical Kane and Moriscatti relation $\ln \varepsilon = bx + cx^2$ [$x = \ln(a/E)$] [10], the coefficients for which are determined by the method of least squares from the results of additional measurements with the set of standard spectrometric γ sources. We interpreted the decay curves using a special program for the M-6000 computer or graphically. We selected the time conditions for the measurements for each isomeric pair taking into account its decay scheme. The data on the decay scheme, required for analysis of the measurements, are taken from tables [11]. We estimated the measurement errors starting from the statistics of the counts in the photopeaks, used for determining $d(E_{\gamma m})$. Separate measurements in a series of identical samples showed that the errors in the reproduci-

bility, do not exceed the statistical errors. The methodical errors were not estimated. In required cases, we checked the contribution of interfering reactions to the isomer yield by additional measurements. The values of $d(E_{\gamma m})$ were obtained for 12 photonuclear reactions (see Table 1).

Within the limits of the measurement error our result for the reaction $^{45}Sc(\gamma, n)^{44}Sc$ agrees with [3, 6, 12], is somewhat higher than the values given in [13, 15], and is lower than the values in [14], though it does not contradict the works cited.

The measurements for the reaction $^{59}Co(\gamma, n)^{58}Co$, obtained with $E_{\gamma m} \leqslant 30$ MeV from [16, 17, 20], agree well with one another and are lower than our value, obtained at $E_{\gamma m} = 22$ MeV. The remaining values were determined for $E_{\gamma m} > 30$ MeV and, as a rule, they are higher than our values. It should be noted that this reaction has not been adequately studied for $E_{\gamma m} \leq 30$ MeV. The isomeric ratios for the reactions $^{82}Se(\gamma, n)^{81}Se$ and $^{81}Br(\gamma, n)^{80}Br$ agree within the limits of error of the measurements. Our result for the reaction $^{85}Rb(\gamma, n)^{84}Rb$ agrees with the value obtained in [5], but differs substantially from the data in [6].

The significant difference between our results for the reaction $^{86}Sr(\gamma, n)^{85}Sr$ and the results in [17, 20, 29] requires a more detailed analysis and check, just as for the reaction $^{116}Cd(\gamma, n)^{115}Cd$. With the exception of the low values in [6, 28, 29], the measurements for the reaction $^{90}Zr(\gamma, n)^{89}Zr$ agree with one another to within the quite large measurement error.

We were the first to obtain the results for the reactions $^{98}Mo(\gamma, p)^{97}Nb$ and $^{112}Sn(\gamma, p)^{111}In$, $^{118}Sn(\gamma, p)^{117}In$.

Thus, due to the existence of perfected γ spectrometers and quite accurate information on the decay schemes, it is now possible to obtain with comparatively less effort experimetally more reliable and accurate data on the isomeric ratios of the cross sections (yields) of photonuclear reactions required for further progress in the area of γ-activation analysis.

LITERATURE CITED

1. M. G. Davydov, V. I. Kuksa, and A. P. Naumov, "Nuclear data for gamma-activation analysis," No. 2318-82, VINITI, Moscow (1982).
2. M. G. Davydov and V. A. Mantoptin, in: Abstracts of Reports at the 32nd Conference on Nuclear Spectroscopy and Nuclear Structure [in Russian], Nauka, Leningrad (1977), p. 239.
3. W. Walters and J. Hummel, Phys. Rev., 150, No. 3, 867 (1966).
4. H. Bartsch et al., Z. Phys., A285, No. 1, 71 (1978).
5. U. Kneissl et al., Nucl. Phys., A135, No. 2, 395 (1969).
6. T. Kato, J. Radioanal. Chem., 16, No. 1, 307 (1973).
7. J. Huizenga and R. Vandenboch, Phys. Rev., 120, 1305 (1960).
8. J. Huizenga and R. Vandenboch, Phys. Rev., 120, 1313 (1960).
9. L. Ya. Arifov et al., Izv. Akad. Nauk SSSR, Ser. Fiz., 42, No. 4, 831 (1978).
10. W. Kane et al., Nucl. Instrum. Method., 56, 189 (1967).
11. Tables of Isotopes, C. Lederer and V. Shirley(eds.), Wiley, New York (1978).
12. R. Volpel, Nucl. Phys., A182, 411 (1972).
13. J. Tatarezuk and H. Medicus, Phys. Rev., 143, No. 3, 818 (1966).
14. M. Erikson and G. Jonsson, Nucl. Phys., A242, 507 (1975).
15. S. Steinberg, in: B. S. Thesis, University of Illinois (1963).
16. P. Decowski et al., Nucl. Phys., A112, 513 (1968).
17. J. Carver, G. Coote, and T. Sherwood, Nucl. Phys., 37, 449 (1962).
18. C. Rhoades and H. Medicus, Phys. Rev., 167, No. 4, 1049 (1968).
19. H. Lichtblau and A. Goldman, Z. Phys., 205, 47 (1967).
20. L. Apers, P. Capron, and L. Gilly, J. Inorg. Nucl. Chem., 5, 23 (1957).
21. D. Christian and D. Martin, Iowa State College Report No. ISC-197 (1951).
22. E. A. Skakun et al., in: Abstracts of Reports at the 32nd Conference on Nuclear Spectroscopy and Nuclear Structure [in Russian], Nauka, Leningrad (1982), p. 565.
23. E. Silva and J. Goldemberg, Ann. Acad. Brasil. Sci., 28, No. 3, 275 (1956).
24. A. King and A. Voigt, Phys. Rev., 105, 1310 (1957).
25. L. Katz, L. Pease, and H. Moody, Can. J. Phys., 30, 476 (1952).
26. S. Costa et al., Nucl. Phys., 72, 158 (1965).
27. L. Katz, R. Baker, and R. Montalbetti, Can. J. Phys., 31, 250 (1953).
28. J. Fox, Ph. D. Thesis, University of Illinois (1960).
29. Fam Zui Khien, Ngo Kuang Zui, and Nguen Tak An', Yad. Fiz., 35, No. 2, 257-263 (1982).

POSSIBILITY OF DECREASING THE ENERGY DEPENDENCE OF DETECTORS BASED ON THE THERMAL LUMINOPHOR LiF IN THE X-RAY REGION

L. Z. Kalmykov, T. G. Kandel', S. M. Grinberg, and I. L. Kruglikov

UDC 621.386.92(088.8)

Lithium fluoride (LiF) plays a leading role among luminophors used in thermoluminescent dosimetry. This is a result of its many useful characteristics: high sensitivity and possibility of detecting different forms of radiation, wide range of measurable doses, good preservation of dosimetric information, possibility of its use in the single-crystalline and powdered forms as well as introduction into an organic matrix, etc. The effective atomic number of LiF is 8.14 and that of muscle tissue is 7.47. For this reason, based on the interaction with photon ionizing radiation, LiF is close to soft biological tissues. In the region of photon energies <100 keV, the energy dependence of LiF can attain 40-50%. As a result of this, LiF detectors are not suitable for direct measurements of doses of low-energy x-ray radiation absorbed in soft tissues as well as in fields with a significant contribution of low-energy photons.

This deficiency of LiF can be eliminated by using its finely dispersed mixture with other substances — nonluminophors. In such mixtures, the particle sizes of the components must be much smaller than the mean-free path length of secondary electrons with the lowest energies. Under these conditions, the dose absorbed in the particles of the thermoluminophor is determined by the electrons formed in the medium surrounding the particle, i.e., by the characteristics of the heterogeneous system as a whole. By selecting an additive material with low Z_{eff}, it is thereby possible to make LiF equivalent to tissues in the low-energy range of photon radiation.

For such substances, we used lithium carbonate Li_2CO_3 and bis(triethylammonium)dodecahydrododecaborane $[NH(C_2H_5)_3]_2B_{12}H_{12}$ [1, 2]. These substances are nonluminophors, they are stable in storage and when heated, they are transparent to the luminescence emission of LiF, and they are easily pulverized. The value of Z_{eff} for these substances is equal to 7.25 and 5.28, respectively.

Table 1 assesses the muscle-equivalence of dosimetric compositions with different content. The dosimetric equivalence is observed in the photon energy range where the ratio

$$A = \frac{(\mu_{en}/\rho)_{mix}}{(\mu_{en}/\rho)_{muscle}}$$

is equal to one. The value of K presented in Table 1 is equal to the ratio $A_{E_i}/A_{1250\ keV}$. As evident from Table 1, when 35% Li_2CO_3 is added to LiF, the composite material is muscle-equivalent in the range 10-60 keV (with an error of about ±5%) and has a lower energy-dependence than LiF in the rest of the energy range. For the two other compositions in the energy range presented μ_{en}/ρ is less than the corresponding values for muscle tissue by 7-13%. For this reason, strictly speaking, such composite materials are not muscle equivalent. However, the fact that K is constant and differs little from one indicates that in a wide energy range the absorbed doses in these composite materials and in muscle tissue are equal to within a constant coefficient close to one.

To determine experimentally the effect of the additive added to the thermal luminophor on the energy dependence, we studied the thermal luminescence of the mixtures LiF and Li_2CO_3 with different composition for four values of the energy of x-ray radiation (17, 26, 36, and 82 keV) and for γ rays from ^{60}Co. We used the powdered form of the LiF thermoluminophor with the natural isotopic composition and especially pure grade Li_2CO_3. The size of the particles of the components was <45 μm. We varied the mass fraction of LiF(p) in the range 0.3-1.0. Under irradiation, we placed 60 mg of the powder in a depression (∼2 mm) on the surface of a tissue-equivalent Miks-D cell (diameter 25 mm, height 7.5 mm). Under γ irradiation from

Translated from Atomnaya Énergiya, Vol. 58, No. 1, pp. 50-53, January, 1985. Original article submitted January 16, 1984.

 0038-531X/85/5801-0060$09.50

E_i, keV	Composition						LiF	
	65 % LiF + 35 % Li_2CO_3		35 % LiF + 65 % Li_2CO_3		75 % LiF + 27 % $[NH(C_2H_5)_3]_2B_{12}H_{12}$			
	A	K	A	K	A	K	A	K
10	1,04	1,21	0,926	1,06	0,933	1,06	1,17	1,39
20	1,03	1,20	0,913	1,05	0,925	1,05	1,16	1,38
30	1,01	1,18	0,903	1,04	0,917	1,04	1,15	1,37
40	0,984	1,15	0,892	1,03	0,905	1,02	1,09	1,30
60	0,934	1,09	0,884	1,02	0,904	1,02	0,990	1,18
80	0,892	1,04	0,876	1,01	0,892	1,01	0,908	1,08
100	0,874	1,02	0,874	1,00	0,891	1,01	0,874	1,04
200	0,863	1,01	0,873	1,00	0,890	1,01	0,853	1,01
500	0,859	1,00	0,872	1,00	0,881	1,00	0,844	1,00
1000	0,856	1,00	0,869	1,00	0,882	1,00	0,840	1,00
2000	0,860	1,00	0,872	1,00	0,899	1,02	0,844	1,00
5000	0,863	1,01	0,874	1,00	0,945	1,07	0,847	1,01

TABLE 2. Dependence of the Thermoluminescence of Mixtures of LiF and Li_2CO_3 on Their Composition

E_i, keV	$I = f(p)$	r	S_0	F_c	t_c
17	$1,59+12,08p$	0,9908	0,44	322,34	2,736
26	$0,85+16,01p$	0,9968	0,35	874,13	9,399
36	$1,71+15,69p$	0,9971	0,32	1029,23	8,854
82	$1,64+13,10p$	0,9973	0,23	1307,59	4,465
1250	$1,98+10,46p$	0,9833	0,51	175,25	—

Note. r) correlation coefficient; S_0) rms regression error in I; F_c) computed value of Fisher's F criterion; t_c) computed value of Student's t criterion.

TABLE 3. Effect of the Composition of Mixtures of LiF and Li_2CO_3 on the Energy Dependence of the Thermoluminescence

Mass fraction in the mixture (p)	K for E_i			
	17	26	36	82
1,0	1,10	1,35	1,40	1,18
0,9	1,09	1,34	1,39	1,18
0,8	1,09	1,32	1,38	1,17
0,7	1,08	1,30	1,36	1,16
0,6	1,07	1,27	1,35	1,15
0,5	1,06	1,23	1,32	1,13
0,4	1,04	1,18	1,29	1,11
0,3	1,02	1,10	1,25	1,09

^{60}Co, in order to create an electronic equilibrium, we covered the cell with a Miks-D cover 5 mm thick. The exposure dosage was the same in all experiments. We determined the thermoluminescence signal (I) on a measuring instrument by the peak method. Equivalent data for each value of the energy were analyzed by the method of regression analysis in order to find the dependence of I on p (Table 2).

As is evident from Table 2, $F_p > F_{table}$ ($F_{table} = 13.74$). Therefore, the presented regression equations adequately describe the experimental data. The correlation coefficient r indicates that there is a determinate dependence of the thermoluminescence signal on the composition of the mixture. When the presented regression equations are compared in pairs based on the Student's t criterion with the equation obtained for the ^{60}Co radiation, a significant difference is established for all energy values with the exception of 17 keV ($t_{table} = 2.969$ with $p = 0.01$). This gives a basis for calculating the value of the energy dependence for mixtures with different composition K (Table 3):

$$K_{E_i} = \frac{(a_0 + a_1 p)_{E_i}}{(a_0 + a_1 p)_{E_i = 1250\ \text{keV}}}.$$

Thus the use of materials with low Z_{eff} decreases the energy dependence of dosimetric composite materials containing the thermoluminophor LiF; in addition, K decreases as the content of these substances in the composite material increases.

An analysis of the values of K presented in Table 3 shows that they are somewhat higher than the computed data (see Table 1). Information on the experimentally obtained high values of the energy dependence of LiF and other thermoluminophors has been published [3-5]. This fact is explained by the influence of the scattered radiation from the material surrounding the detector and the fact that the real spectrum at the location of the detector was not taken into account. In particular, there exist data indicating that the thermoluminescence accom-

of the Components on the Energy Dependence of the Dosimetric Composite Material K with Respect to E_i = 1.25 MeV

Particle size, μm	17 keV	33 keV	82 keV
102–250	1,12±0,09	1,32±0,13	1,15±0,09
40–88	1,27±0,10	1,39±0,09	1,22±0,09
<40	1,25±0,08	1,28±0,09	1,11±0,07
<5	1,35±0,08	1,32±0,10	1,17±0,14

panying the action of monoenergetic radiation is 10-20% lower than that accompanying the action of filtered x-ray radiation [6].

In order to ensure that the particles are finely dispersed in the composite material, the particles must be quite small. The larger the difference between Z_{eff} of the components, the higher must be their degree of dispersity. Table 4 shows the effect of the particle sizes on the energy dependence of the mixture containing 73% LiF and 27% $[NH(C_2H_5)_3]_2B_{12}H_{12}$. It follows from the data presented that pulverization of the components of the composite material studied down to particles of size 100-200 μm, usually used in thermoluminescent dosimetry, is sufficient for achieving fine-dispersity of the dosimetric system. This result is also valid for mixtures of LiF and Li_2CO_3, since Z_{eff} of these materials are close.

Using the methods of mathematical planning of the experiment, we studied some dosimetric properties of composite thermoluminescence detectors. Thus, we studied the dependence of the thermoluminescence (y) on the dose, the mass of powder, the diameter of the sample used in measurements of the thermoluminescence, and the content of Li_2CO_3 in the mixture with LiF (Table 5). The equation which relates the thermoluminescence of the powder detector with the variable factors has the form

$$y = 1.022 + 0.643x_1 - 0.176x_2 + 0.049x_3 + 0.073x_4.$$

An analysis of this expression shows that in the range 3-214 kC/kg the thermoluminescence signal depends linearly on the dose. As is evident from the values of the coefficients in the regression equation in front of the factors x_3 and x_4, as the mass of the powder detector increases from 18.5 to 35.5 mg, and the diameter of the suhstrate on which it is positioned in the measurements in the range 5.1-8.5 mm, the thermoluminescence increases insignificantly. At the same time, however, the diameter of the detector had a more distinct effect. The indicated information is important for optimizing the mass and size of thermoluminescence detectors. An increase of the mass fraction of Li_2CO_3 in the dosimetric composite material decreases the sensitivity to radiation by a factor of 2.25 when the Li_2CO_3 content is increased from 0.35 to 0.65.

Detectors fabricated from mixtures of LiF and Li_2CO_3 can be used only in the powder form. The mixture of LiF and $[NH(C_2H_5)_3]_2B_{12}H_{12}$ can also be pressed into tablets. The mechanical strength of the tablets under a pressure of 14.7 MPa is equal to 1 kg, which is sufficient for the use of such detectors in phantom measurements.

Mixtures of LiF with Li_2CO_3, due to the high thermal stability of the latter, can be used for dosimetric measurements repeatedly with subsequent heat treatment under the conditions used for pure LiF. The noted 1.5-2-fold decrease in the sensitivity with a total dose of 200 Gr and 30 irradiation–measurement–heat-treatment cycles is in all probability associated with the pulverization of the powder of the thermoluminophor.

The results obtained in this work indicate that the energy dependence of the thermoluminophor LiF for photon energies in the range <100 keV can be decreased by creating its finely dispersed compositions with materials which are not luminophors and which have a low effective atomic number. Detectors based on these dosimetric materials can be used for direct measurements of the absorbed dose in soft tissues without making corrections for the tissue-nonequivalence, which simplifies such measurements and decreases their error. The composition-material detectors preserve the form of the thermal luminescence curve and the basic advantages of LiF. They can be fabricated under laboratory conditions.

TABLE 3. Level of Variation of the Factors in the Central Composite Orthogonal Plane (CCOP)

Factors	Unit of measurement	Coded units					Δ
		$-\alpha$	-1	0	$+1$	$+\alpha$	
x_1 — dose	lg D (D in P)	1,080	1,350	2,000	2,650	2,920	0,650
x_2 — quantity	Mass fraction of Li_2CO_3	0,238	0,30	0,45	0,60	0,662	0,15
x_3 — mass	mg	18,5	21,0	27,0	33,0	35,5	6,0
x_4 — diameter	mm	5,1	5,6	6,8	8,0	8,5	1,2

The approach presented in this paper to the modification of energy dependence of dosimetric systems, based on the creation of finely dispersed mixtures containing the thermoluminophor, can be used to obtain dosimetric systems which are equivalent to different irradiated media.

LITERATURE CITED

1. L. Z. Kalmykov and T. G. Kandel', "Material for thermal luminescence dosimetry of photon radiation in muscle tissue," Inventor's Certificate No. 8435060, Byull. Izobret., No. 12, 290 (1982).
2. L. Z. Kalmykov, T. G. Kandel', and R. A. Svitsyn, "Material for thermal luminescence dosimetry of photon radiation in muscle tissue," Inventor's Certificate No. 1065796, Byull. Izobret., No. 1, 178 (1984).
3. C. Graham and S. Homann, in: Proc. Int. Symp. "National and International Standardization of Radiation Dosimetry," Vol. 2, Vienna (1978), p. 335.
4. E. Storm, J. Cortez, and G. Littlejohn, in: Proc. Int. Symp. "National and International Standardization of Radiation Dosimetry," Vol. 1, Vienna (1978), p. 399.
5. T. Budd, M. Marshall, L. Peaple, and J. Dauglas, Phys. Med. Biol., 24, No. 1, 71 (1979).
6. P. Christensen, Lars Botter-Jensen, and Benny Majborn, "The response of thermoluminescence dosimeters to monoenergetic photons of energies between 15 keV to 100 keV," Dan. AEC Research Establishment Riso, Riso-M-1787, Health Physics Dep., Roskilde (1975).

EFFECT OF INTRAGRAIN PORES ON THE SWELLING OF UO_2

A. S. Gontar', R. Ya. Kucherov,
and M. V. Nelidov

UDC 621.039.548.34

It is well known that in highly compressed UO_2 pellets, almost all the pores are sealed [1]. In the final stage of sintering, effected in a gaseous medium, the pores which have been formed are in equilibrium, i.e., the gas pressure in them is compensated by the Laplace pressure, and, as a result of this, shrinkage of the pellets ceases [2-4]. These sealed pores are located at the boundaries and in the body of the grains in accordance with the distribution achieved at the final stage of sintering. In this case, the size of a considerable part of the pores in the body of the grains is <1 μm [5].

These facts allow one to conclude that at a high temperature in reactor conditions, additional swelling accompanies the radiation swelling of UO_2, caused by fusion of the equilibrium technological pores filled with gas, which migrate under the action of the temperature gradient.

The rate of migration of pores of these sizes (d_p < 1 μm), in the absence of increase of UO_2 grains, is controlled by a surface diffusion mechanism and is determined by the formula [4]:

$$V_s = \frac{6D_sQ_sa_0}{kT^2d_p}\operatorname{grad} T, \tag{1}$$

where D_s is the coefficient of surface self-diffusion of the atoms; Q_s is the heat of transfer for surface thermal self-diffusion; d_p is the diameter of a pore; a_o is the lattice constant; k is Boltzman's constant; T is the temperature.

As a result of direct motion, these pores in the course of time leave the grain boundaries where they are fixed under the action of the forces of the intergrain surface tension γ_b. Because of this, buildup, fusion, and increase of size of the original technological pores entering from the body of the grains will take place at the boundaries.

The size of the pore d_p, formed by the fusion of two colliding equilibrium pores filled with gas with diameters d_{p_1} and d_{p_2}, is determined from the solution of the equations of state of the gas in the pores and the condition of their equilibrium [2]:

$$d_p^2 = d_p^2 + d_{p_2}^2. \tag{2}$$

In this case, the volume of the pore formed exceeds the volumes of the fused pores, i.e., a reduction of density of the fuel occurs — its swelling.

Since the driving force acting on the pore, caused by the temperature gradient, increases with increase in size of the pore according to law [4]

$$F_b = \frac{\pi d_p^3 Q_s}{4a_0^3T}\operatorname{grad} T, \tag{3}$$

and the maximum value of the force restraining the pore at the boundary of the grain is equal to

$$F = \pi d_p \gamma_b /2, \tag{4}$$

then in attaining the critical size

$$d_p^{cr} \geqslant 2\left[\frac{a_0^3\gamma_b T}{2Q_s\operatorname{grad} T}\right]^{1/2} \tag{5}$$

the pore is torn away from the boundary of the grain and migrates towards the center of the fuel core.

The relations given allow the swelling of a UO_2 pellet to be estimated in reactor conditions in consequence of the fusion of the technological intragrain pores. For a quantita-

Translated from Atomnaya Énergiya, Vol. 58, No. 1, pp. 54-55, January, 1985. Original article submitted September 8, 1983.

 0038-531X/85/5801-0064$09.50

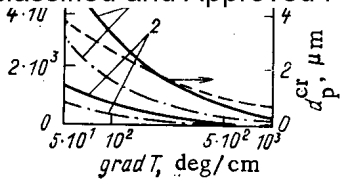

Fig. 1

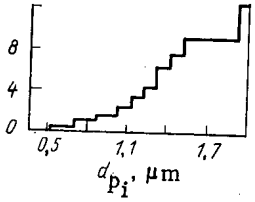

Fig. 2

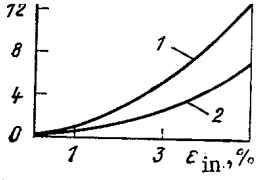

Fig. 3

Fig. 1. Values of the time necessary for displacement of pores with diameter d_p = 1 μm (——) and d_p = 0.5 μm (-·-) to a distance equal to the grain size, and the dependence of the critical diameter of pore (- - -) on the temperature gradient: 1) T = 1800°K; 2) T = 1900°K.

Fig. 2. Contribution of pores with diameter less than d_{pi} to the grain boundary porosity ε_i (initial intragrain porosity 5%, diameter of the original intragrain pores 0.5 μm).

Fig. 3. Effect of the initial intragrain porosity on the grain-boundary porosity formed after the exit of all intragrain pores at the grain boundary: 1) d_p = 0.5 μm; 2) d_p = 1 μm.

tive estimate of the effect, we shall confine ourselves to the temperature region below 2000°K, where there is no change of structure of the UO_2. As, in this temperature region, attachment and buildup of the migratory pores occurs at the grain boundaries [6], in the analysis we shall consider these boundaries as sinks for the technological pores ($d_p < 1$ μm).

For a quantitative estimate of the effect, we shall approximate an equiaxial grain to a cube of the same volume, one of the edges of which is perpendicular to the direction of the temperature gradient. The location of the pores subsequently arriving at this edge of the approximating cube will be determined by the Monte Carlo method. In the case of bridging of two pores, we shall find the location of the pores from the condition of conservation of the position of the center of mass for a system of two pores.

When performing the evaluating parametric calculations, we shall assume the grain size to be equal to 6 μm and the ranges of change of size of the original technological pores and the total porosity to be equal to 0.5-1 μm and 1-5%, respectively. For simplicity, we shall suppose that in the initial state there is no grain-boundary porosity. We shall choose the numerical values of the constants in Eqs. (1) and (5) in accordance with [4].

Figure 1 shows the values of the time necessary for displacing the pores to a distance equal to the size of a grain at 1800-1900°K and with a different temperature gradient in the UO_2. Here, the dependence of the critical pore diameter on the temperature gradient is shown. As the temperature depends only slightly on d_p^{cr}, this dependence is shown only for 1800°K. It can be seen that in the temperature conditions realized in many types of reactors, and to a lesser degree in individual zones of the UO_2 fuel core, the intragrain pores leave the grain boundaries in the initial period of irradiation, and the critical size of the pores at the boundaries can exceed the size of the original intragrain pores by a factor of several, which creates the necessary prerequisites for the development of the swelling mechanism considered.

The values of the porosity ε_i due to the presence of pores with a size less than d_{pi}, obtained after the exit of all the intragrain pores at the boundary, are shown in Fig. 2 for typical starting parameters. From a comparison of the sizes of these pores with the critical sizes (see Fig. 1) it follows that in realistic conditions over the radius of the fuel element both the case when all the pores or a considerable part of them remain at the grain boundaries and the case when part of these pores, having been torn away from the boundaries, migrates towards the center of the core, where in consequence of a reduction of the temperature gradient the critical size of the pore increases, as a result of which in this region the conditions are also created for the development of the additional swelling mechanism considered, are realized. Figure 3 shows the ratio of the initial and final porosity after fusion of the original pores, having different sizes.

An analysis was also carried out of the effect of the initial grain-boundary pores on the process being considered, which showed that with a given total number of the original pores, swelling of the fuel increases in proportion with increase of the ratio of the number

of p
aries.

The estimates given confirm that in the conditions causing migration of the pores, the presence of a technological intragrain porosity in high-density UO_2 can have a negative effect on the dimensional stability of the fuel core, leading to an appreciable additional swelling of a nonradiation nature.

LITERATURE CITED

1. G. H. Chelder, N. F. Bright, D. L. Paterson, and L. K. Watson, "Manufacture and properites of uranium dioxide fuel," in: Proceedings of the Second International Conference on the Peaceful Uses of Atomic Energy. Selected Reports of Foreign Scientists. Vol. 6. Nuclear Fuel and Reactor Materials, Main Administration of the Use of Atomic Energy for the Council of Ministers of the SSSR, Moscow (1959), pp. 627-648.
2. Ya. E. Geguzin and M. A. Krivoglaz, Motion of Macroscopic Inclusions in Solids [in Russian], Metallurgiya, Moscow (1971).
3. Ya. E. Geguzin, Physics of Sintering [in Russian], Nauka, Moscow (1967).
4. D. Olander, Fundamental Aspects of Nuclear Reactor Fuel Elements, Department of Nuclear Engineering, University of California, Berkeley (1976).
5. R. B. Kotel'nikov, S. N. Bashlykov, A. N. Kashtanov, and T. S. Men'shikova, High-Temperature Nuclear Fuel [in Russian], Atomizdat, Moscow (1978).
6. C. Ronchi and H. Matzke, "Calculations on the in-pile behavior of fission gas in oxide fuels," J. Nucl. Mater., 45, No. 1, 15-28 (1972).

STUDY OF THE CONDITIONS OF ACTIVATION WITH A RADIONUCLIDE NEUTRON SOURCE BASED ON ^{252}Cf

V. N. Kustov and V. V. Ivanenko

UDC 543.53

Activation setups with radionuclide neutron sources based on ^{252}Cf, Sb—Be are being increasingly used to solve scientific and commercial problems involving high-sensitivity neutron-activation analysis (NAA) of a wide range of objects containing gold, silver, uranium, rare-earth and other elements [1-6]. Commercial application of the indicated setups is most efficient in laboratories which are located directly in the regions where the prospecting and development of new deposits, including also gold-bearing ores, occurs. In the latter case, the structure of the NAA setup must ensure quite high capacity (up to 100 samples per day) and an accuracy of analysis with a threshold of 0.1-0.3 g/ton for gold determination. For neutron sources with an output of 10^9-10^{10} sec^{-1}, the indicated parameters can be attained when the flux density of thermal neutrons in the activation zone reaches 10^7 $sec^{-1} \cdot cm^{-2}$. The solution of this problem requires a well-founded approach to the selection of the structural materials of the activation zone and primarily the moderating material.

The distribution of thermal and resonant neutrons from point and extended sectioned californium sources in a water medium was studied in [7] and the deviations from the indicated distributions, arising due to the finite dimensions of the moderator, were studied in [8]. The characteristics of water and graphite moderators for ^{252}Cf were studied in [9]. In all indicated publications, the moderating medium was considered to be homogeneous and the perturbations introduced by the objects studied were ignored.

We studied the spatial distribution of thermal and resonance neutrons in different types of moderators by the method of the cadmium difference in the activation of gold foils, arranged radially at different distances from the source. The studies were performed on a modified (compared with the previously described [1]) setup admitting simultaneous irradiation of 96 samples each with a mass of 150-200 g in 16 channels (Fig. 1). We placed the radionuclide source ^{252}Cf with a neutron yield of $4 \cdot 10^9$ sec^{-1} in the central channel of a 25 × 30 × 50 cm moderating block. Without loading up the block with the samples, in homogeneous hydrogen-containing moderators the positions and values of the peaks in the

Translated from Atomnaya Énergiya, Vol. 58, No. 1, pp. 55-57, January, 1985. Original article submitted July 4, 1984.

 0038-531X/85/5801-0066$09.50

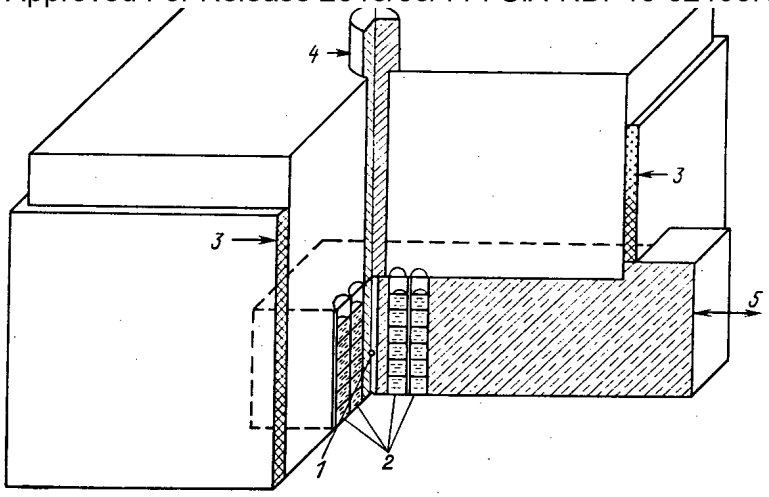

Fig. 1. Diagram of activation setup: 1) californium source; 2) channels with samples; 3) lead shield; 4) mechanism for lifting source; 5) movable truck.

distribution of thermal and resonance neutrons over the spherical layers (Fig. 2) agree with the computed and experimental data in [7-9], obtained for spontaneous-fission sources in media whose dimensions substantially exceeded the neutron-moderation length. Qualitative agreement is also observed for graphite, though in this case the influence of boundary effects, owing to the inadequate dimensions of the block compared with the neutron-moderation length in it, becomes important.

It follows from the data presented that in a sphere with a radius of up to 10-15 cm hydrogen-containing materials provide a higher density of thermal and resonant neutrons. Not less than 100 samples with a mass of 5-10 g each can be irradiated simultaneously in an activation zone of this size. The perturbation of the spatial distribution of neutrons when samples of the indicated mass are inserted turns out to be insignificant compared with the experimental random errors in the determination of the neutron flux density. The organic-glass moderator provides, in this case, a maximum neutron density.

When analyzing samples with coarsely dispersed gold or pulverized samples with diameter of up to 1 mm, in order to preserve the representativeness of the weighed quantity of sample its mass must be increased up to 100-200 g according to the well-known Richardson–Chechota formula [10]. In this case, the samples can be placed into the same activation zone with a radius of 15 cm in vertical channels, arranged around the neutron source. The role of the perturbation of the neutron distributions under these conditions, however, becomes determining, because the mass of the inserted material (10-15 kg) can even exceed the mass of the moderating material. The curves in Fig. 3 characterize the spatial distribution of thermal (see Fig. 3a) and resonant (see Fig. 3b) neutrons in the activation zone when only the sample being activated (1) is loaded into it, i.e., without the moderating material, and when additional graphite (2) and hydrogen-containing (3) moderators are introduced. It follows from the experimental data that if the graphite moderator increases the flux density of thermal neutrons by a factor of 1.3-1.5, while the resonance flux is approximately doubled, then with a hydrogen-containing moderator the neutron flux density increases by a factor of 10 and 3-15, respectively. Such a marked increase in the neutron flux density accompanying the use of the organic-glass moderator indicates the determining role of the mass of the organic glass as compared with the mass of the sample in the formation of the spatial distributions of the neutrons. The graphite moderator, as follows from the data presented, affects the characteristics of the neutron fields less strongly in the activation zone studied. In this connection, possible variations of the composition of the matrix and, therefore, the effects of perturbations, arising due to these changes, will affect the spatial distributions of neutrons in the hydrogen-containing moderator much more weakly than in graphite. The organic glass, in this case, is the most effective moderating material.

An experimental check of the role of the perturbation effects was made for different gold-bearing deposits. We measured the flux density of thermal and resonant neutrons with successive loading of the setup by samples from each deposit (see Table 1). A statistical

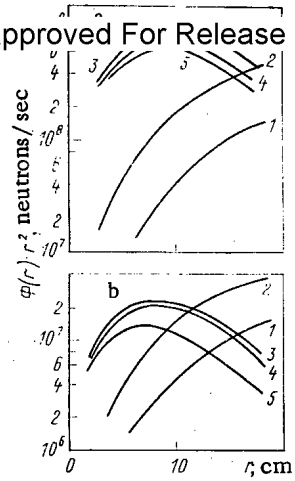

Fig. 2

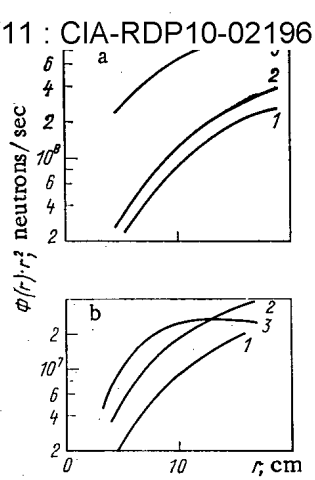

Fig. 3

Fig. 2. Distribution of thermal (a) and resonance (b) neutrons in uniform materials (without loading of samples): 1) without moderator; 2) graphite; 3) organic glass; 4) water; 5) paraffin.

Fig. 3. Distribution of thermal (a) and resonant (b) neutrons in the block with the samples: 1) without moderator; 2) graphite; 3) organic glass.

analysis of the experimental results by Duncan's method [11] shows that the 3-4% change recorded in the neutron flux density is insignificant compared to the random errors in the measurements of these quantities. The experimental confirmation of the stability of the neutron flux density enabled the determination of the value of the specific activity of gold in the zone of maximum neutron density $q_{max} = (1.16 \pm 0.02)\cdot 10^6$ counts$\cdot$min$^{-1}\cdot$g^{-1}. A knowledge of the corresponding quantities in the entire activation zone enabled the development of the NAA procedure, which excludes the need for using accompanying standards, which greatly simplified the conditions of mass analysis.

Much more important are the effects of perturbations arising due to the change in the geometrical conditions of activation, for example, with incomplete loading of the channels in the zone. It was shown experimentally that the specific activity of the control specimen in the channel can drop by up to 10% in the absence of neighboring samples in this channel. An additional extraction of samples from neighboring channels lowers the specific activity of the control sample by another 8%. To avoid this source of error, the analytical procedure allows for performing the NAA with total loading up of all channels with the help of ballasting samples.

The results of the studies performed and of methodological developments were realized in structures of setups and the procedure of NAA, whose metrological parameters correspond to the requirements adopted by Mingeo SSSR for analytical methods of category III, i.e., methods intended for mass analysis of ores from gold-bearing deposits. Experience with commercial tests and operation of setups over a long time, as well as the use of the NAA procedures under laboratory and expedition conditions, confirmed the high efficiency and commercial value of their application in prospecting and developing gold-bearing deposits.

TABLE 1. Density of Neutron Fields in the Activation Zone, sec$^{-1}\cdot$ cm^{-2}

Deposit	Thermal neutrons	Resonant neutrons
A	(9,3±0,86) 10^6	(4,3±0,27) 10^5
B	(9,7±0,82) 10^6	(3,9±0,25) 10^5
C	(9,3±0,82) 10^6	(3,9±0,25) 10^5
D	(8,9±0,83) 10^6	(4,1±0,26) 10^5
E	(9,3±0,73) 10^6	(4,1±0,26) 10^5
F	(8,9±0,71) 10^6	(4,0±0,19) 10^5

1. V. V. Ivanenko, V. N. Kustov, and V. V. Zheleznov, "Setup and method of neutron-activation analysis based on californium 252," Izotopy SSSR, 60, 3-9 (1981).
2. N. Shilo et al., "Instrumental neutron activation of gold in mineral raw materials using a californium neutron source," J. Radioanal. Chem., 79, No. 2, 309-316 (1983).
3. Yu. N. Burmistenko, Yu. S. Zamyatin, and Yu. G. Teterev, "Setup for neutron-activation analysis with an intense antimony–beryllium source of neutrons," Preprint Joint Institute of Nuclear Research, 18-81-171, Dubna (1981).
4. A. A. Kist et al., in: "Use of a californium source for analytical purposes," in: Activation Analysis in Science and Engineering, Affiliate of the Academy of Sciences of the USSR, Tashkent (1980), pp. 91-113.
5. N. A. Shilo et al., Abstracts of the 12th Mendeleev Conference [in Russian], Nauka, Moscow (1981), pp. 330-331.
6. V. V. Ivanenko, V. N. Kustov, and V. V. Kovalenko, "Instrumental neutron-activation analysis of samples of gold deposits in the Far East," in: Abstracts of Reports at the Conference on the Chemistry, Technology, and Analysis of Gold and Silver, Siberian Branch, Academy of Sciences of the USSR, Novosibirsk (1983), p. 72.
7. V. D. Gavrilov, Yu. S. Zamyatnin, and V. V. Ivanenko, "Accumulation of ^{252}Cf in the central channel of the SM-2 reactor," At. Energ., 35, No. 1, 33-35 (1973).
8. G. A. Tovstogan' and N. D. Tyufyakov, "Effect of the dimensions of the moderator and of the energy spectrum of neutrons from isotopic sources on the distribution of the flux density of hypocadmium neutrons in water," in: Radiation Technology [in Russian], No. 17, Atomizdat, Moscow (1979), pp. 212-216.
9. V. Ya. Vyropaev, "Use of isotopic neutron sources in activation analysis," Preprint Joint Institute of Nuclear Research, 14-9615, Dubna (1976).
10. Sample Extraction and Analysis of Noble Metals [in Russian], Metallurgiya, Moscow (1968), p. 20.
11. K. Doerfel', Statistics in Analytical Chemistry [Russian translation], Mir, Moscow (1969), p. 168.

DETERMINATION OF THE QUANTITY OF TRITIUM FORMED IN THE COOLANT OF WATER-COOLED–WATER-MODERATED REACTORS

S. V. Popov, A. G. Babenko, B. N. Mekhedov, V. M. Ilyasov, I. G. Golubchikova, and L. E. Podporinova

UDC 621.039.524.44

The sources of tritium in water-cooled–water-moderated reactors (VVÉR) have been studied theoretically in great detail [1, 2]. Experimental data on the concentration of tritium in the coolant are presented and an attempt is made to construct a mathematical model that describes the accumulation and migration of tritium in water systems of nuclear power plants in [2, 3]. The comparison of the computed and experimental values, however, is only approximate, because water-transfer parameters which are averaged over a long time interval are used, which leads to an appreciable disagreement between the experimental and theoretical results, especially at the end of the operating period.

In this connection, a mathematical model which enables the determination of the amount of tritium formed in the coolant of VVÉR-1000 with an acceptable error was constructed based on the experimental data on the concentration of tritium in the coolant of the first loop and in the makeup system as well as data on the daily consumption of water for makeup in the first loop.

The change in the tritium concentration $C_T(t)$ in the coolant of the first loop is described by a differential equation of the type

$$P_L \frac{dC_T(t)}{dt} = v_{fm}(t) + C_m(t) u_m(t) - C_T(t) v_l(t) - \lambda P_L C_T(t), \quad (1)$$

Translated from Atomnaya Énergiya, Vol. 58, No. 1, pp. 57-59, January, 1985. Original article submitted December 28, 1983.

0038-531X/85/5801-0069$09.50

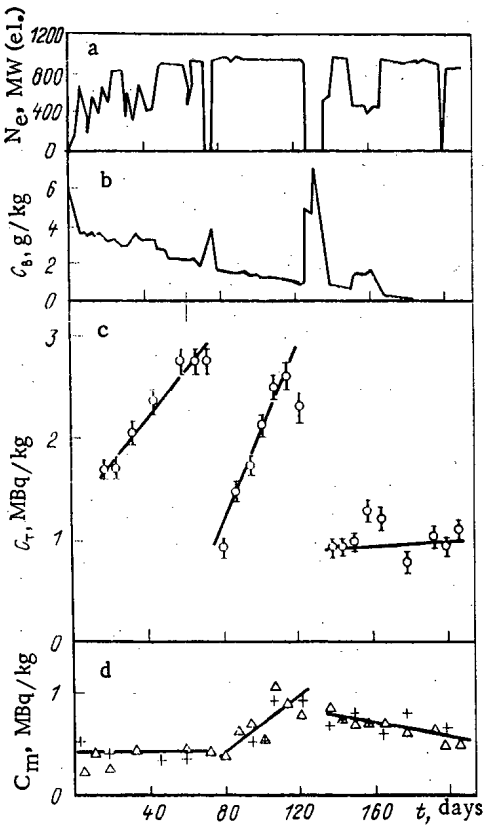

Fig. 1

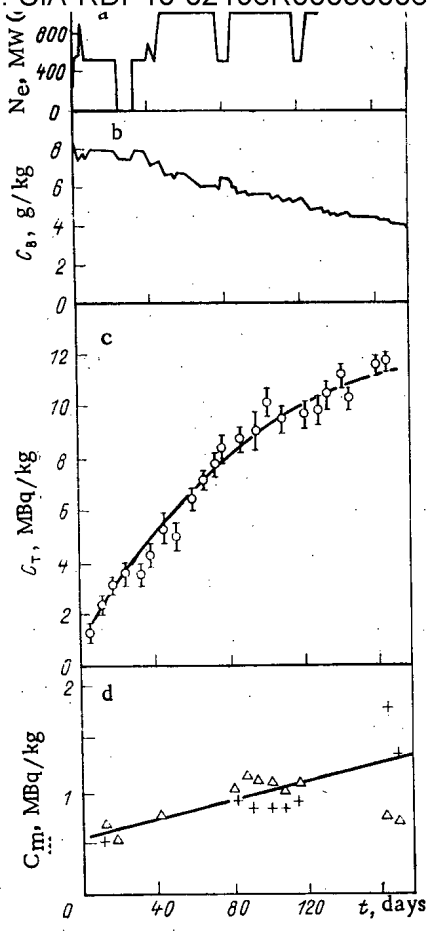

Fig. 2

Fig. 1. Change in the reactor power (a), H_3BO_3 concentration (b), tritium concentration in the first loop (c) and in the tanks of pure condensate (d) in B9 (+) and B10 (Δ), respectively, for the third operating period of the fifth block of NVAÉS as a function of time.

Fig. 2. Change in the reactor power (a), H_3BO_3 concentration (b), tritium concentration in the first loop (c) and in the tanks of pure condensate (d) in B9 (+) and B10 (Δ) as a function of time, respectively, for the fourth operating period of the fifth block of NVAÉS: ○) experimental values; ——) the least-squares curve approximating the experimental data.

where P_L is the mass fo the water in the first loop; $v_{fm}(t)$ is the rate of formation of tritium in the coolant; $C_m(t)$ is the concentration of tritium in the makeup water; $v_m(t)$ and $v_\zeta(t)$ are the flow rate of coolant for makeup of the first loop and leakage from it; and λ is the decay constant of tritium.

In view of the fact that the water level in the first loop is maintained constant, the equality $v_m(t) = v_\zeta(t)$ holds. Then the amount of tritium A_T, formed over a time τ, will be equal to

$$A_T = \int_0^\tau v_{fm}(t)dt = \int_0^\tau \left\{P_L \frac{dC_T(t)}{dt} + v_m(t)[C_T(t) - C_m(t)] + \lambda P_L C_T(t)\right\} dt = P_L[C_T(\tau) - C_T(0)] + \int_0^\tau v_m(t)[C_T(t) - C_m(t)]\,dt + \lambda P_L \int_0^\tau C_T(t)dt. \quad (2)$$

Therefore, to calculate A_T it is necessary to know the dependence of the tritium concentration in the water of the first loop and in the makeup water on time as well as the consumption of water for makeup in the first loop.

Periodic makeup in the first loop in the nominal operational regime of the reactor is performed, as a rule, with pure condensate, introduced in order to maintain the required

conce ... In addition, boron concentrate and solutions of chemical reagents (KOH, NH_4OH, N_2H_4) are introduced into the first loop. The latter are prepared in water taken from tanks containing the pure condensate. The pure condensate and the solutions of chemical reagents are introduced over a definite period of time Δt_i by special pumps with a capacity of Q_α. Thus the makeup flow rate is equal to

$$v_{m_i} = \sum_{\alpha=1}^{n} Q_{i\alpha}, \tag{3}$$

where n is the number of simultaneously operating pumps in the i-th time interval.

The dependence of $C_T(t)$ and $C_m(t)$ versus time is, as a rule, smooth [2]. For this reason, a curve of the following form can be drawn through the experimental points:

$$C(t) = \sum_{j=0}^{N} b_i P_i(t), \tag{4}$$

where $P_j(t)$ are the orthogonal Chebyshev polynomials; b_j are independent expansion coefficients; and N is the maximum degree of the polynomial. The coefficients b_j can be found by the method of least squares [4]. Substituting expressions (3) and (4) into Eq. (2), we obtain

$$A_T = P_L [C_T(\tau) - C_T(0)] + \int_0^\tau \sum_{\alpha=1}^{n} Q_{i\alpha}\Delta t_i \left[\sum_{j=0}^{N} b_i P_j(t) - \sum_{j=0}^{N_1} b'_j P_i(t)\right] dt + \lambda P_L \sum_{j=0}^{N} b_i \int_0^\tau P_j(t)dt. \tag{5}$$

The integrals in these expressions can now be easily found analytically.

Using formula (5) and the actual data, we calculated the amount of tritium formed in the coolant of the first loop of VVÉR-1000 in the fifth block of NVAÉS (Novovoronezhk Nuclear Power Plant) within the third and part of the fourth operating periods (from December 5, 1981 to December 20, 1982).

Figures 1 and 2 show the change as a function of time in the concentration of tritium in the water of the first loop and in the tanks of pure condensate used for makeup (B9, B10). The figures also show the change as a function of time in the reactor power and the concentration of boric acid in the coolant of the first loop. We determined the tritium concentration in the samples by a scintillation method using the SBS-2 setup. We first removed extraneous radionuclides from each sample by means of double distillation and performed no less than four measurements.

It follows from Fig. 1 that there were two prolonged shutdowns of the reactor during the third operating period. For this reason, the entire period was divided into three intervals, for each of which experimental data on the concentration of tritium in the coolant of the first loop and in the water in the tanks of pure condensate were described by their own curve (see Fig. 1c and d). In the fourth operating period, all experimental points $C_T(t)$ were described by a single curve — a parabola, and $C_m(t)$ was described by a straight line (see Fig. 2c and d).

As a result of the calculations it was found that A_T is equal to 2.7 ± 0.3 TBq and 4.3 ± 0.2 TBq for the third and fourth operating periods, respectively. To determine the computational error in A_T, the following formula was used:

$$(\Delta A_T)^2 = \sum_{i=1}^{i=L} \left(\frac{\partial A_T}{\partial x_i}\Delta x_i\right)^2, \tag{6}$$

where x_i denotes the independent coefficients b_j, b'_j, and $Q_{i\alpha}$. The calculation of the error in A_T was performed with a confidence probability of 0.95.

To clarify the contribution of the reaction $^{10}B(n, 2\alpha)^3H$ to the overall tritium activity of the coolant, the amount of tritium formed was calculated using the procedure in [3]. The values used for the H_3BO_3 concentration in the coolant of the first loop and the reactor power were obtained by operational control (see Fig. 1a, b; Fig. 2a, b).

For the third and fourth operating periods, the contribution of the indicated reaction according to the calculations is equal to 2.5 TBq and 5.0 TBq, respectively. These values differ from A_T by not more than 15%. Therefore, during the operating periods studied, tritium

was insignificant, which agrees with the results of [3]. The contribution of the reaction $^6Li(n, \alpha)^3H$ turned out to be small due to the fact that in the third operating period KOH was not introduced, i.e., the lithium impurity also did not enter. The partial overloading of the filter permitted introducing only 5 kg of KOH instead of the planned 40 kg during the fourth operating period.

Thus in this work we proposed a mathematical model for calculating the amount of tritium formed in the coolant of the first loop of VVÉR. A comparison of the amounts of tritium calculated for the first loop of the fifth block of NVAÉS based on the proposed model and based on the procedure published in [3], taking into account only the reaction $^{10}B(n, 2\alpha)^3H$, showed that these values differ by not more than 15%.

In conclusion, we thank V. V. Tagirov and V. N. Kuklin for useful discussions.

LITERATURE CITED

1. K. Langeker and H. Graupe, Kernenergie, 15, No. 165 (1972).
2. L. I. Golubev, V. M. Ilyasov, A. I. Lur'e, et al., "Tritium content in the coolant of water-cooled–water-modulated (VVÉR) reactors," At. Energ., 46, No. 2, 79 (1979).
3. V. P. Kruglov, V. M. Ilyasov, I. G. Golubchikova, et al., "Tritium content in the water systems of the reactor in the fifth block of the Novovoronezhsk nuclear power plant," At. Energ., 53, No. 4, 225 (1982).
4. V. N. Grishin, Statistical Methods of Analysis and Planning of Experiments [in Russian], Moscow State Univ. (1975).

NEW FORMULA FOR THE SPECTRUM OF PROMPT NEUTRONS FROM FISSION

A. F. Grashin and M. V. Lepeshkin

UDC 539.179

The Maxwellian or Watt distribution is still commonly used to describe the laboratory spectrum of prompt neutrons from fission. Experiments, however, have repeatedly indicated deviations from these semiempirical formulas, the physical reasons for which were never clarified. The most interesting study in this respect is [1], where it is pointed out that a superposition of Maxwellian terms must be introduced to describe the energy spectrum $n(\varepsilon)$ in the center of mass system of the fragments for spontaneous fission of ^{252}Cf. Analogous effects were observed in the study of fragmentation of heavy nuclei in high-energy collisions (see, for example, [2]), which indicates the existence of a single mechanism governing the emission of particles with low and high excitation energy.

All of this served as a foundation for proposing a statistical model with a continuous temperature for describing the spectra [3]:

$$n(\varepsilon)=\int_0^\infty n_M(\varepsilon, \theta)\exp[-\Delta F(\theta)/\theta]\,d\theta = \text{const}\,\sqrt{\varepsilon}\,\frac{\exp[-\sqrt{\alpha^2+2\alpha\varepsilon/\tau}]}{\sqrt{\alpha^2+2\alpha\varepsilon/\tau}}. \quad (1)$$

Here the Maxwellian distribution $n_M(\varepsilon, \theta)$ for the temperature θ is averaged with a weighting factor which depends on the change in the free energy $\Delta F(\theta)$ in the process of emission of the observed particle. The integral in Eq. (1) was calculated analytically using the two-term expansion $\Delta F(\theta) = c_0 + c_2\theta^2$ of the free energy in powers of the temperature. The coefficients of this expansion cannot be calculated in the general case, so that two parameters are retained in formula (1): the average temperature $\tau = \bar{\theta}$ and the parameter α, whose inverse is determined by the variance of the temperature. In the limit $\alpha \to \infty$, the weighting factor has a δ-function form, so that the function (1) transforms into a Maxwell distribution. The superposition on an infinite time interval with finite values of α has a simple physical meaning, since it ultimately reflects the nonuniformity of nuclear processes. In other words, formula (1) may be viewed as the result of the application of nonequilibrium thermodynamics to nuclear

Translated from Atomnaya Énergiya, Vol. 58, No. 1, pp. 59-61, January, 1985. Original article submitted April 19, 1984.

 0038-531X/85/5801-0072$09.50

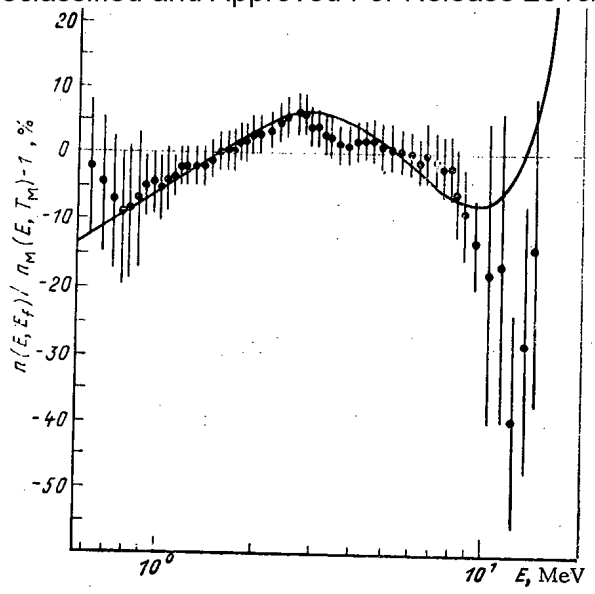

Fig. 1

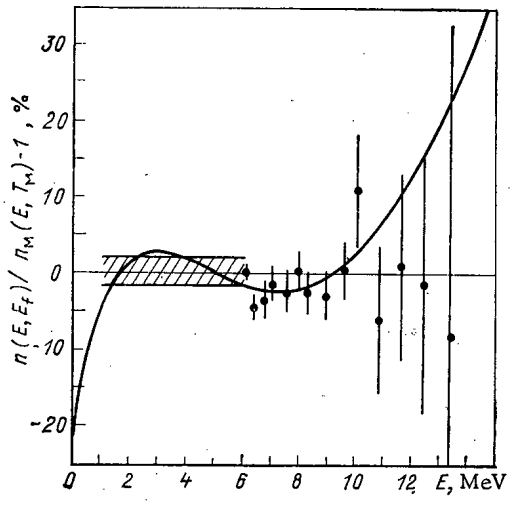

Fig. 2

Fig. 1. Ratio of the spectrum (2) and $n_{exp}(E_i)$ [5] for $^{235}U + n(0.53\ MeV)$ to the Maxwellian spectrum (8) with the parameter $T_M = 1.321$ MeV; $\chi^2/DF = 0.371$.

Fig. 2. Ratio of the spectrum (2) and $n_{exp}(E_i)$ [5] to the Maxwellian spectrum for ^{252}Cf (sf) [6] with $T_M = 1.424$ MeV, $\chi^2 = 11.4$ for $E \geq 6$ MeV.

processes.*

If the distribution (1) is transformed into the laboratory system of coordinates, a simple analytic formula is obtained:

$$n(E,\ E_f) = N\left[\exp\left(-\sqrt{X-Y}\right) - \exp\left(-\sqrt{X+Y}\right)\right]; \qquad (2)$$

$$X = \alpha^2 + 2\alpha\,(E+E_f)/\tau;\quad Y = 4\alpha\sqrt{EE_f}/\tau,$$

where E_f is the average kinetic energy of the fission fragments per nucleon; the coefficient N is found from the normalization condition of the energy spectrum. The limit $\alpha \to \infty$ corresponds to the usual equilibrium thermodynamics, and Eq. (2) transforms into the Watt distribution

$$n_W(E) = N_W \exp(-E/\tau)\,\mathrm{sh}\,(2\sqrt{EE_f}/\tau). \qquad (3)$$

The formula (2) was used to analyze the data on the fission of ^{235}U by 0.53-MeV neutrons [5] and the spontaneous fission of ^{235}Cf [6]. Here, we normalized the theoretical spectra as follows: we calculated the sums

$$\int_{E_{min}}^{E_{max}} n(E,\ E_f)\,dE = S_{theo} \sum_{i=min}^{max} n_{exp}(E_i)\,\Delta E_i = S_{exp}, \qquad (4)$$

after which we minimized the weighted mean of the sum of the deviations of the experimental values $n_{exp}(E_i)$ from the values

$$n^*(E_i,\ E_f) = (S_{exp}/S_{theo})\,n(E_i,\ E_f). \qquad (5)$$

Substituting the experimental values of the average energy $E_f = 0.805$ and 0.784 MeV for uranium and californium, respectively, we obtained†

*In [4] the neutron spectra were also calculated taking into account the temperature continuum, but the superposition of the temperature on a finite interval $0 \leq \theta \leq \theta_{max}$ was studied. This leads to a considerable difference in the high-energy region (see below).

†We point out the fact that in contrast to uranium we did not have reliable tabulated data for californium, so that the values of the parameter (7) must be refined as experimental data is accumulated.

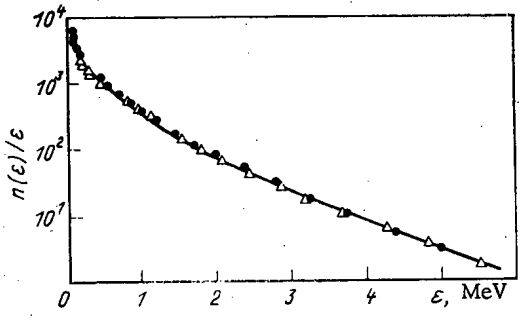

Fig. 3

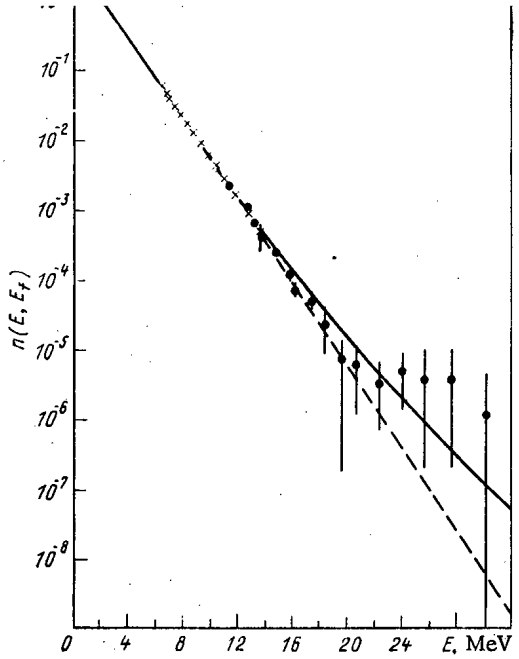

Fig. 4

Fig. 3. Comparison of the experimental spectrum for light and heavy fragments in the center of mass system of the fragments with the theoretical formula (1) for the parameters (7) in the case ^{252}Cf (sf). The values of $n(\varepsilon)/\varepsilon$ examined in [1] are shown.

Fig. 4. Comparison of the theoretical spectrum (2) with the parameters (7) and the Maxwellian spectrum with T_M = 1.424 MeV (broken curve) with the experimental data for ^{252}Cf(sf): ×) [6], ●) [7]. The normalization is arbitrary.

$$\tau = 0.777 \pm 0.007 \text{ MeV}, \quad \alpha = 18.4 \pm 1.6 \text{ for } {}^{235}\text{U} + n \text{ (0.53 MeV)}, \tag{6}$$

$$\tau = 0.848 \pm 0.007 \text{ MeV}, \quad \alpha = 13.5 \pm 0.8 \text{ for } {}^{252}\text{Cf}(sf). \tag{7}$$

Figures 1 and 2 show the theoretical spectra and the experimental points, divided for convenience by the previously used Maxwellian function

$$n_M(E, T_M) = N_M \sqrt{E} \exp(-E/T_M), \tag{8}$$

which was normalized analogously to the function (2). The agreement between Eq. (2) and the laboratory spectra leads to the agreement between Eq. (1) and the data in [1] in the center of mass system (Fig. 3). A significant difference between the distribution (2) and the Maxwellian distribution and the spectrum presented in [4] is the increasing excess in the high-energy part, i.e., in the "tail" of the distribution. We observed this excess experimentally [7] for ^{252}Cf(sf) in the region 16 < E < 30 MeV (Fig. 4). We observed an analogous difference from the Maxwellian tails for different particles created in high-energy collisions [3].

The thermodynamic theory of fission [8] gives a relationship between the changes in the temperature τ and the excitation energy E* of the fissioning nucleus

$$\Delta E^* = a_{ef} \Delta (\tau + T_0)^2, \tag{9}$$

where a_{ef} is the effective parameter of the density of states; $T_0 \approx 1.15$ MeV, which permits rescaling the values of τ obtained from the analysis of the spectra to the case of other values of the excitation energy with constant α. Thus for ^{235}U the relation (9) with the parameter $a_{ef} = A_F/15$ MeV can be written in the form

$$\Delta\tau \approx 0.017 \Delta E^*. \tag{10}$$

by 7-MeV neutrons τ = 0.89 MeV with α = 18.4, which agrees with the experiment in [9].

It should be noted that τ obtained from neutron spectra for $^{235}U + n(th)$ agrees within the limits of error with the nuclear temperature τ = 0.75 MeV in the thermodynamic theory of fission [8]. Thus, the parameters of the proposed model and the model itself have a clear physical meaning. In addition, the Watt distribution (3) does not agree with experiment for the physical values of E_f, so that it is used as a two-parameter formula, varying τ and E_f simultaneously. In this case, both the parameter and model become physically meaningless.

In conclusion, we note that more accurate experimental data should be analyzed by applying formulas (2) to the light and heavy fragments and summing the corresponding weighted contributions. In this work, we restricted our attention to an analysis using the value of E_f averaged over the light and heavy fragments.

LITERATURE CITED

1. H. Bowman et al., Phys. Rev., 126, 2120 (1962); E. Khaid, I. Perlman, and G. Seaborg, Nuclear Properties of the Heavy Elements [in Russian], No. 5, Atomizdat, Moscow (1969).
2. G. Westfall et al., Phys. Rev., C17, 1368 (1978).
3. A. F. Grashin and Ya. Ya. Shalamov, Yad. Fiz., 29, No. 3, 625 (1979).
4. D. Madland and J. Nix, Nucl. Sci. Eng., 81, 213 (1982).
5. P. Johansson and B. Holmqvist, Nucl. Sci. Eng., 62, 695 (1977).
6. J. Boldeman, D. Culley, and R. Cawley, Trans. Am. Nucl. Soc., 32, 733 (1979).
7. H. Marten, D. Seeliger, and B. Stobinski, in: Proc. 12th Int. Symp. Nucl. Phys. Heavy-Ion Collisions and Nucl. Fission, Gaussig, Nov. 22-26, 1982, p. 122.
8. A. F. Grashin, A. D. Efimenko, and V. M. Kolobashkin, in: Methods of Experimental Nuclear Physics in Studies of Fission Processes and Products [in Russian], Énergoatomizdat, Moscow (1983), p. 43; A. F. Grashin, in: Current Problems in Fission Physics [in Russian], Moscow (1983), p. 28.
9. J. Frehaut, A. Bertin, and R. Bois, Trans. Am. Nucl. Soc., 32, 732 (1979).

SPECTROMETRY OF THE MULTIPLICITY OF GAMMA QUANTA ON A STATIONARY RESEARCH REACTOR

Yu. V. Adamchuk, A. L. Kovtun, G. V. Muradyan, Yu. G. Shchepkin,* G. Georgiev, N. Kalinkova, E. Moravska, N. Stancheva, N. Chikov, and N. Yaneva†

UDC 539.125.5.164.078: 621.039.55

A new technique has been developed at the I. V. Kurchatov Institute of Atomic Energy for measuring neutron cross sections and studying the channels of formation and decay of excited nuclei: the spectrometry of multiplicity of secondary radiation emitted by excited nuclei [1, 2]. In particular, spectrometric measurement of the radiation of reaction products enables the identification of radiation capture, fission, and neutron scattering events. The neutron cross sections of nuclei of many elements have been measured with high accuracy with this method in a wide range of energies [3-6]. In this paper we describe the technique for measuring the neutron cross sections based on the spectrometry of the multiplicity in the low-energy range (<0.4 eV) based on the stationary thermal reactor. Measurement of cross sections by the method of spectrometry of multiplicities with the use of a reactor as the source of neutrons makes it possible to determine with high accuracy neutron cross sections with a small amount of matter. This is linked to the high intensity of the thermal neutron flux and the possibility of quite accurate determination of the background level.

The experimental setup is shown schematically in Fig. 1. The multiplicity spectrometer consists of a Romashka 12-section scintillation detector based on the NaI(Tl) crystals with a volume of 16.1 liters [1]. A through channel with a diameter of 38 mm, for the passage

*USSR.
†People's Republic of Bulgaria.

Translated from Atomnaya Énergiya, Vol. 58, No. 1, pp. 61-63, January, 1985. Original article submitted April 19, 1984.

0038-531X/85/5801-0075$09.50

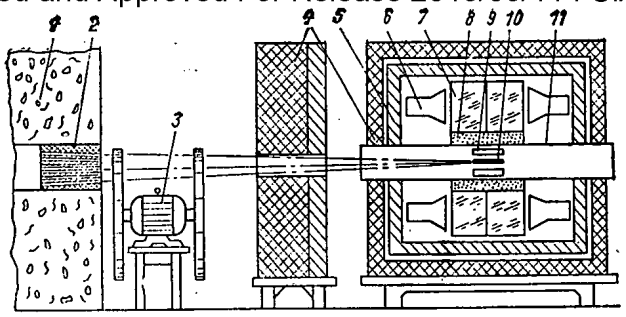

Fig. 1

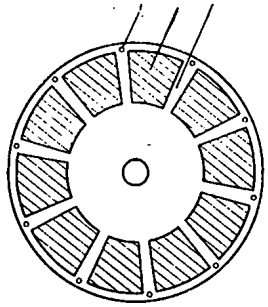

Fig. 2

Fig. 1. Experimental setup: 1) radiation shield of the reactor; 2) multigap collimator; 3) neutron interruptor–monochromator; 4) paraffin with boric acid; 5) lead; 6) photomultiplier; 7) NaI(Tl) crystals; 8) shielding from ^{6}Li carbonate; 9) Si-semiconductor detectors; 10) target; 11) evacuated chamber for sample.

Fig. 2. Neutron interruptor–monochromator disk: 1) opening for light pulse, triggering the system; 2) cadmium plate; 3) transmitting gap.

of a neutron beam and for the insertion of an evacuated chamber for a sample of length 1,2 m, is located at the center of the detector. It contains the sample and a silicon semiconductor detector for registering the fission fragments of nuclei. The latter is located outside the passing neutron beam. The combination of a multiplicity detector with detectors registering fission fragments enables precision measurements of the cross sections of radiative capture and fission and their ratio (α), as well as the study of the correlation of the fission products. A layer of ^{6}Li carbonate 1 g/cm^2 thick, acting as a shield for thermal neutrons scattered by the sample, is located between the evacuated chamber for the sample and the crystals. The exterior shielding of the detector consists of a layer of lead 10 cm thick and a mixture of paraffin with boric acid 20 cm thick. The shielding on the reactor side is increased by layers of lead 20 cm thick and paraffin with boric acid 60 cm thick.

A mechanical interruptor–monochromator [7] consisting of two coaxially rotating duraluminum disks 8 mm thick with a diameter of 620 mm was developed and fabricated for performing spectrometric measurements of neutrons with energies <0.4 eV and for simultaneously separating out the quasimonochromatic line. A layer of cadmium 0.5 mm thick, in which 10 equidistant radial gaps were made, was inserted into each disk (Fig. 2). The gaps on one disk are displaced with respect to the gaps of the other disk by a definite angle, corresponding to the quasimonochromatic line being separated. The monochromatization used, because of the large number of gaps, permits increasing the intensity of the incident beam and determining the background level with high accuracy. The background is determined from time-of-flight sections, positioned on both sides of the time interval corresponding to the neutron energy separated (Fig. 3). In the sections for determining the background level, there are practically no neutrons with the energy examined. It should be noted that with the examined method of monochromatization and determination of the background, the latter is found with high accuracy, so that the conditions for passage of background neutrons and γ quanta through the interruptor remained virtually unchanged as a function of the position of the disks. Monochromatization of neutrons and exact determination of the background by the method examined are achieved at the expense of decreasing the flux of neutrons with the energy separated out, but the ratio of the "effect" to the "background" remains high due to the high cadmium ratio.

The setup under study permits measuring different cross sections, but, as noted above, its particular feature consists of the fact that it is possible to measure cross sections on this setup with the use of a small amount of matter while at the same time performing spectrometric measurements on the thermal neutrons. The energy resolution of the setup with a flight baseline of 3.5 m and a neutron pulse duration of $\tau_n \approx 90$ μsec is equal to 12.5% for 0.025-eV neutrons. This setup permits determining the radiative-capture cross section of radioactive nuclei, measuring with high accuracy the ratio of the radiative-capture and fission cross sections α as a function of the neutron energy in the thermal energy range and, in particular, for 0.0253-eV neutrons.

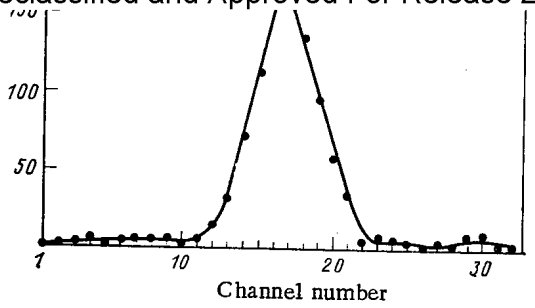

Fig. 3

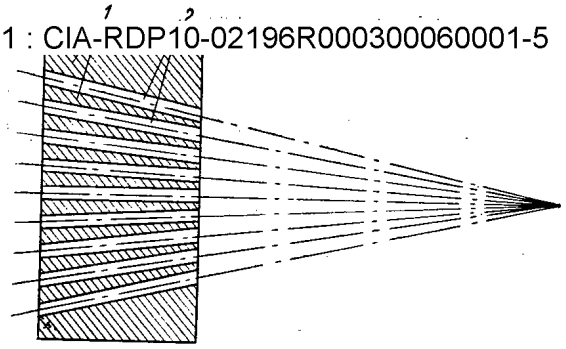

Fig. 4

Fig. 3. Time-of-flight spectrum of the coincidences between the Romashka and semiconductor detectors for k = 6: ●) experimental points.

Fig. 4. Schematic section of the multigap collimator: 1) cadmium shields; 2) collimator gaps.

The high sensitivity of the Romashka detector to background neutrons and measurements with a small amount of the matter being studied impose certain restrictions on the collimation system collimating the neutron beam. The small amount of matter requires that the detector be placed closer to the reactor. This, in turn, leads to the fact that the angular divergence of the neutron beam increases within the limits of the detector. Thus, it becomes necessary to increase the distance between the sample and the semiconductor fission-fragment detector, which decreases its detection efficiency and increases the size of the scintillation detector. For this reason, when the dimensions of the latter are preserved, the geometry of the arrangement of the sample and the semiconductor detector, placing the setup closer to the reactor, requires that the transverse section of the beam be limited when it is collimated. But this limitation strongly decreases the neutron flux at the sample. To solve this problem, a special multigap collimator was developed [7, 8], which passes the neutron beam with a small divergence within the detector with a comparatively low loss of beam intensity (Fig. 4). The axes of the collimator gaps converge at the center of the detector, where the sample is located. At this point the size of the beam, determined with the help of photographic film, does not exceed 15 × 20 mm.

The measuring–computing system is based on the standard CAMAC blocks and a small TRA-i-1001 computer (Fig. 5). The system includes the following basic blocks: time encoder, coincidence multiplicity encoder, input register, control block. The coincidence multiplicity encoder [9] converts into a binary code the number of events entering within a given time interval (∿1 μsec) from the sections of the detector. The encoder operates according to the principle of parallel loading of information from the detector sections into a shift register with subsequent counting of the number of triggered cells. When single events are recorded, the number of the detector section appears at the output of the encoder, which makes it possible to control the operation of separate sections. The indication of each event, determining whether it belongs to the scintillation detector or the semiconductor detector or the random-pulse generator, is loaded into the parallel input register. Three signs, characterizing the response of the first, second, and third integral discriminators to the total amplitude of the pulses from all sections of Romashka, are loaded into the same register. These three thresholds are introduced in order to make a precise determination of the efficiency of the detector when registering radiative capture. In addition, the input register, together with the control block, is used to synchronize the overall operation of the system. The insertion of a random-pulse generator permits taking into account miscounts in the time spectra.

The events fed to the computer are analyzed and grouped according to the time of flight of the neutrons, the multiplicity of the coincidences, and three discrimination thresholds of the total energy liberation in the scintillation detector belonging to the sensor (Romashka detector, semiconductor detector, random-pulse generator). A maximum of 109 time spectra can be recorded.

The value of $\alpha^{235}U$ at the thermal point was measured on the spectrometer developed. In the measurements, we used a layer of uranium 0.7 mg/cm² thick. The total amount of uranium was equal to ∿20 mg. Figure 3 shows the time-of-flight spectrum of the coincidences between Romashka and the semiconductor detector for a multiplicity of k = 6. It is evident from this

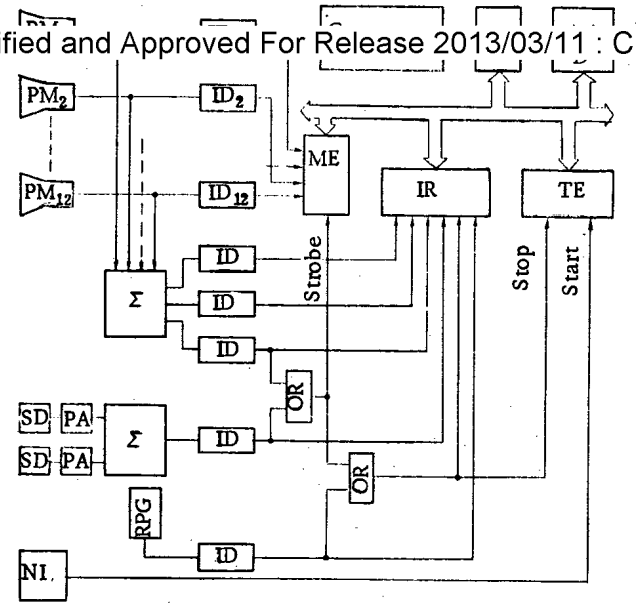

Fig. 5

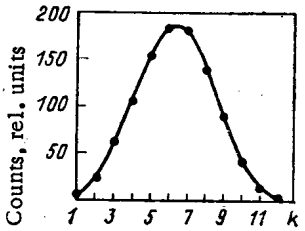

Fig. 6

Fig. 5. Structural diagram of the electronic apparatus: integral discriminators (ID); CAM crate controller (C); point display (D); coincidence multiplicity encoder (ME); input register (IR); time encoder (TE); linear adder (Σ); semiconductor Si detector (SD); preamplifier (PA); logical OR circuit (OR); electronic random-pulse generator (RPG); neutron interruptor–monochromator (NI); photomultiplier (PM).

Fig. 6. Spectrum of multiplicity of coincidences between Romashka and the semiconductor detectors: ●) experimental points.

figure that the effect-to-background ratio is good. Figure 6 shows the spectrum of multiplicity in the coincidences with fission fragments for ^{235}U. It is evident that the peak is located in the region of coincidence multiplicities k = 6 and 7. Here, for k = 6, where capture events are expected, the fission fraction is equal to ∿50%.

A measurement of the spectrum of multiplicity in the coincidence with fission fragments permits determining the efficiency of detection of fission events by the Romashka detector. This efficiency exceeds 99% at the threshold of 0.2 MeV. At the same time, since the volume of the detector is only 16.6 liters, the characteristic background level does not exceed 150 counts per sec. Such a high efficiency permits performing absolute measurements of cross sections and their ratios. For comparison we point out that the efficiency of detection of fission for a liquid scintillation tank with a volume of 3000 liters is only 80% with a much higher background level [10].

Thus, the technique developed permits performing absolute measurements of neutron cross sections and their ratios with a high degree of accuracy. Its advantages are especially clearly manifested in measurements of neutron cross sections with a small amount of matter and in measurements of cross sections of radioactive nuclei.

LITERATURE CITED

1. G. V. Muradyan, Yu. G. Shchepkin, Yu. V. Adamchuk, and G. I. Ustroev, "Study of neutron cross sections and quantum characteristics of nuclear levels based on spectrometry of the multiplicity of emissions of nuclei," Preprint IAÉ-2634, Moscow (1976).
2. G. V. Muradyan, "Spectrometry of multiplicity," At. Energ., 50, No. 6, 394-398 (1981).
3. G. Muradyan, Yu. Schchepkin, Yu. Adamchuk, and M. Voskanyan, "A measurement of U-235 absolute alpha value in the neutron energy range from 0.1 to 30 keV," in: Proc. Int. Conf. Nuclear Cross Section for Technology (1980), pp. 488-490.
4. Yu. V. Adamchuk, M. A. Voskanyan, G. V. Muradyan et al., "Measurement of the capture cross section of ^{235}U," in: Neutron Physics. Proceedings of the IV All-Union Conference on Neutron Physics, Kiev, 18-22 April 1977, Moscow (1977), Part 2, pp. 192-195.
5. G. V. Muradyan, Yu. G. Shchepkin, Yu. V. Adamchuk, et al., "Measurement of the fission and capture cross sections and the value of alpha of ^{235}U," in: Neutron Physics. Pro-

Moscow (1977), Part 2, pp. 119-125.
6. S. T. Bak"rdzhiev and G. P. Georgiev, "Mechanical system for collimation and monochromatization of a neutron beam in the horizontal channel No. 4 of the reactor IRT-2000," Yad. Energ., 20, 25 (1984).
7. G. V. Muradyan, G. I. Ustroev, Yu. G. Shchepkin, et al., "Collimation of a neutron beam in experiments on the measurement of partial cross sections with a small amount of material," Preprint IAÉ-2470, Moscow (1974).
8. A. A. Bogzdel', Ts. Ts. Panteleev, N. S. Stancheva, V. G. Tishin, and Fo Dik Toan, "Set-up for coding the multiplicity of coincidences in the CAMAC standard for work with a multisectioned detector," Report B31 at the 11th Int. Symposium on Nuclear Electronics, Bratislava (1984).
9. R. Gwin, E. Silver, R. Ingle, and H. Weaver, "Measurement of the neutron capture and fission cross sections of Pu-239 and U-235, 0.02 eV to 200 keV, the neutron capture cross sections of Au-197, 10 to 50 keV, and neutron fission cross sections of U-235, 5 to 200 keV," Nucl. Sci. Eng., 59, 79-105 (1976).

NEUTRON SOURCES BASED ON A BOOSTER

N. I. Alekseev

UDC 539.125.5.03

One of the trends in research on the production of high-intensity neutron sources is developing them on the basis of a booster — a multiplying subcritical assembly with neutron injection (for example, using charged-particle conversion processes). The subcritical assembly is, as a rule, used simultaneously as a target for converting charged particles to neutrons and as a multiplier of these neutrons by means of a fission reaction. Such a source can operate under either stationary or pulsed conditions.

The purpose of the present study was to obtain an expression for determining the peak neutron flux density and investigate the variation of this value as a function of the dimensions and material of the target.

Suppose that a multiplying subcritical medium with volume V contains a neutron injector which is constant with respect to time and has intensity $Q(\mathbf{r}_0, \Omega_0, E_0)$ ($\mathbf{r}_0$, Ω_0, E_0 are the variables of the spatial, angular, and energy distributions of the injector neutrons over the volume). Then the density of neutrons with energy E at the point $\mathbf{r}$ which are flying in the direction Ω can be expressed in terms of the Green's function as follows [1]:

$$\Phi(\mathbf{r}, \Omega, E) = \int\int\int Q(\mathbf{r}_0, \Omega_0, E_0)\, G(\mathbf{r}_0, \Omega_0, E_0 \to \mathbf{r}, \Omega, E)\, d\mathbf{r}_0\, d\Omega_0\, dE_0. \quad (1)$$

We divide both sides of formula (1) by W_0, the total rate of neutron generation over the volume V:

$$W_0 = \int\int\int Q(\mathbf{r}_0, \Omega_0, E_0)\, d\mathbf{r}_0\, d\Omega_0\, dE_0 + \int\int\int F(\mathbf{r}', \Omega', E')\, d\mathbf{r}'\, d\Omega'\, dE', \quad (2)$$

where $f(\mathbf{r}', \Omega', E')$ is the rate of generation of fission neutrons.

The resulting ratio of neutron flux density to the total generation rate W_0 will be denoted by $\mu(\mathbf{r}, \Omega, E)$ and called the neutron influence coefficient

$$\mu(\mathbf{r}, \Omega, E) = 1/W_0 \int\int\int Q(\mathbf{r}_0, \Omega_0, E_0)\, G(\mathbf{r}_0, \Omega_0, E_0 \to \mathbf{r}, \Omega, E)\, d\mathbf{r}_0\, d\Omega_0\, dE_0. \quad (3)$$

The influence coefficient is numerically equal to the flux density in a medium with total neutron generation rate of one neutron per second and has the dimensions of $1/cm^2$. The neutron flux density for an arbitrary generation rate can be written as follows:

$$\Phi(\mathbf{r}, \Omega, E) = \mu(\mathbf{r}, \Omega, E)\, W_0. \quad (4)$$

We introduce the neutron amplification factor as the ratio of the total generation rate

Translated from Atomnaya Énergiya, Vol. 58, No. 1, pp. 64-65, January, 1985. Original article submitted April 19, 1984.

0038-531X/85/5801-0079$09.50

to the injector power:

$$K_a = W_0 \Big/ \int\int\int\int Q(\mathbf{r}_0, \Omega_0, E_0)\, d\mathbf{r}_0\, d\Omega_0\, dE_0. \tag{5}$$

Then the neutron flux density (4) takes the following form:

$$\Phi(\mathbf{r}, \Omega, E) = \mu(\mathbf{r}, \Omega, E) K_a \int\int\int Q(\mathbf{r}_0, \Omega_0, E_0)\, d\mathbf{r}_0\, d\Omega_0\, dE_0. \tag{6}$$

For a multiplying medium with a spatial distribution of neutrons with respect to the zeroth harmonic, the amplification factor is equal to [2]

$$K_a = 1/[1 - K_e(1-\beta)], \tag{7}$$

where K_e is the effective multiplication factor and β is the fraction of delayed neutrons.

If the injector operates in the pulsed regime with period T, then, introducing the concept of effective duration of the neutron pulse

$$\tau_e = 1/\Phi_{pk} \int_0^T \Phi(t)\, dt, \tag{8}$$

we can obtain an expression for the peak value of the neutron flux density

$$\Phi_{pk} = 1/\tau_e \int_0^T \Phi(t)\, dt. \tag{9}$$

Assuming that the per-pulse average flux density in the nonstationary problem is the same as in a stationary problem with an injector power equal to the per-pulse average injector power in the nonstationary problem, we obtain

$$\Phi_{pk}(\mathbf{r}, \Omega, E) = 1/\tau_e\, \mu(\mathbf{r}, \Omega, E) K_a \int\int\int\int Q'(\mathbf{r}_0, \Omega_0, E_0, t_0)\, d\mathbf{r}_0\, d\Omega_0\, dE_0\, dt_0. \tag{10}$$

If the time-dependence curve of the injector neutron pulse is rectangular in shape (which is characteristic of all accelerators) with pulse width τ and the injector intensity integrated over volume, directions, and energy $Q'(\mathbf{r}_0, \Omega_0, E_0, t_0)$ is S_0 (for particles with unit charge we have $S_0 = 10^{19}/1.6 i_{pulse} P$, where i_{pulse} is the particle current in a pulse, and P is the coefficient of conversion of charged particles to neutrons), then the peak value of the neutron flux density will be equal to

$$\Phi_{pk}(\mathbf{r}, \Omega, E) = (\tau/\tau_e)\, \mu(\mathbf{r}, \Omega, E) K_a S_0. \tag{11}$$

In [2], for the estimate of the effective neutron pulse duration in a moderator with a slowing-down time much less than the time $\mathcal{L}$ up to the absorption and leakage of a themal neutron, and on the assumption that the time and space variables are separable, we obtained the following expression:

$$\tau_e^{\tau} = \tau (e^{\tau/lK_a} - 1)^{lK_a/(\mathcal{L} - lK_a)} (e^{\tau/\mathcal{L}} - 1)^{-\mathcal{L}/(\mathcal{L} - lK_a)}, \tag{12}$$

where l is the lifetime of the prompt neutrons.

As an example, we performed calculations of neutron sources with a target made of fuel elements with either metallic or dioxide fuel. A target 200 mm high was surrounded on all sides with a light-water moderator 500 mm thick. The diameter of the fuel element was taken to be 5 mm, the pitch of the fuel-element lattice to be 5.4 mm, the uranium dioxide density in the core 10 g/cm^3, and the metallic uranium density 18.9 g/cm^3. To shorten the pulse duration, we coated the target with cadmium 1 mm thick. The calculations were carried out in cylindrical geometry by the Monte Carlo method, using the MMKFK program [3]. The results of the calculations of the neutron-source characteristics are shown in Figs. 1 and 2 for the "Fakel'" ("Torch") electron accelerator with the following parameters: electron energy $\sim$60 MeV, current per pulse $\sim$1 A, frequency 150 Hz, pulse duration 5.5 μsec [4], injector intensity per pulse for full conversion was $S_0 = 2 \cdot 10^{17}$ neutrons/sec.

In the calculation it was assumed that the conversion neutrons were isotropic, had a fission spectrum, and were spatially distributed according to the zeroth harmonic of the target. The peak thermal-neutron flux density in the moderator is given (see Fig. 2) at a dis-

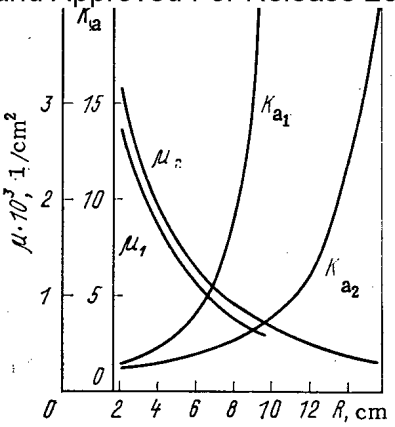

Fig. 1

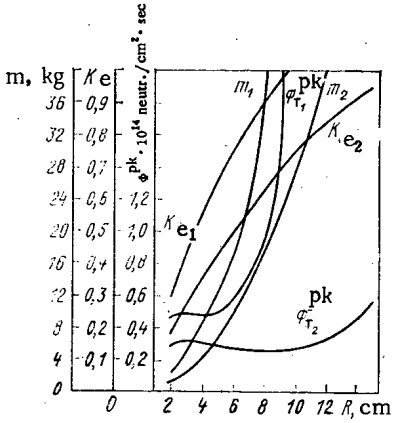

Fig. 2

Fig. 1. Influence coefficient for thermal neutrons in the moderator (μ) and amplification factor (K_a) as functions of the target radius (R) for a target height of 20 cm: 1, 2) fuel elements with metallic and dioxide fuel, respectively.

Fig. 2. Peak unperturbed thermal-neutron flux density in moderator (Φ^{pk}), effective multiplication factor K_e, and charge of ^{235}U (m) as functions of the radius (R) of a target 20 cm high: 1, 2) fuel elements with metallic and dioxide fuel, respectively.

tance approximately equal to the diffusion length from the target (the zone of spatial maximum of the flux), where the effective pulse duration (for $K_a \leqslant 20$) for a target with dioxide fuel is about 105 μsec, while in the variants with metallic uranium it is about 90 μsec.

From Figs. 1 and 2 it can be seen that with increasing target radius the amplification factor and the charge of fissionable material increase monotonically, the influence coefficient decreases, and the thermal-neutron flux density varies nonmonotonically. If we keep $K_a < 10$ (for $K_e < 0.9$, nuclear test stands do not always have reactivity control systems), then for a target with dioxide fuel, when $K_a \simeq 1.5$ ($m \simeq 2.5$ kg), the peak neutron flux density is the same as for $K \simeq 10$ ($m \simeq 50$ kg) and amounts to about $3 \cdot 10^{13}$ neutrons/(cm²·sec). Using a small target reduces the uranium consumption (by a factor of about 20). With increasing density of fissionable material, the flux density increases and the zone of nonmonotonic behavior of the flux becomes narrower. In a source with metallic fuel, for $K_a \simeq 10$ ($m \simeq 37$ kg) the peak flux density is about twice as high as the flux density for $K_a \simeq 1.5$ ($m \simeq 3.7$ kg) and is equal to $\sim 9 \cdot 10^{13}$ neutrons/(cm²·sec). The calculations show that the most intensive growth of thermal-neutron flux density in the moderator (an increase by a factor of 6-10) is observed when the amplification factor is increased from 10 to the limiting value (about 150 for ^{235}U). The charge of fissionable isotope increases by about 50%.

LITERATURE CITED

1. D. Bell and S. Glasstone, Theory of Nuclear Reactors [Russian translation], Atomizdat, Moscow (1974).
2. N. I. Alekseev et al., Preprint IAÉ-2775, Moscow (1977).
3. L. V. Maiorov, Vopr. At. Nauki Tekh., Ser. Fiz. Tekh. Yad. Reaktorov, No. 8 (21), 7 (1981).
4. M. I. Pevzner et al., Preprint IAÉ-2122, Moscow (1971).

USE OF METALLIC LITHIUM FOR DETECTING SOLAR NEUTRINOS

E. P. Veretenkin, V. N. Gavrin, and E. A. Yanovich

UDC 539.12,123+546.34.45.02.7

Work on the development of new radiochemical neutrino detectors [1], including detectors based on lithium, was significantly stimulated by the disagreement between the value of the solar neutrino flux recorded by Davis [2, 3] with a chlorine–argon detector and the value theoretically predicted by the standard solar model [4]. The use of the reaction $^7Li(\nu_e,e^-)^7Be$ for detecting solar neutrinos has been discussed since 1964 [5, 6, 7]. Different methods for extracting single atoms of ^7Be from lithium-containing targets and possible methods for their detection [8, 9, 10, 11] have been studied over this time period. All examined extraction methods depend on the use of a water solution of lithium chloride, which involves a large detector volume and strict requirements on the admissable concentration of impurity alpha-active elements in the detector. Thus, in order that the background from the internal radioactivity not exceed 10% of the effect expected from the neutrino pep reaction, the uranium and thorium concentration in the water solution of LiCl must not exceed $5\cdot10^{-11}$ g/g [12], and this is a factor of three lower than the usual contamination of environmental materials. In addition, the background from cosmic-ray muons in the detector based on the aqueous solution of LiCl exceeds by a factor of 30 the same background in a detector based on metallic lithium at the same depth [12].

In this connection, an attempt was made to find an efficient method for extracting single atoms of ^7Be directly from metallic lithium. For this, we studied the coprecipitation of microscopic quantities of beryllium with a solid collector, which consisted of lithium oxide and nitride, contained in commercially produced lithium in quantities of $(5\text{-}10)\cdot10^{-2}$ mass% [13]. We separated the solid phase containing beryllium from the lithium by low-temperature filtering. The choice of this method was based on the fact that the isobaric–isothermal formation potentials of BeO and Be_3N_2 are lower than the formation potentials of Li_2O and Li_3N and the beryllium occurs in the lithium in the form of the oxide and the nitride. It may therefore be expected that when the oxides and nitrides crystallize in zones of low temperature the beryllium concentrates in the solid phase.

We performed the studies on a setup consisting of a vertical assembly of two vessels made of 12Kh18N10T stainless steel, which are separated by a metalloceramic filter with a pore size of 15 μm. We placed the assembly into a heated evacuated chamber. We placed a 50-g mass of lithium, containing radioactive ^7Be, in the upper vessel and melted it in a vacuum of $\sim10^{-3}$ mm Hg. We monitored the temperture with thermocouples. After holding at 400°C for 1 h, we cooled the specimen to 200°C and pressed it with argon through the filter into the lower vessel. We monitored its extraction via the gamma activity of ^7Be in the starting and filtered as well as the solid phases on the filter. We measured the activity with a NaI(Tl) crystal. We injected the ^7Be into the sample studied together with the lithium irradiated on a cyclotron. To form ^7Be by the reaction $^7Li(v, n)^7Be$, we irradiated the 1-g lithium target with 7-MeV protons and alloyed it with the studied sample directly in the setup.

The measurements showed that 95% of the ^7Be concentrates on the filter; in addition, the total mass of the filtered phase is less than 0.5% of the starting phase.

For filtering performed in the isothermal state at 400°C, the amount of ^7Be on the filter decreases threefold, which quantitatively agrees with the increase of the solubility of lithium oxide and nitride.

To prove the independence of the efficiency of the extraction from the starting distribution of beryllium in the sample, we filtered the lithium irradiated by 120-MeV protons. The irradiated 60-g sample consisted of a cylinder with a diameter of 40 mm and 100 mm long. Since the mean free path length of 120-MeV protons is much larger than the geometric dimensions of the target, the ^7Be formed in it uniformly over the entire volume. When the fil-

Translated from Atomnaya Énergiya, Vol. 58, No. 1, pp. 65-66, January, 1985. Original article submitted March 2, 1984.

 0038-531X/85/5801-0082$09.50

teri d and starting samples was equal to 0.02, which corresponds to a content of 98% ^{7}Be on the filter. Thus, the filtering at a temperature close to the melting point permits extracting ^{7}Be without a carrier from the melted lithium with an efficiency close to 100%.

After dissolving the filtered solid phase in a comparatively small amount of water, the methods examined in previous works [9, 10, 11] can be used to extract ^{7}Be from the water solution, to synthesize beryllium acetylacetonate, and to measure its activity in a proportional counter.

Since for a full-scale neutrino experiment it is necessary to have no less than 10 tons of lithium, this procedure must be tested on model setups containing tens and hundreds of kilograms of lithium. In so doing, for scale modeling it is primarily necessary to study the dependence of the coefficient of distribution of beryllium between the solid and liquid phases as a function of the temperature and composition of the solid phase.

In conclusion, the authors thank G. T. Zatsepin and A. E. Chudakov for useful discussions and I. R. Barabanov, Yu. I. Zakharov, I. V. Orekhov, and L. Ya. Shavtvalov for useful suggestions and assistance.

LITERATURE CITED

1. I. Barabanov, A. Egorov, V. Gavrin, et al., "Present state and outlook for development of the solar neutrino astronomy," in: Proc. Int. Conf. "Neutrino 77," Moscow (1978), pp. 20-41.
2. R. Davis, S. Harmer, and H. Hoffman, "Search for neutrinos from the sun," Phys. Rev. Lett., 20, 1205-1209 (1968).
3. R. Davis, B. Cleveland, and J. Rowley, "Underground science at homestake," Science Underground Workshop, Los Alamos, 1982, New York (1983), pp. 2-15.
4. J. Bahcall, W. Huebner, S. Lubow, et al., "Standard solar models and the uncertainties in predicted capture rates of solar neutrinos," Rev. Mod. Phys., 54, No. 3, 767-799 (1982).
5. V. Kuzmin and G. Zatsepin, "On the neutrino spectroscopy of the sun," in: Proc. Int. Conf. Cosmic Rays, London (1966), pp. 1023-1025.
6. J. Rahcall, Phys. Lett., 13, 332 (1964).
7. F. Reines and R. Woods, "New approach to the detection of solar neutrinos via inverse beta decay," Phys. Rev. Lett., 14, 20-24 (1965).
8. A. A. Pomanskii, "Practical possibility for utilizing lithium as a solar-neutrino detector," Preprint Physics Institute, Academy of Sciences of the USSR (1966).
9. N. P. Rudenko, A. I. Sevast'yanov, G. T. Zatsepin, and A. A. Pomanskii, "Removal of lithium chloride from beryllium with a ratio Be/Li = $1/10^{18}$ as an example of deep purification of some compounds," Vestn. Mosk. Univ., No. 4, 402 (1970).
10. J. Rowly, "The ^{7}Li—^{7}Be experiment," in: Proc. Informal Conf. on Status and Future of Solar Neutrino Research, Brookhaven National Laboratory, Upton, NY, 5-7 January 1978, pp. 265-291.
11. I. Barabanov, V. Gavrin, Yu. Zakharov, and G. Zatsepin, "Be counting in proportional counter," in: Proc. Int. Conf. "Neutrino 77," Moscow (1978), pp. 70-72.
12. Yu. Zakharov, "Background effect in solar neutrino experiments," in: Proc. Int. Conf. "Neutrino 77," Moscow (1978), pp. 64-69.
13. V. K. Grishin et al., Properties of Lithium [in Russian], Metallurgizdat, Moscow (1963).

How To Comply With The New Copyright Law

Participation in the Copyright Clearance Center (CCC) assures you of legal photocopying at the moment of need.

Libraries everywhere have found the easy way to fill photocopy requests legally and instantly, without the need to seek permissions, from more than 3000 key publications in business, science, humanities, and social science. You can:

Fill requests for multiple copies, interlibrary loan (beyond the CONTU guidelines), and reserve desk without fear of copyright infringement.

Supply copies from CCC-registered publications simply and easily.

The Copyright Clearance Center is your one-stop place for on-the-spot clearance to photocopy for internal use.

Its flexible reporting system accepts photocopying reports and returns an itemized invoice. You send only one convenient payment. CCC distributes it to the many publishers whose works you need.

And, you need not keep any records, the CCC computer will do it for you. Register now with the CCC and you will never again have to decline a photocopy request or wonder about compliance with the law for any publication participating in the CCC.

To register or for more information, just contact:

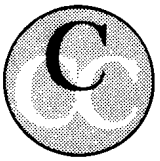

Copyright Clearance Center
21 Congress Street
Salem, Massachusetts 01970
(617) 744-3350

a not-for-profit corporation

NAME _____ TITLE _____

ORGANIZATION _____

ADDRESS _____

CITY _____ STATE _____ ZIP _____

COUNTRY _____ TELEPHONE _____

CHANGING YOUR ADDRESS?

In order to receive your journal without interruption, please complete this change of address notice and forward to the Publisher, 60 days in advance, if possible.

(Please Print)

Old Address:

name

address

city

state (or country) zip code

New Address

name

address

city

state (or country) zip code

date new address effective

name of journal

THE LANGUAGE OF SCIENCE
Plenum
PUBLISHING CORPORATION

233 Spring Street, New York, New York 10013

MEASUREMENT TECHNIQUES
Izmeritel'naya Tekhnika
Vol. 27, 1984 (12 issues) $520

MECHANICS OF COMPOSITE MATERIALS
Mekhanika Kompozitnykh Materialov
Vol. 20, 1984 (6 issues) $430

METAL SCIENCE AND HEAT TREATMENT
Metallovedenie i Termicheskaya Obrabotka Metallov
Vol. 26, 1984 (12 issues) $540

METALLURGIST
Metallurg
Vol. 28, 1984 (12 issues) $555

PROBLEMS OF INFORMATION TRANSMISSION
Problemy Peredachi Informatsii
Vol. 20, 1984 (4 issues) $420

PROGRAMMING AND COMPUTER SOFTWARE
Programmirovanie
Vol. 10, 1984 (6 issues) $175

PROTECTION OF METALS
Zashchita Metallov
Vol. 20, 1984 (6 issues) $480

RADIOPHYSICS AND QUANTUM ELECTRONICS
Izvestiya Vysshikh Uchebnykh Zavedenii, Radiofizika
Vol. 27, 1984 (12 issues) $520

REFRACTORIES
Ogneupory
Vol. 25, 1984 (12 issues) $480

SIBERIAN MATHEMATICAL JOURNAL
Sibirskii Matematicheskii Zhurnal
Vol. 25, 1984 (6 issues) $625

SOIL MECHANICS AND FOUNDATION ENGINEERING
Osnovaniya, Fundamenty i Mekhanika Gruntov
Vol. 21, 1984 (6 issues) $500

SOLAR SYSTEM RESEARCH
Astronomicheskii Vestnik
Vol. 18, 1984 (6 issues) $365

SOVIET APPLIED MECHANICS
Prikladnaya Mekhanika
Vol. 20, 1984 (12 issues) $520

SOVIET ATOMIC ENERGY
Atomnaya Énergiya
Vols. 56-57, 1984 (12 issues) $560

SOVIET JOURNAL OF GLASS PHYSICS AND CHEMISTRY
Fizika i Khimiya Stekla
Vol. 10, 1984 (6 issues) $235

SOVIET JOURNAL OF NONDESTRUCTIVE TESTING
Defektoskopiya
Vol. 20, 1984 (12 issues) $615

SOVIET MATERIALS SCIENCE
Fiziko-khimicheskaya Mekhanika Materialov
Vol. 20, 1984 (6 issues) $445

SOVIET MICROELECTRONICS
Mikroélektronika
Vol. 13, 1984 (6 issues) $255

SOVIET MINING SCIENCE
Fiziko-tekhnicheskie Problemy Razrabotki Poleznykh Iskopaemykh
Vol. 20, 1984 (6 issues) $540

SOVIET PHYSICS JOURNAL
Izvestiya Vysshikh Uchebnykh Zavedenii, Fizika
Vol. 27, 1984 (12 issues) $520

SOVIET POWDER METALLURGY AND METAL CERAMICS
Poroshkovaya Metallurgiya
Vol. 23, 1984 (12 issues) $555

STRENGTH OF MATERIALS
Problemy Prochnosti
Vol. 16, 1984 (12 issues) $625

THEORETICAL AND MATHEMATICAL PHYSICS
Teoreticheskaya i Matematicheskaya Fizika
Vol. 58-61, 1984 (12 issues) $500

UKRAINIAN MATHEMATICAL JOURNAL
Ukrainskii Matematicheskii Zhurnal
Vol. 36, 1984 (6 issues) $500

Send for Your Free Examination Copy

Plenum Publishing Corporation, 233 Spring St., New York, N.Y. 10013
In United Kingdom: 88/90 Middlesex St., London E1 7EZ, England
Prices slightly higher outside the U.S. Prices subject to change without notice.

RUSSIAN JOURNALS IN THE PHYSICAL AND MATHEMATICAL SCIENCES

AVAILABLE IN ENGLISH TRANSLATION

ALGEBRA AND LOGIC
Algebra i Logika
Vol. 23, 1984 (6 issues) $360

ASTROPHYSICS
Astrofizika
Vol. 20, 1984 (4 issues) $420

AUTOMATION AND REMOTE CONTROL
Avtomatika i Telemekhanika
Vol. 45, 1984 (24 issues) $625

COMBUSTION, EXPLOSION, AND SHOCK WAVES
Fizika Goreniya i Vzryva
Vol. 20, 1984 (6 issues) $445

COSMIC RESEARCH
Kosmicheskie Issledovaniya
Vol. 22, 1984 (6 issues) $545

CYBERNETICS
Kibernetika
Vol. 20, 1984 (6 issues) $445

DIFFERENTIAL EQUATIONS
Differentsial'nye Uravneniya
Vol. 20, 1984 (12 issues) $505

DOKLADY BIOPHYSICS
Doklady Akademii Nauk SSSR
Vols. 274-279, 1984 (2 issues) $145

FLUID DYNAMICS
Izvestiya Akademii Nauk SSSR, Mekhanika Zhidkosti i Gaza
Vol. 19, 1984 (6 issues) $500

FUNCTIONAL ANALYSIS AND ITS APPLICATIONS
Funktsional'nyi Analiz i Ego Prilozheniya
Vol. 18, 1984 (4 issues) $410

GLASS AND CERAMICS
Steklo i Keramika
Vol. 41, 1984 (6 issues) $590

HIGH TEMPERATURE
Teplofizika Vysokikh Temperatur
Vol. 22, 1984 (6 issues) $520

HYDROTECHNICAL CONSTRUCTION
Gidrotekhnicheskoe Stroitel'stvo
Vol. 18, 1984 (12 issues) $385

INDUSTRIAL LABORATORY
Zavodskaya Laboratoriya
Vol. 50, 1984 (12 issues) $520

INSTRUMENTS AND EXPERIMENTAL TECHNIQUES
Pribory i Tekhnika Eksperimenta
Vol. 27, 1984 (12 issues) $590

JOURNAL OF APPLIED MECHANICS AND TECHNICAL PHYSICS
Zhurnal Prikladnoi Mekhaniki i Tekhnicheskoi Fiziki
Vol. 25, 1984 (6 issues) $540

JOURNAL OF APPLIED SPECTROSCOPY
Zhurnal Prikladnoi Spektroskopii
Vols. 40-41, 1984 (12 issues) $540

JOURNAL OF ENGINEERING PHYSICS
Inzhenerno-fizicheskii Zhurnal
Vols. 46-47, 1984 (12 issues) $540

JOURNAL OF SOVIET LASER RESEARCH
A translation of articles based on the best Soviet research in the field of lasers
Vol. 5, 1984 (6 issues) $180

JOURNAL OF SOVIET MATHEMATICS
A translation of Itogi Nauki i Tekhniki and *Zapiski Nauchnykh Seminarov Leningradskogo Otdeleniya Matematicheskogo Instituta im. V. A. Steklova AN SSSR*
Vols. 24-27, 1984 (24 issues) $1035

LITHOLOGY AND MINERAL RESOURCES
Litologiya i Poleznye Iskopaemye
Vol. 19, 1984 (6 issues) $540

LITHUANIAN MATHEMATICAL JOURNAL
Litovskii Matematicheskii Sbornik
Vol. 24, 1984 (4 issues) $255

MAGNETOHYDRODYNAMICS
Magnitnaya Gidrodinamika
Vol. 20, 1984 (4 issues) $415

MATHEMATICAL NOTES
Matematicheskie Zametki
Vols. 35-36, 1984 (12 issues) $520

continued on inside back cover

Declassified and Approved For Release 2013/03/11 : CIA-RDP10-02196R000300060001-5